Structures and fragmentations of the deep-hole states in ^{11}B and ^{15}N

A dissertation
by

YOSOI, Masaru

Department of Physics
Faculty of Science
Kyoto University

January, 2003

Abstract

Decay particles from the s-hole states in ^{11}B and ^{15}N have been measured in coincidence with the quasifree ^{12}C$(p, 2p)$ and ^{16}O$(p, 2p)$ reactions at E_p=392 MeV. Triton-decay was found to be dominant for the ^{11}B(s-hole) state and also found to be larger than α-decay for the ^{15}N(s-hole) state despite its smaller Q-value compared to α-decay. Measured decay branching ratios are discussed in comparison with the results of statistical-model, microscopic cluster-model, and shell-model calculations. The energy spectra around the s-hole states in both ^{11}B and ^{15}N exhibit some bump-like sub-structures, which can be qualitatively explained by recent shell-model calculations for both nuclei.

The decay pattern of the s-hole state in ^{11}B can not be explained by the statistical-decay model. Microscopic cluster-model calculations with SU(3)$(\lambda\mu)$ wave functions explain the experimental decay character of the ^{11}B(s-hole) state qualitatively. For the s-hole state in ^{11}B, a quantitative comparison between the experimental results and theoretical calculations is, however, not sufficient to determine the ratio of the direct decay from the doorway s-hole state to the statistical decay.

In the fragmentation of the s-hole state in ^{15}N, the suppression of α-decay is clearly recognized, which supports the selection rule predicted by the microscopic SU(3)-cluster model. The shell-model calculations explain the measured relative branching ratios of decay particles fairly well in the 2-body decay region for the ^{15}N(s-hole) state. The ratio of the escape width $\Gamma^{\uparrow}$ to the spreading width $\Gamma^{\downarrow}$ for the s-hole state in ^{15}N is reasonably deduced from a comparison between the experimental results and both the statistical-model and shell-model calculations.

The present data for decay properties of the s-hole states produced from the targets of ^{12}C and ^{16}O will provide useful information on the studies of the hypernuclear productions and on the search of proton decay with water Čerenkov detectors.

Contents

Chapter 1

Introduction

1.1 Quasifree scattering and nuclear hole states

Quasifree scattering is one of the most direct ways of investigating both the single-particle properties in a nucleus and the nature of the strong interaction in the nuclear medium. The first kind of quasifree scattering reaction to be studied extensively was of the form ${}^{A}Z(p,2p)^{A-1}(Z\text{–}1)$, which is then interpreted as a direct knockout of a proton bound in the ${}^{A}Z$ nucleus by a fast incident proton and the ${}^{A-1}(Z\text{–}1)$ remains in a one-hole state. Chamberlain and Segrè [1] and Cladis, Hess and Moyer [2] first performed the $(p,2p)$ experiments at the Berkeley synchrocyclotron and demonstrated that this interpretation of the reaction mechanism is realistic and later this was verified by Wilcox and Moyer [3]. After the early $(p,2p)$ works [4, 5, 6], quasifree proton knockout reactions were systematically measured using proton beams at medium energies (150–1000 MeV) [7, 8, 9, 10] and, then, separation energies and widths of proton-hole states have been deduced for the wide mass-number range of nuclei, which directly revealed the existence of not only surface but also inner orbital shells in nuclei. These orbital shell structures were the basic character of the nuclear shell model. Thus, Bethe [11] emphasized that “the most striking feature of finite nuclei is the validity of the shell model. Nuclei can be very well described by assigning quantum numbers to individual nucleons, just as is done for the electrons in atoms”. The famous figure compiled by Jacob and Maris [10] is shown in Fig. 1.1.

From Fig. 1.1, the energy eigenvalues of the more strongly bound shells ($1s$, $1p$) were found to increase rapidly up to $A \approx 40$, and to saturate above. For the heavier nuclei, the experimental knowledge is rather poor since the distortion effects, *i.e.* the proton-target interactions both in the initial and final stages, reduce the intensity producing the hole states with large separation energies. The strong distortion is less severe in another quasifree process, namely, $(e,e'p)$ reaction, because the distortion of only one proton has to be taken into account. The $(e,e'p)$ reaction is, therefore,

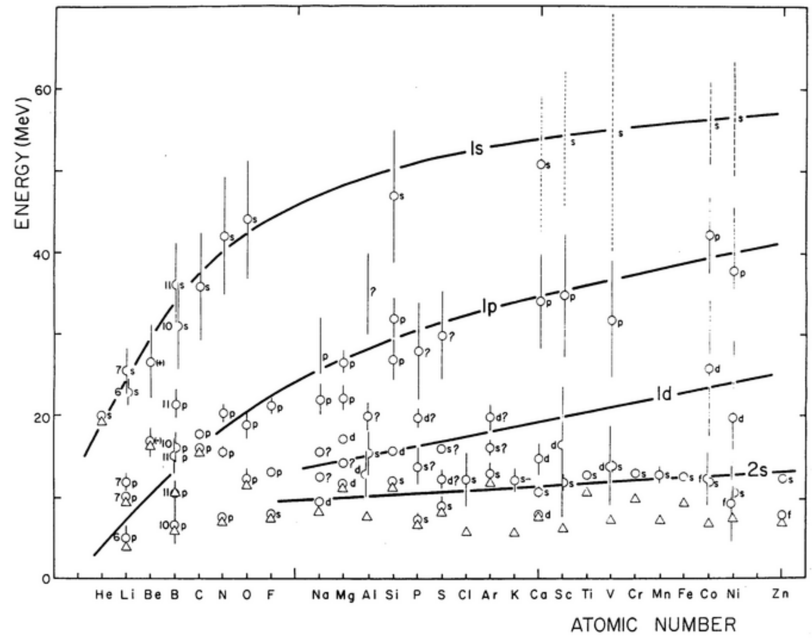

Figure 1.1: Separation energies, widths and angular momentum assignments of hole states obtained from quasifree scattering experiments, as functions of atomic number. The figure is taken from Ref. [10].

the cleanest tool known for the investigation of the more deeply bound nucleon state, although the cross section is much smaller than that of the $(p, 2p)$ reaction. After the first $(e, e'p)$ experiment at Frascati [12], plenty of quasifree $(e, e'p)$ investigations have been performed at all medium-energy electron accelerators. Fullani and Mougey [13] reviewed the $(e, e'p)$ works and presented the updated version of Fig. 1.1. However, information on the deep hole states in heavy nuclei has been still insufficient.

Since the distortion effects were expected to be relatively small at higher energies, quasifree knockout $(p, 2p)$ and (p, pn) reactions were measured at 1.0 GeV [14, 15], where the $1s$-hole states were clearly seen up to ^{40}Ca. Measurements of the $(p, 2p)$ reaction with polarized beams were also performed at several institutes [16, 17, 18, 19]. However, the reaction mechanism and medium effects on the nucleon-nucleon interaction rather than the single-hole structure were discussed in most cases. High resolution $(e, e'p)$ investigations during the last decade were mainly concentrated on the orbitals near the Fermi surface, for instance, $1p$-knockout for p-shell nuclei [20, 21], where the spectroscopic information on binding energies, occupation probabilities and momentum distributions was obtained. One of the major findings of these studies is a large reduction of the spectroscopic strength compared to the prediction of the independent-particle shell model and the theory has been further developed in respect to the ground state correlations [22, 23, 24]

In spite of a lot of experimental efforts via quasifree nucleon knockout reactions as well as pick-up reactions, only the macroscopic structures like separation energies (E_{sep}) and total widths ($\varGamma$) are obtained for deep-hole states. Detailed structures and fragmentation mechanisms of deep-hole states has been little known even for light nuclei until now, while interests in decay characters of s-hole states in light nuclei have been newly aroused through the study of the production of hypernuclei and the relation to the nucleon decay search, as mentioned below.

1.2 Fragmentations of deep-hole states

The 1s-hole states are observed as broad bumps in the region of highly excited energies above the particle decay thresholds with large widths in the excitation spectra of quasifree nucleon knockout reactions. For example, the proton s-hole states for ^{11}B and ^{15}N, which are the typical deep-hole states in p-shell nuclei, appear at $E_x \simeq$ 20 MeV with $\varGamma \simeq$ 9–13 MeV and $E_x \simeq$ 28 MeV with $\varGamma \simeq$ 14 MeV [4, 7, 10], respectively, where E_x is the excitation energy from its ground state and given with the Q-value of the knockout reaction as $E_x = E_{sep} + Q$. The energy and width give important information on the wave function of a deep-hole state. In addition, the partial fragmentation widths which relate to how a deep-hole state is fragmented should provide extremely interesting information on the fragmentation mechanism.

The wave function of a nuclear s-hole state ($\Psi_{s\text{-hole}}$) is given generally as $\Psi_{s\text{-hole}} = \Psi_{\text{doorway}} + \Psi_{\text{compound}}$, where the doorway s-hole state (Ψ_{doorway}) is orthogonal to the compound state (Ψ_{compound}). In medium-heavy and heavy nuclei, the doorway s-hole produced by a quasifree knockout reaction is propagating in a nuclear medium and spread out in the nucleus. Then, a compound nucleus with many particle-hole states is produced by strong coupling with higher configuration states, because the deep-hole state appears in a highly excited energy region in which the level density is very high. Thus, the deep-hole state has been believed to be fragmented statistically.

This scenario, however, may not be always realized in the case of deep-hole states in light nuclei. The ratio of the nuclear radius to the mean free path of a 1s-hole presents a good index of how much the doorway s-hole state survives without exciting many particle-hole states when the s-hole propagates in the nuclear medium. This can be simply estimated according to Ref. [33]. The mean free path (L) is calculated as [25]

$$L = \frac{\hbar^2 k}{2m_k W} \qquad k^2 = \frac{2m(E - V_R)}{\hbar^2},$$

where k is the wave number of the 1s-hole, V_R and W are the real and imaginary

Table 1.1: Ratios of nuclear radius (R) to mean free path (L) of 1s-hole. k and Γ denote the wave number and width of the s-hole state [27]. Experimental widths (Γ_{exp}) are also shown for light nuclei [4, 7, 10].

	^{7}Li	^{12}C	^{16}O	^{27}Al	^{40}Ca	^{208}Pb
k (fm^{-1})	0.89	0.81	0.77	0.71	0.67	0.47
Γ (MeV)	6.5	11.5	14	20	22	30
Γ_{exp} (MeV)	∼6	9–13	∼14	∼20		
L (fm)	9.4	4.8	3.8	2.4	2.1	1.1
R (fm)	2.40	2.52	2.77	3.30	3.76	6.52
R/L	0.26	0.53	0.73	1.4	1.8	5.9

parts of the hole-nucleus optical potential, and m is the nucleon mass. m_k is the so-called effective k-mass and the value of $\frac{m_k}{m} = (1 + \frac{m}{\hbar^2 k}\frac{\partial V_R}{\partial k})^{-1} \simeq 0.6$ is taken from the result of mean field calculations [26]. W is given by the s-hole width Γ as $W= \Gamma/2$. Since there are no experimental s-hole widths in the case of medium-heavy and heavy nuclei, the theoretical values estimated by Köhler [27] are employed, in which the experimental values of the s-hole widths in light nuclei are well reproduced. If the simple formula for the averaged kinetic energy (T) of an s-hole, $T= <E-V_R>= \frac{3}{4}\hbar\omega$ with $\hbar\omega = 41/A^{1/3}$ MeV is used [28], k of a 1s-hole is given by $k^2 \approx 1.5/A^{1/3}$ fm^{-2}. For the medium-heavy and heavy nuclei, the harmonic oscillator wave functions are supposedly less good, the kinetic energy T of a self-consistent field calculations [27] are used. For the nuclear radius (R), a root mean square (rms) radius [29] is used for ^{7}Li and $R= 1.1\ A^{1/3}$ is employed for other nuclei.

The calculated values of R/L for various nuclei are shown in Table 1.1. (It should be noted that, in Ref. [33], nucleon mass (m) was used for the calculation of L and rms values were taken for R. Then, the R/L values in Table 1.1 are different from their results.) R/L is less than 1 in p-shell nuclei, and larger than 1 in medium-heavy and heavy nuclei. These results indicate that the s-hole states in light nuclei may have large escape widths ($\Gamma^{\uparrow}$) ($\|\Psi_{\rm doorway}\|^2 \geq \|\Psi_{\rm compound}\|^2$) and that the spreading widths ($\Gamma^{\downarrow}$) are dominant ($\|\Psi_{\rm compound}\|^2 \gg \|\Psi_{\rm doorway}\|^2$) in heavy nuclei. It is expected that the character of the fragmentation of deep-hole states in light nuclei is considerably different from that in heavy nuclei, since the nuclear saturation property of the ground states largely deviates in light nuclei.

Theoretical studies of the structures and fragmentations of deep-hole states, especially for the partial fragmentation widths, were very scarce. The continuum shell model [30] was applied to describe the experimental excitation spectra for quasifree $(p, 2p)$ knockout. The Green function method [31] was developed and the hole-strength functions were calculated [32] in the framework of Brueckner's theory, which showed fair agreement with the spectra measured from $(e, e'p)$ knockout process. However, only the nucleon fragmentation of the final deep-hole state was taken into account in these calculations.

Yamada et al. recently calculated spectroscopic factors and partial decay widths for 2-body cluster decay processes from the doorway s-hole states of ^{11}B and ^{15}N in the framework of the microscopic cluster model with SU(3)$[f](\lambda\mu)$ wave functions [33]. The description of the s-hole state is based on the fact that the doorway s-hole state produced by the quasifree knockout reactions should have the same spatial symmetry as the ground state of the target nucleus, whose wave function is well described by the SU(3)-cluster model in light nuclei. The authors showed that a selection rule owing to the spatial symmetry is valid for fragmentations of s-hole states in light nuclei: n-, p-, d-, t- and ^{3}He-fragments are allowed, while the fragments such as the α-particle and the heavier particles are forbidden.

An intuitive understanding of the reason why α-cluster fragmentation is forbidden in the ^{11}B(s-hole) doorway state, is shown in Fig. 1.2. According to the simple shell model, the ^{11}B(s-hole) state is given as the $(s)^3(p)^8$ configuration [Fig.1.2(b)]. In the case of the ^{8}Be + t channel, the eight nucleon in the p-shell are correlated to form the ^{8}Be cluster [Fig.1.2(c)] and has a large spectroscopic factor. On the other hand, in the case of the ^{7}Li + α channel, the four nucleons in the p-shell are correlated to form the α cluster and then the remainder nucleus, ^{7}Li, corresponds to the unbound s-hole state [Fig.1.2(d)], which is orthogonal to the ^{7}Li ground-band states [Fig.1.2(e)]. Therefore, 2-body α-cluster fragmentation is forbidden. This is strictly supported by the SU(3) algebra if the ^{11}B(s-hole) state has the same SU3$(\lambda\mu)$=(04) as the ^{12}C ground state [Fig.1.2(a)], because $(\lambda\mu)$=(04) representation can be given from $(00)\otimes(40)\otimes(40)_r$ but can not be constructed from $(00)\otimes(30)\otimes(50)_r$, where the $(\lambda, \mu)_r$=$(40)_r$ and $(50)_r$ describe the relative wave functions between ^{8}Be and t and between ^{7}Li and α, respectively.

Since the Q-values for α-fragments in most light nuclei are larger than those for other cluster decay channels, α-decay is favored in the statistical decay process. Thus, the experimental study of the α-decay partial widths (Γ_α) is especially important to investigate if deep-hole states are statistically fragmented.

Various thresholds for fragmentation channels of ^{11}B and ^{15}N are shown in Fig. 1.3 and Fig. 1.4, respectively. In the case of the ^{15}N(s-hole) state, the threshold energy of the 3-body decay is higher than 2-body decay thresholds of n+^{14}N, p+^{14}C, d+^{13}C, t+^{12}C and α+^{11}B channels, while the 3-body decay channel of 2α+t has a very low threshold energy and may compete against the 2-body decay processes of n+^{10}B, p+^{10}Be, d+^{9}Be, t+^{8}Be and α+^{7}Li for the ^{11}B(s-hole) state. In general, theoreti-

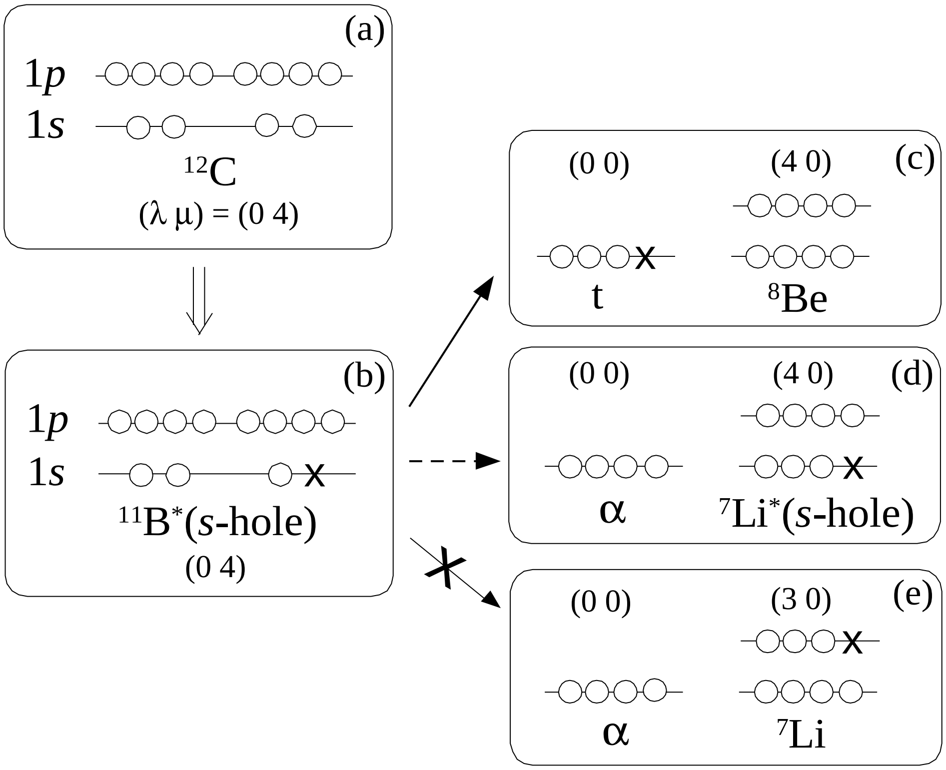

Figure 1.2: Intuitive explanation for the suppression of the α-cluster fragmentation in the ^{11}B(s-hole) doorway state. (a) The $(s)^4(p)^8$ shell model configuration for the ^{12}C ground state (g.s.). (b) The $(s)^3(p)^8$ shell model configuration for the ^{11}B(s-hole) doorway state, which has the same SU3($\lambda\mu$)=(04) configuration as (a). (c) In the ^{8}Be+t fragmentation channel, the eight nucleons in the p-shell of the ^{11}B(s-hole) are correlated to form a ^{8}Be cluster. (d) In the ^{7}Li*+α fragmentation channel, the four nucleons in the p-shell of the ^{11}B(s-hole) are correlated to form an α-cluster, where the residual nucleus ^{7}Li remains in the s-hole state. (e) The ^{7}Li(g.s.)+α fragmentation channel, which is orthogonal to (d). Therefore this channel is forbidden. The value of SU(3)($\lambda\mu$) of each cluster is indicated in all panels.

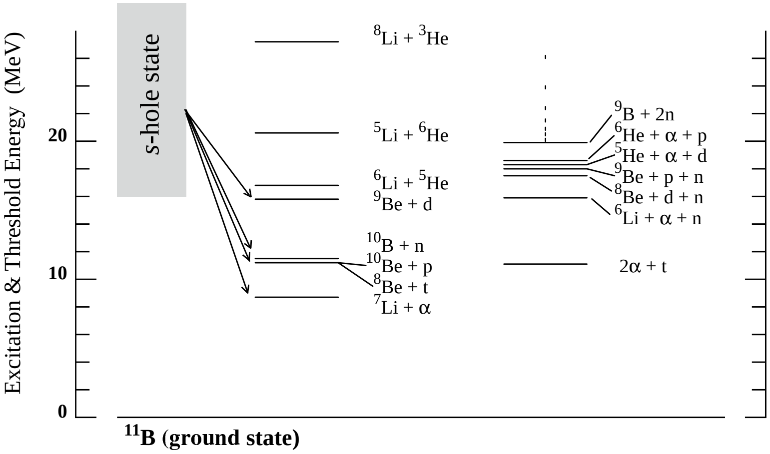

Figure 1.3: Threshold energies for various fragmentation channels of the s-hole state in ^{11}B. The energy region of the ^{11}B(s-hole) state is shown at the left side.

cal calculations including 3-body decay are practically difficult and might be more complicated than 2-body decay. Then, the ^{15}N is more suitable to understand the microscopic structure of the deep hole state and its fragmentation mechanism. It is also interesting to study the effect of 3-body decay in the fragmentation process by comparing the decay patterns of the ^{11}B(s-hole) and ^{15}N(s-hole) states.

1.3 Related topics

Nuclear deep-hole states are closely related to hypernuclear physics [34, 35]. In the (K^-,π^-) strangeness-exchange reaction, the substitutional states with a neutron s-hole Λ-particle configuration $[s_N^{-1}s_\Lambda(\text{or } p_\Lambda)]$ are strongly populated [36] since the momentum transfer of the reaction is very small ($q \simeq 50$ MeV/c). If the selection rule from the SU(3) spatial symmetry as mentioned above is applied, ^{11}C(s-hole), which is the nuclear-core s-hole state of ${}^{12}_{\Lambda}$C(s_N^{-1},s_Λ), can decay to the ^{8}Be + ^{3}He channel but the decay to the ^{7}Be + α channel is suppressed. Thus, the ${}^{12}_{\Lambda}$C(s_N^{-1},s_Λ) state with the [^{11}C(s-hole)$\otimes s_\Lambda$] configuration can decay to the ${}^{9}_{\Lambda}$Be + ^{3}He channel, while the decay to the ${}^{8}_{\Lambda}$Be + α channel is largely hindered.

The production of hypernuclei with strangeness $S{=}{-}2$ via the Ξ^- atomic capture reaction at rest is of particular interest because the Q-value of the elementary process ($\Xi^- p \rightarrow \Lambda\Lambda + 28$ MeV) is almost the same as the separation energy of an s-state proton in light nuclei. According to recent hybrid emulsion-counter experiments with the (K^-,K^+) reaction [37, 38, 39, 40, 41], several double-Λ and twin-Λ hypernuclear production events were identified. Five events including an event with two interpretations were produced by Ξ^- atomic captures into ^{12}C. Only the following three

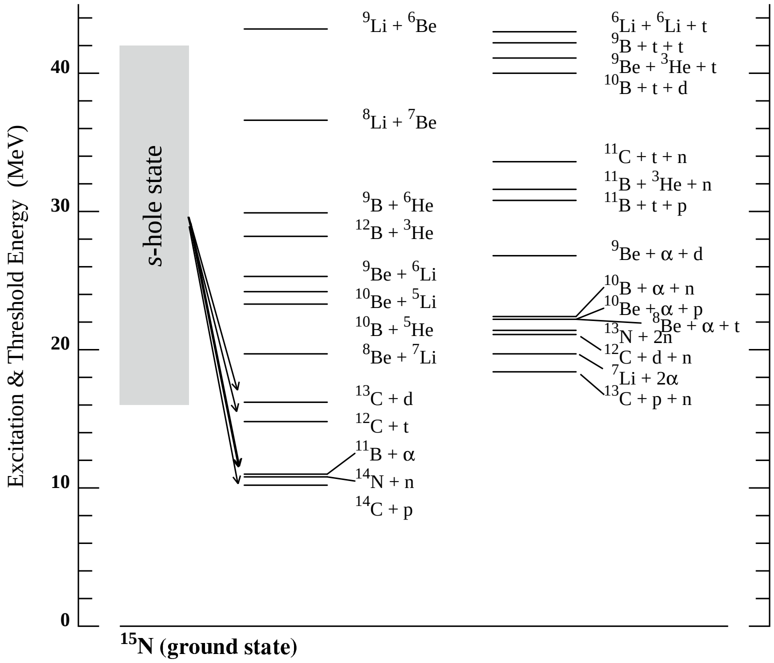

Figure 1.4: Threshold energies for various fragmentation channels of the s-hole state in ^{15}N. The energy region of the ^{15}N(s-hole) state is shown at the left side.

processes were observed:

$$\Xi^- +^{12}\mathrm{C} \longrightarrow \ {}^{10}_{\Lambda\Lambda}\mathrm{Be} + t,\ {}^{6}_{\Lambda\Lambda}\mathrm{He} + \alpha + t, \quad \text{and} \ \ {}^{9}_{\Lambda}\mathrm{Be} + {}^{4}_{\Lambda}\mathrm{H},$$

where a triton or a ${}^{4}_{\Lambda}\mathrm{H}(=t \otimes \Lambda)$ was emitted in all cases. This high probability of the $S{=}-2$ formation with a triton-based fragment is hardly understood on the basis of the statistical decay model [43] and the microscopic transport model [44]. The $S{=}-2$ hypernuclear production rates were also explored by Yamada *et al.* using a direct reaction model [45]. Their calculation, however, does not explain the enhancement of t-based fragments if the Ξ^- particle interacts mainly with a p-state proton in ^{12}C. It is therefore important to better understand the fragmentation of the s-hole state in ^{11}B.

Decay properties of the s-hole states produced from the targets such as ^{12}C and ^{16}O are also interesting from a particle physics point of view. In fact, C and O are typical nuclei used as detectors for studies of proton decay and neutrinos. Both the decay of an s-proton and the neutrino knockout of an s-proton leaves an s-hole. Thus, proton decay and neutrino interactions can be studied by observing the decay from the s-hole states as well.

Deexcitation γ-rays from the hole states of ^{15}N and ^{15}O have been used in the nucleon-decay search by means of the Kamiokande and Super-Kamiokande water

Čerenkov detectors [46, 47, 48], which is one of the most efficient methods to find nucleon decays. Ejiri discussed deexcitations of proton hole states in ^{15}N produced by proton decay in ^{16}O [49]. If a proton in ^{16}O decays, the remaining ^{15}N nucleus is left in the ground state or excited states and the latter can emit prompt γ-rays. The γ-decay rates are 100 % for the low excited p-hole states. If the excited state is the s-hole state, many particle decay channels are open. It decays by emitting n, p, d, t, α, and other clusters. Here, various residual nuclei such as ^{14}C, ^{14}N, ^{13}C, ^{13}N, ^{13}B, ^{12}N, ^{12}C, ^{12}B, ^{11}Be, etc., are left in their ground or excited states, the latter of which also deexcite by emitting γ rays. The level and deexcitation schemes relevant to the proton hole in ^{15}N is shown in Fig. 1.5.

By using these prompt γ-rays as a tag, the background contamination can be strongly reduced in the $p \rightarrow \overline{\nu} + K^+$ mode [47, 48], which is favored by most supersymmetric Grand Unified Theories (SUSY GUT) [50]. Moreover, if the branching ratio of a characteristic γ-ray such as the 15.1 MeV γ from the ^{12}C, ^{13}N, and ^{13}C, it may provide a new method to determine a mode-independent nucleon-decay rate like $n \rightarrow \nu\nu\bar{\nu}$ [46]. The 15.1 MeV γ-ray is also one of the most astrophysically significant γ-rays [51]. For example, the ratio of the flux of 15.1 MeV γ-rays to the flux of 4.44 MeV γ-rays resulting from excitation of ^{12}C and spallation of ^{16}O is a sensitive measure of the spectrum of the exciting particles produced in solar flares and other cosmic sources.

Information on the deexcitation γ-rays from the s-hole state can be obtained not only from the direct measurements of γ-rays, but also, in principle, from the particle decay measurements, because the production rate of decay to discrete excited states in residual daughter nuclei are obtained and γ-decay probabilities from these discrete states are well known.

In the present work, charged particle and neutron decays from the quasifree proton-knockout reactions on ^{12}C and ^{16}O are studied to understand the structures and fragmentation mechanisms of the s-hole states in ^{11}B and ^{15}N. (The measurements of neutron decay were only performed for the ^{16}O target.) The results of the early test experiment for ^{11}B [52] and the preliminary analysis of the charged-particle decay measurements [53] were already reported. The experimental setup and procedures are explained in Chap. 2. The data analysis and results are presented in Chap. 3. The structures and fragmentation characters of s-hole states in both ^{11}B and ^{15}N are discussed in Chap. 4, in comparison with the theoretical calculations of a statistical model, an SU(3)(λ, μ) microscopic cluster model, and a shell model. Conclusions are presented in Chap. 5. The efficiency calibration of the neutron detector is described in Appendix A. The statistical-model calculations and the microscopic cluster-model calculations are briefly described in Appendix B and C, respectively.

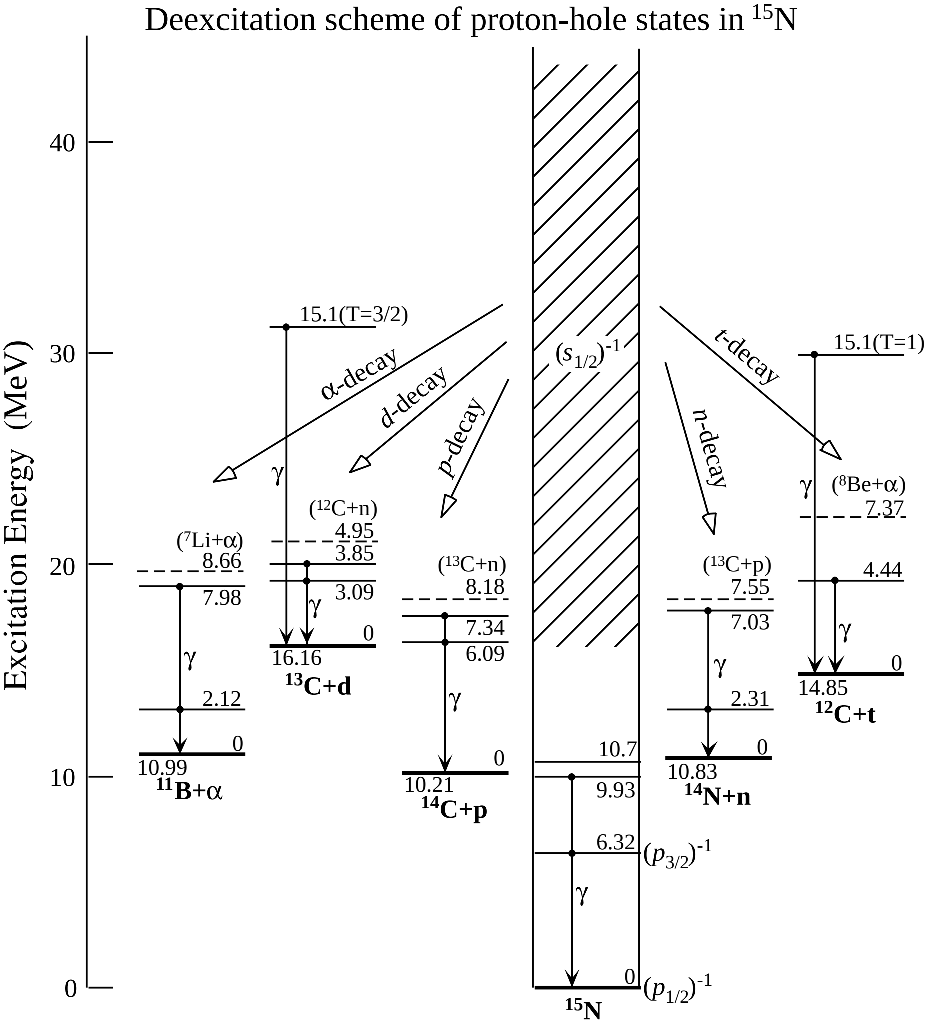

Figure 1.5: Level scheme of proton-hole states in ^{15}N and their deexcitation modes. Particle-decay threshold energies of residual nuclei after emitting neutrons, protons, deuterons, tritons and α-particles from the ^{15}N(s-hole) state are indicated by dashed lines, respectively. Only the first and the highest excited states below the particle-decay threshold are displayed for each residual nucleus, except for the 15.1 MeV states in ^{12}C and ^{13}C.

Chapter 2

Experiment

2.1 Overview and beam transportation

The experiment was carried out at the Research Center for Nuclear Physics (RCNP), Osaka University, by using a 392 MeV proton beam. We separated the experiment into two parts. In the first beam time, charged particle decay of the *s*-hole states in both ^{11}B and ^{15}N was measured in coincidence with the quasifree ^{12}C$(p, 2p)$ and ^{16}O$(p, 2p)$ reactions, and neutron decay of the *s*-hole state in ^{15}N was studied in the second beam time. The quasifree $(p, 2p)$ reaction was measured with the dual spectrometer system consisting of the high resolution spectrometer Grand Raiden (GR) [54] and the large acceptance spectrometer (LAS) [55]. Sixteen telescopes of ΔE-E Si solid-state detectors (SSD) were used for the measurements of p-, d-, t-, and α-decays, and thirty liquid scintillation counters were employed to detect decay neutrons.

A proton beam extracted from a high intensity ion source [56] was accelerated up to 64.2 MeV by the K=120 MeV AVF cyclotron and its energy was boosted to 392 MeV by the K= 400 MeV ring cyclotron [57]. The beam was transported achromatically from the ring cyclotron to the target in the scattering chamber and further lead to a Faraday cup in a well shielded beam dump about 25 m downstream of the target. The beam spot size at the target point was typically 1 mmϕ. Since the beam line was reconstructed between two beam times, the first experiment of the charged particle decay was performed with the old WN beam line and the next neutron decay experiment was carried out with the new WS beam line. (Although the new WS beam line can be applied for a high resolution measurement with a dispersion matching mode [58], an achromatic transport was still used in the present experiment.) The very stable and clean (halo-free) beam was provided through the experiment. A schematic layout of the RCNP cyclotron facility with both new and old beam lines is shown in Fig. 2.1.

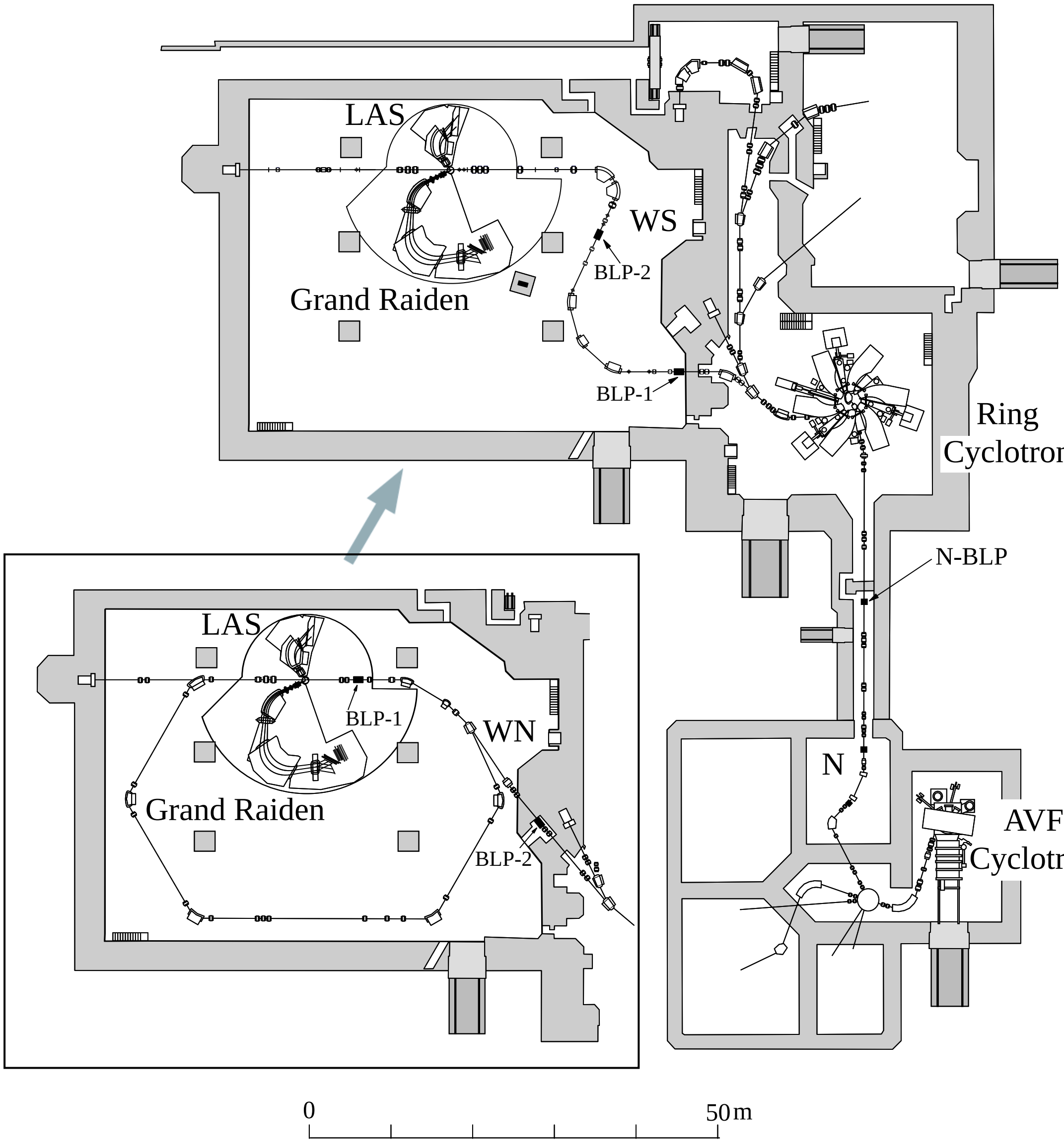

Figure 2.1: Layout of the RCNP cyclotron facility. Both the old WN and new WS beam lines are shown.

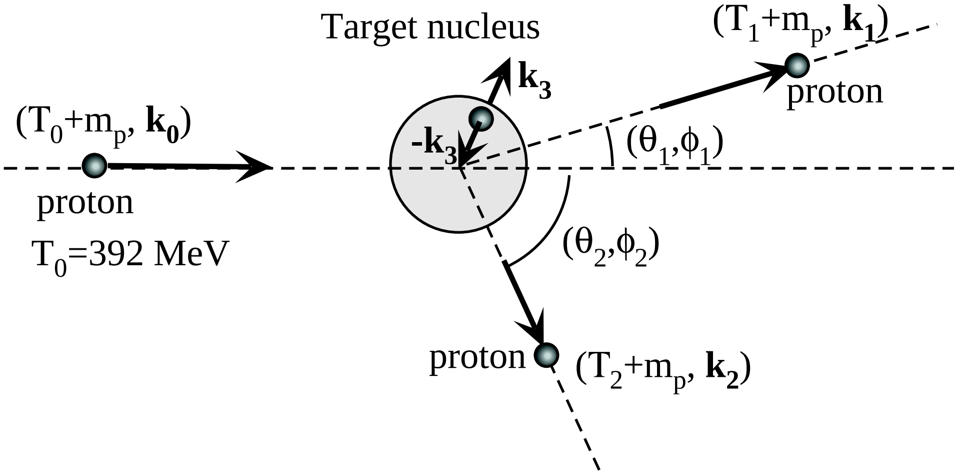

Figure 2.2: $(p, 2p)$ reaction in the laboratory coordinate system. Four-momenta are indicated as $(T_i{+}m_p\ ,\ \boldsymbol{k}_i)$ for incident (i=0) and two emerging (i=1,2) protons, respectively. $\boldsymbol{k}_3$ denotes the recoil momentum.

2.2 Quasifree $(p, 2p)$ reactions

2.2.1 Kinematics

The $(p, 2p)$ reaction at an intermediate energy such as 392 MeV is well described by the direct reaction picture and is flexible enough to choose the proper kinematics to enhance the s-hole state [59].

Fig. 2.2 illustrates the $(p, 2p)$ reaction in the laboratory coordinate system. For the reaction $A(p, 2p)B^*$, one measures the differential cross section as a function of the momenta $\boldsymbol{k}_1$ and $\boldsymbol{k}_2$ of two emerging protons. From the energy and momentum conservation, the state of the final nucleus B^* is specified by two quantities [60]:

$$\boldsymbol{k}_3 = \boldsymbol{k}_0 - \boldsymbol{k}_1 - \boldsymbol{k}_2, \tag{2.1}$$

$$E_{sep} = T_0 - (T_1 + T_2 + T_3) = E_x - Q, \tag{2.2}$$

where $\boldsymbol{k}_0$ and T_0 are the momentum and energy of the incident proton, and T_1, T_2, and T_3 are the kinetic energies of two emerging protons, and of the recoiling nucleus B^*, respectively. $\boldsymbol{k}_3$ is the recoil momentum of B^*. If one neglects the distortion effect, the initial momentum of a proton removed from the target A is equal to $-\boldsymbol{k}_3$, since the momentum of the target A is zero. E_{sep} is the separation energy and E_x is the excitation energy of B^* from its ground state. The reaction Q-value is given by $Q{=}M_A{-}(m_p{+}M_B)$, where m_p, M_A, and M_B are the masses of proton, target A, and residual nucleus B, respectively.

Table 2.1: Setting parameters of spectrometers in the coincidence measurements with decay particles. The suffix 1 and 2 correspond to GR and LAS, respectively. The values of the central orbits are denoted for angles (θ) and kinetic energies (T).

	Q-value (MeV)	E_{sep} (s-hole) (MeV)	θ_1 (deg)	T_1 (MeV)	θ_2 (deg)	T_2 (MeV)
^{12}C(p,2p)^{11}B	-15.96	36	25.5	268	51.6	88
^{16}O(p,2p)^{15}N	-12.13	39	25.5	265	51.0	88

In the coincidence measurements with decay particles, GR was set at 25.5° and detected a fast proton of the $(p, 2p)$ reaction and another proton was detected by LAS, taking into account the difference of the momentum acceptance of GR (5 %) and LAS (30 %). The laboratory angle of LAS and the magnetic fields of the spectrometers were determined to satisfy the zero-recoil momentum condition ($k_3 = 0$) at the central energy of the $1s_{1/2}$-knockout bump, where the cross section leading to the s-hole state is maximum. The kinematical parameters used in the experiment are shown in Table 2.1. Although the recoil momentum k_3 is distributed around zero due to the finite solid angles and momentum acceptances, the width of the distribution of k_3 is only about 60 MeV/c (FWHM) for the s-hole states.

In the second beam time, the angular correlations of the ^{16}O$(p, 2p)^{15}$N reaction for $30^\circ \leq \theta_{\mathrm{LAS}} \leq 65^\circ$ were also measured to estimate the amount of non-quasifree components around the excitation energy of the s-hole state.

2.2.2 Dual spectrometer system

Emerging two protons from the quasifree $(p, 2p)$ reaction were measured with the dual magnetic spectrometer system, consisting of GR and LAS. A schematic view of the dual spectrometer system is shown in Fig. 2.3.

GR [54, 61] was designed and constructed for high resolution measurements, and also for detecting tritons with $E_t \leq 450$ MeV emerging from, for example, (^{3}He,t) reactions. GR consists of three dipole (D1, D2, and DSR) magnets, two quadrupole (Q1 and Q2) magnets, a sextupole (SX) magnet, and a multipole (MP) magnet as shown in Fig.2.3. In Table 2.2, the designed values of the specifications and ion-optical properties of GR are summarized. GR is mostly characterized by its high momentum resolution of $p/\Delta p$= 37,000 and the large magnetic rigidity of 5.4 T·m. The second-order ion-optical properties like the tilting angle of the focal plane are adjusted by the SX magnet, and higher-order aberrations are minimized by the MP magnet and the curvatures of the pole edges at the entrance and exit of dipole magnets. The

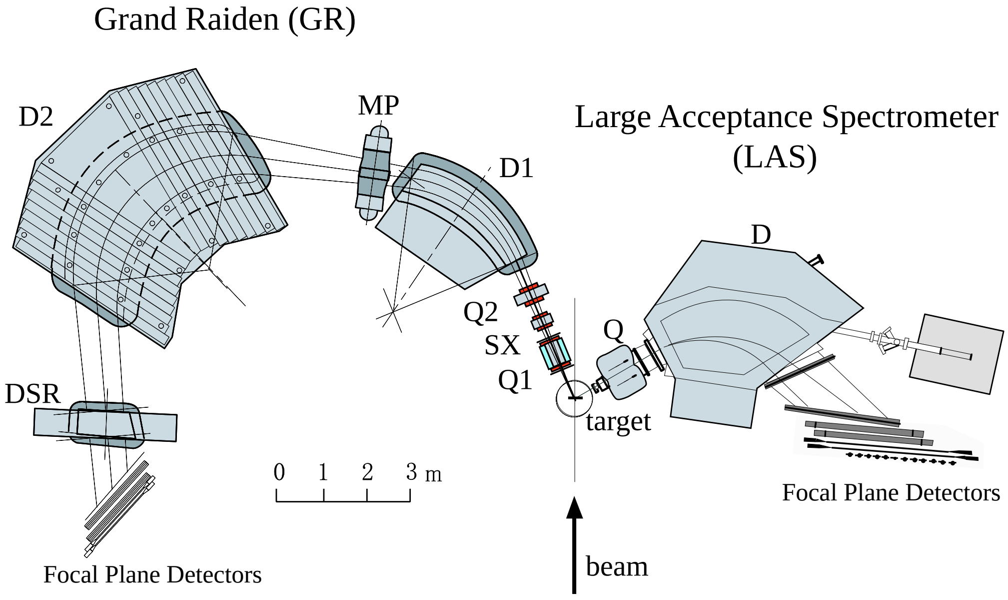

Figure 2.3: Schematic view of the dual spectrometer system at RCNP. The high resolution spectrometer Grand Raiden (GR) is placed on the left side of the beam line and the large acceptance spectrometer (LAS) is on the right side.

Table 2.2: Design specifications of the Grand Raiden spectrometer

Mean orbit radius	3 m
Total deflection angle	162°
Measurable angle	−4° to 90°
Momentum range	5 %
Momentum dispersion	15.45 m
Momentum resolution $(p/\Delta p)$	37000[a]
Tilting angle of focal line	45°
Focal plane length	120 cm
Maximum magnetic rigidity	5.4 T·m
Maximum field strength (D1, D2)	1.8 T
Maximum field gradient (Q1)	0.13 T/cm
Maximum field gradient (Q2)	0.033 T/cm
Horizontal magnification $(x\|x)$	−0.417
Vertical magnification $(y\|y)$	5.98
Horizontal acceptance angle	±20 mrad
Vertical acceptance angle	±70 mrad
Maximum solid angle	∼4.3 msr[b]
Flight path for the central ray	20 m

[a] The source width is assumed to be 1 mm.

[b] This is the actual value measured in the present experiment.

Table 2.3: Design specifications of the large acceptance spectrometer (LAS)

Mean orbit radius	1.75 m
Total deflection angle	70°
Measurable angle	0° to 130°
Momentum range	30 %
Momentum resolution ($p/\Delta p$)	5000
Tilting angle of focal line	~57°
Focal plane length	170 cm
Maximum magnetic rigidity	3.22 T·m[a]
Maximum field strength (D)	1.6 T
Maximum field strength (Q)	−74 mT/cm
(Sextupole component)	0.465 mT/cm^2
(Octupole component)	0.029 mT/cm^3
Horizontal magnification $(x\|x)$	−0.40
Vertical magnification $(y\|y)$	−7.3
Horizontal acceptance angle	±60 mrad
Vertical acceptance angle	±100 mrad
Maximum solid angle	~20 msr
Flight path for the central ray	6.2 m

[a] The value is given for the high momentum end ($\delta = +15$ %).

third dipole (DSR) magnet, which is added for the measurements of the in-plane polarization transfer, was not used in the present experiment.

LAS [55] was designed as the second arm spectrometer with medium energy resolution, complementary to GR. LAS is a QD type spectrometer with a large solid angle (~20 msr) and a wide momentum acceptance ($p_{max}/p_{min} \simeq 1.3$). The design specifications are listed in Table 2.3. Following the requirement from ion optical calculations, the quadrupole magnet includes sextupole and octupole components.

The entrance slits of both spectrometers were fully opened for maximum acceptance in the coincidence measurements with decay particles. Absolute values of cross sections were determined by normalizing results obtained in separate measurements with slits defining the solid angles of GR and LAS to 2.4 msr and 12.0 msr, respectively.

2.2.3 Focal-plane detectors of GR and LAS

Two multi-wire drift chambers (MWDC) in each focal plane of both spectrometers determined the positions and the incidence angles of particles. Particle identification was provided by the ΔE signals from plastic scintillation counters, that were also

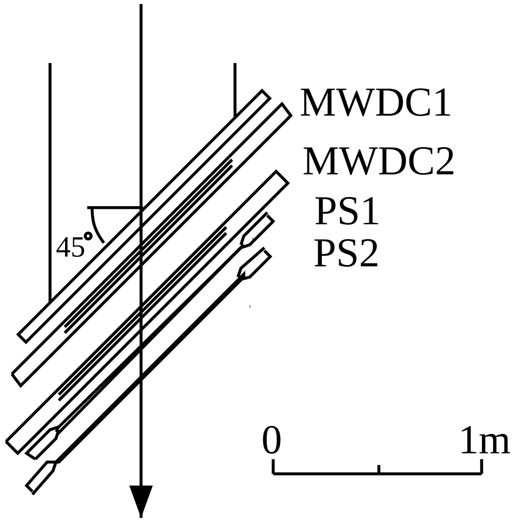

Figure 2.4: Focal plane detectors of Grand Raiden.

used for trigger signals. The layout of the focal-plane detector system of GR is shown in Fig. 2.4.

The type of any plane of the MWDC's is, so called, a vertical drift chamber (VDC), in which electrons ionized by a radiation drift perpendicularly to the anode plane [62]. Specifications of the GR-MWDC's are summarized in Table 2.4. Each MWDC consists of two sets of anode wire planes (X and U), sandwiched between three cathode planes. Anode planes include sense wires and potential wires. The structure of an X-wire plane is schematically illustrated in Fig. 2.5. It should be noted that the spacing of sense wires are different between X-planes (6 mm) and U-planes (4 mm) for the GR-MWDC's. The potential wires serve to make a uniform electric field between the cathode plane and the anode plane. Taking into account the difference of wire diameters between sense wires and potential wires, high voltages of -350 V and -500 V were supplied to the potential wires in the X- and U-plane, respectively, while the cathode voltage was -5.6 kV and the sense wires were grounded (0 V). The gas multiplications by avalanche processes are only occurred near the sense wires. In the case of Fig. 2.5, drift-time information from four wires are obtained and, thus, the particle trajectory can be determined with a good position resolution (typically 300 μm (FWHM)).

Mixture gas of argon (71.4 %), iso-butane (28.6 %), and iso-propyl-alcohol was used. The iso-propyl-alcohol was mixed in the argon gas with vapor pressure at 2° in order to reduce the deterioration due to the aging effect like the polymerizations of gas on the wire surface. Signals from the sense wires were pre-amplified and discriminated by LeCroy 2735DC cards, which were directly connected on the printed bases of the

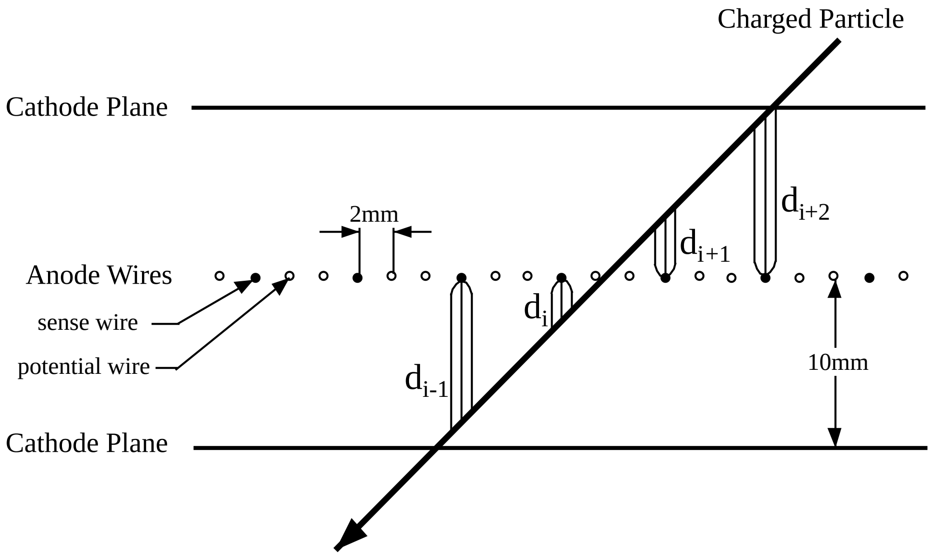

Figure 2.5: Structure of an X-plane of the MWDC's. Cathode planes and anode wires are illustrated with a typical charged particle track.

MWDC's without cables. Output ECL signals of 2735DC cards were transfered to LeCroy 3377 TDC's, in which information on the hit timing of each wire was digitized.

The GR drift chambers were backed by two plastic scintillation counters with a thickness of 3 mm (PS1) and 10 mm (PS2), whose area size was 1200^{W} mm × 120^{H} mm. The scintillation light was detected by photo-multiplier tubes (Hamamatsu H1161) on both sides of PS1 and PS2. Signals from these scintillators were used to generate a trigger signal of the GR event. An aluminum plate with a thickness of 5 mm was placed between PS1 and PS2 in order to avoid that the secondary electrons produced by one scintillator hit another scintillator.

The focal plane detector system of LAS consists of two MWDC's [55] and two planes of plastic trigger scintillators (PS1 and PS2). The detector layout is shown in Fig. 2.6. In order to cover the vertically broad focal plane of LAS, both PS1 and PS2 consist of three (up, middle, and down) scintillation counters. Each scintillator had the size of 2000^{W} mm × 150^{H} mm with a thickness of 6 mm. Fast photo-multiplier tubes (Hamamatsu H1949) were used on both sides of each scintillator. (A scintillator hodoscope drawn in the figure was not used in the present experiment.)

The LAS-MWDC's are similar to those for GR, except for the size and wire configuration. Although each MWDC consists of three anode planes (X, U, and V), the V plane has not been used due to the lack of the readout electronics. A high voltage of −5.4 kV was supplied to the cathode planes, and −300 V was to the potential wires. The specifications of the LAS-MWDC's are summarized in Table 2.5.

Table 2.4: Specifications of the MWDC's for Grand Raiden.

Wire configuration	X (0°=vertical), U (48.2°)
Active area	1150^{W} mm × 120^{H} mm
Number of sense wires	192 (X), 208 (U)
Cathode-anode gap	10 mm
Anode wire spacing	2 mm
Sense wire spacing	6 mm (X), 4 mm (U)
Sense wires	20 μmϕ gold-plated tungsten wire
Potential wires	50 μmϕ gold-plated beryllium-copper wire
Cathode	10 μm-thick carbon-aramid film
Cathode voltage	−5.6 kV
Potential-wire voltage	−350 V (X), −500 V (U)
Gas mixture	Argon + Iso-butane + Iso-propyl-alcohol (71.4 %) (28.6 %) (2° vapor pressure)
Entrance and exit window	12.5 μm aramid film
Distance between two MWDC's	250 mm
Pre-amplifier	LeCroy 2735DC

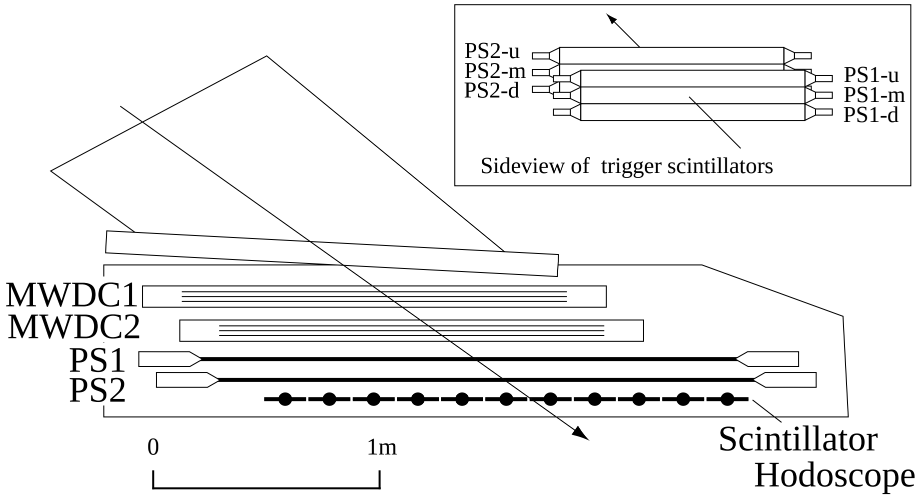

Figure 2.6: Focal plane detectors of LAS.

Table 2.5: Specifications of the MWDC's for LAS.

Wire configuration	X (0°=vertical), U (31°), V (−31°)
Active area	1700^{W} mm × 350^{H} mm
Number of sense wires	272 (X), 256 (U, V)
Cathode-anode gap	10 mm
Anode wire spacing	2 mm
Sense wire spacing	6 mm
Sense wires	20 μmϕ gold-plated tungsten wire
Potential wires	50 μmϕ gold-plated beryllium-copper wire
Cathode	10 μm-thick carbon-aramid film
Cathode voltage	−5.4 kV
Potential-wire voltage	−300 V
Gas mixture	Argon + Iso-butane + Iso-propyl-alcohol
	(71.4 %) (28.6 %) (2° vapor pressure)
Entrance and exit window	25 μm aramid film
Distance between two MWDC's	164 mm
Pre-amplifier	LeCroy 2735DC

2.2.4 Trigger and readout systems of focal plane scintillators

The readout electronics and trigger systems of the focal plane scintillators for GR and LAS, are shown in Figs. 2.7 and 2.8, which were all placed near the focal planes of GR and LAS, respectively. Any output of photomultiplier tube (PMT) was first divided into two signals and one was discriminated by a constant fraction discriminator (CFD) and another was sent to a FERA (Fast Encoding and Readout ADC (analog-to-digital converter)) module. One of the CFD outputs was transmitted to the TDC (time-to-digital converter) system consisting of TFC's (Time to FERA Converter) and FERA's. A coincidence signal of two PMT-outputs on both sides of the same scintillator was generated by a Mean-Timer circuit, in which the times of two signals were averaged. Thus, the position dependence of output timing caused by the difference of the propagation time in the long scintillator was minimized.

The trigger system was constructed with LeCroy 2366 universal logic modules (ULM) with field programmable gate-array (FPGA) chips [63]. As shown in Fig. 2.7 (Fig. 2.8), the trigger system received signals from the outputs of Mean Timers and generated the GR (LAS) trigger by the coincidence of PS1 and PS2, internally. (In the LAS case, PS1 (or PS2) was generated when there was at least one signal of three Mean Timer outputs corresponding to up, middle, and down scintillators.) The GR trigger gave the gate signals of ADC modules and start or stop signals of TDC modules for the GR focal plane detectors, while the LAS trigger was used as the ADC

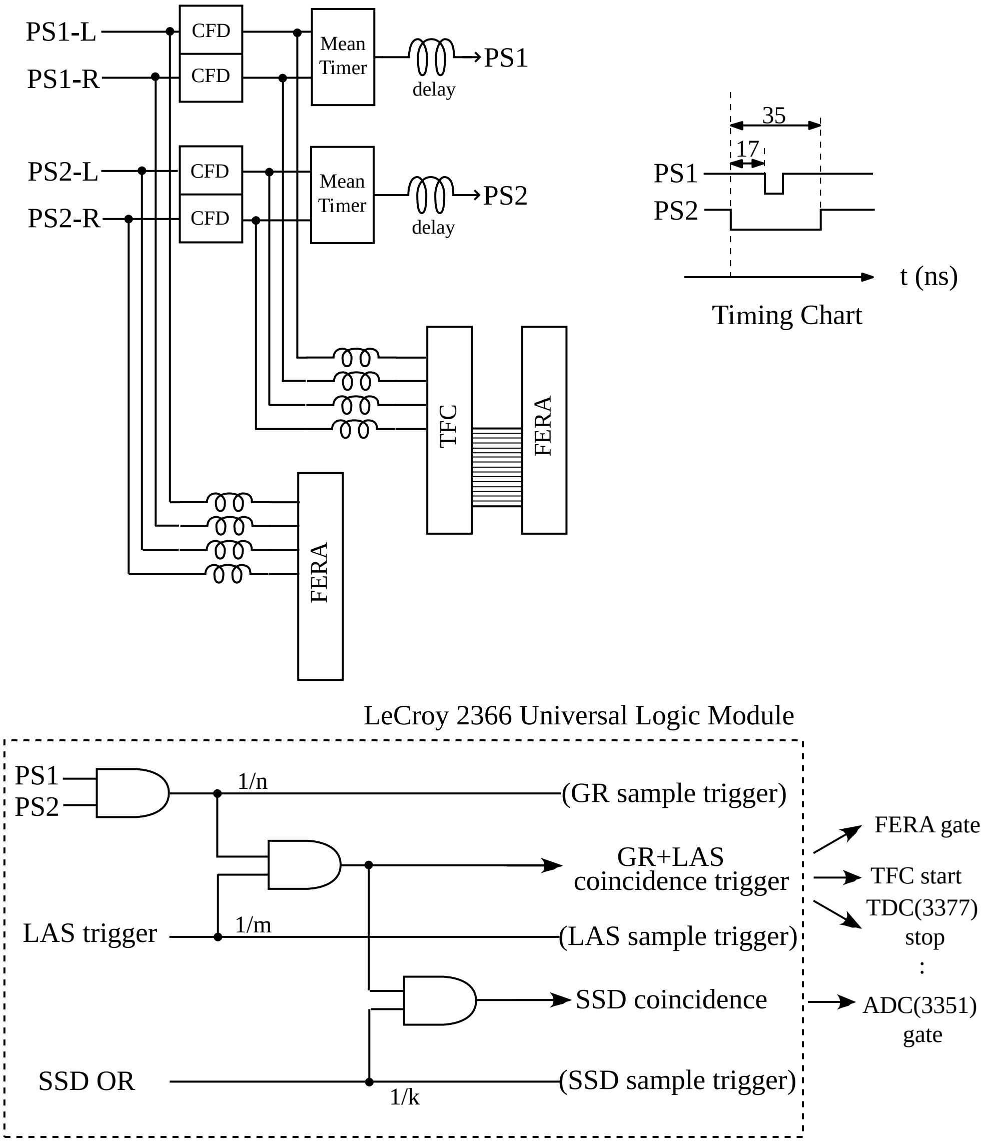

Figure 2.7: Circuit diagram for the GR focal plane detectors and the trigger logic for the coincidence measurements.

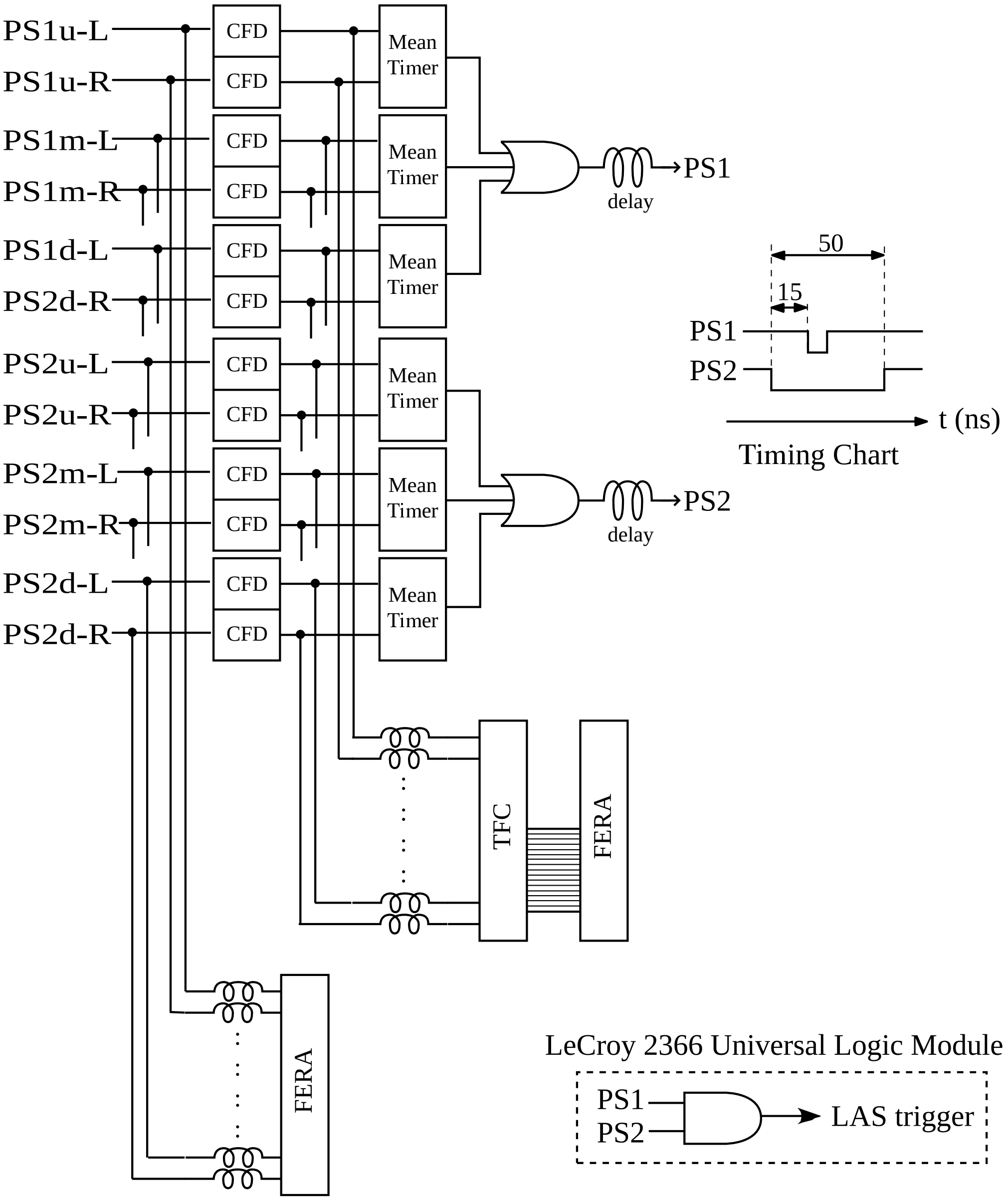

Figure 2.8: Circuit diagram for the LAS focal plane detectors.

gate signals and the TDC start or stop signals for the LAS focal plane detectors,

The coincidence trigger of GR and LAS was also generated in the 2366 module of the GR side, where the output timing was determined by the GR trigger. In order to select the main trigger mode, it was only needed to set the proper sampling conditions (n, m, and k in Fig. 2.7) via CAMAC functions. Thus, the system was very flexible to operate the trigger in several modes, for example, a GR+LAS coincidence mode (no sampling), a GR single mode (n=1), a LAS single mode (m=1), and an SSD test mode (k=1, described in § 2.3.3). During the present experiment, the GR+LAS coincidence mode was usually used, except for some measurements for the check of detectors such as SSD's. (In the first experiment, GR single triggers are mixed with a small sampling rate.) The main trigger output started the data acquisition system.

2.3 Measurements of charged particle decay

2.3.1 SSD-Ball

Charged particles decaying from the highly excited states in ^{11}B and ^{15}N were detected in sixteen telescopes of ΔE-E Si solid-state detectors (called SSD-Ball) in coincidence with two protons of the $(p, 2p)$ reaction. This SSD-Ball is an upgraded version of the previous SSD-Ball [64, 65] at RCNP. Each telescope consisted of a thin (20 μm, 50 μm or 100 μm) ΔE SSD (surface-barrier type) and a thick (5000 μm) E detector (lithium-drifted silicon (Si(Li)). The active area of a ΔE was 300 mm^2 or 450 mm^2 and that of an E is 450 mm^2. Eight 20 μm ΔE detectors were used for the identification of α-particles with $E_\alpha \geq 4.5$ MeV. The 50 μm and 100 μm ΔE detectors were used for identification of protons, deuterons and tritons. The SSD telescopes were mounted on a copper frame of a hemisphere shape and placed at backward angles around 135° in the scattering chamber with the inner diameter of 70 cm. The distance between the target and ΔE SSD's was 114 mm and the total solid angle of the SSD array was 3.5 % of 4π. In order to reduce the leakage current, the SSD-Ball system was cooled to about -20 $°C$ with four Peltier elements. The backsides of the Peltier elements were connected to a cooling pipe through which coolant liquids were circulated by a pump outside the scattering chamber. A photograph of SSD-Ball is shown in Fig. 2.9 and a schematic arrangement of the SSD-Ball system is illustrated in Fig. 2.10.

In order to reduce the background caused by the beam halo, a beam halo monitor system consisting of four plastic scintillators was set at about 1 m upstream of the target (see Fig. 2.10). In the beginning of the experiment, the beam was tuned without SSD-Ball to reduce the counting rates of these scintillators. (The actual values were less than 1 kHz at 50 nA when they were set at 2 cm from the beam line.) After getting the clean beam with a small halo, we set the SSD-Ball system

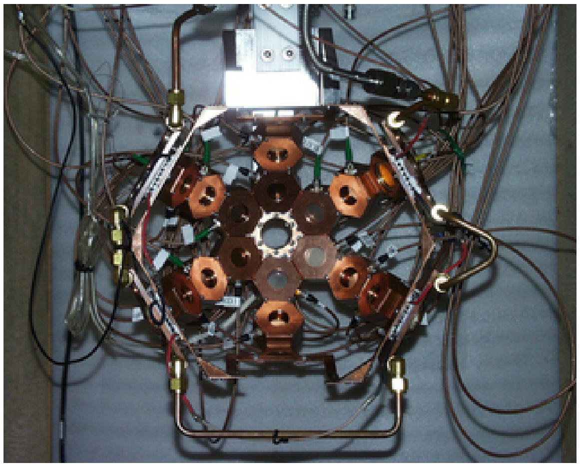

Figure 2.9: Photograph of the SSD-Ball system.

in the scattering chamber and started the decay measurements. The beam intensity was, however, limited to about 70 nA by the maximum counting rate of the SSD closest to the beam. The lowest detectable energies of particles were determined by the thickness of the 100 μm and 20 μm ΔE SSD's and, therefore, were different for each particle (see Tables 3.1 and 3.2). In the analysis, the same energy threshold was set for the 50 μm ΔE SSD as for the 100 μm ΔE SSD.

2.3.2 Targets

In the measurements of charged particle decay, one generally needs a thin target as possible because the energy losses of the emitted particles like α in the target are not negligible. We used a natural carbon target with a thickness of 0.5 mg/cm^2 for the ^{12}C$(p,2p)$ reaction. In the measurements of the ^{16}O$(p,2p)$ reaction, a glass (SiO$_2$) target and a natural silicon (Si) target with each thickness of about 2 mg/cm^2 were employed, and cross sections of the ^{16}O$(p,2p)^{15}$N were obtained after subtracting the Si target runs from the SiO$_2$ runs. Taking into account a long-term shift of the beam condition, SiO$_2$ data and Si data were alternately taken every three hours. We rotated the target through 45° towards LAS in order to increase the $(p,2p)$ yields, where the energy losses of decay particles detected by SSD-Ball were minimized because the target was perpendicular to the axis towards the center of SSD-Ball.

The target thicknesses were measured by means of the dE/dx method with ^{241}Am α-source. The position dependences were also studied with a 1.5 mmϕ collimator. As a result, the uniformity of the thickness was not so good for the Si target. The obtained values are shown in Table 2.6. The errors denoted in the thickness are the maximum deviations from the averaged values.

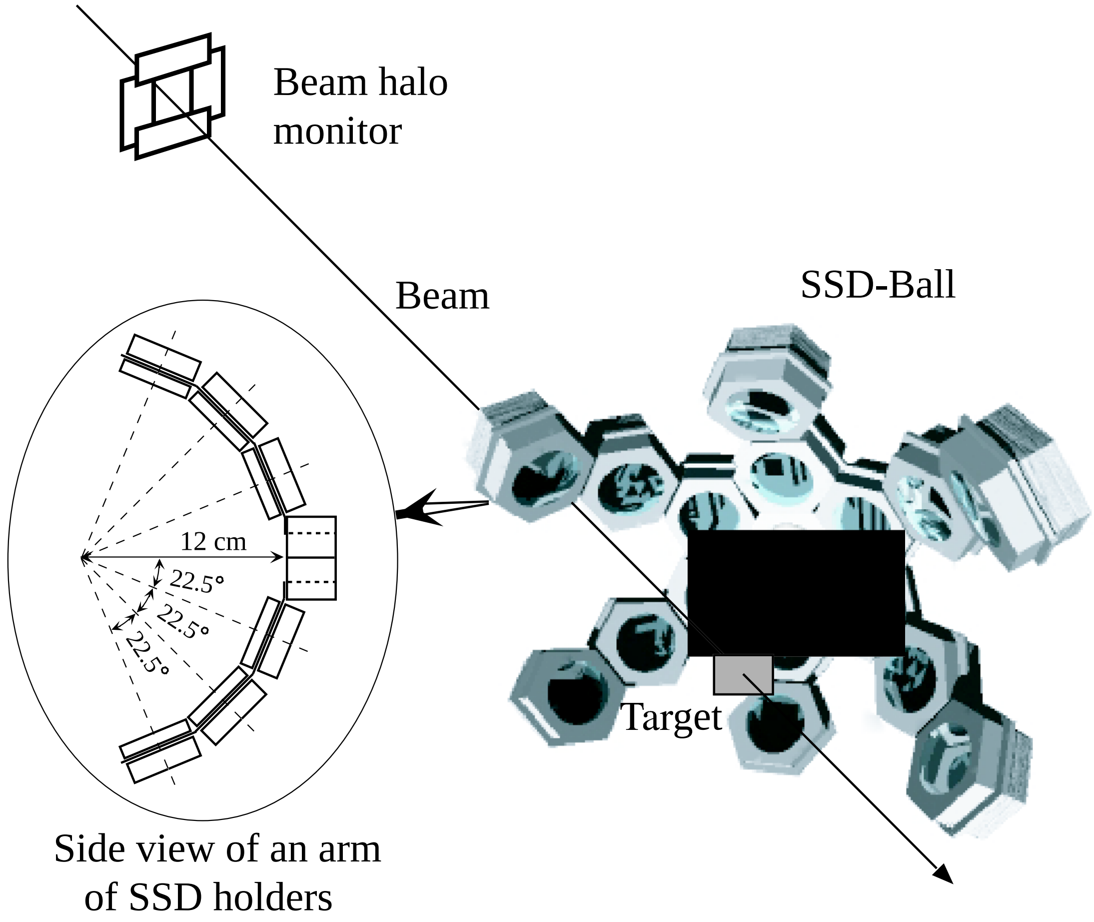

[redacted]

Figure 2.10: Schematic view of the setup of the SSD-Ball system and a beam halo monitor.

Table 2.6: Targets used for the measurements of charged particle decay.

	material	thickness (nominal)	thickness (measured)
^{12}C$(p, 2p)^{11}$B	natural C foil	0.5 mg/cm^2	0.48±0.02 mg/cm^2
^{16}O$(p, 2p)^{15}$N	Quarts glass (SiO$_2$)	8 μm	1.93±0.02 mg/cm^2
	natural Si foil	10 μm	2.42±0.10 mg/cm^2

2.3.3 Readout system of SSD-Ball

A block diagram of the readout electronics of SSD-Ball is shown in Fig. 2.11. All modules except for pre-amplifiers were placed in the rack near the DSR magnet of GR. The pre-amplifiers were put on the scattering chamber in order to minimize the noises caused by long cables. Moreover, ORTEC 142C pre-amplifiers were used for 20μm ΔE SSD's, taking into account the large capacitance of detectors. (HOSHIN pre-amplifiers were used for other SSD's.) Output signals of the pre-amplifiers were transmitted to both timing-filter amplifiers (TFA) and shaping amplifiers (S-Amp). The TFA outputs were sent to CFD's (Phillips 715). Any output of the S-Amp was sent to the Peak Sensing ADC (LeCroy 3351) and one of the CFD outputs was sent to the TDC system (TFC+FERA). An SSD OR signal was generated when there existed at least one CFD output, which was used as the trigger in the SSD test mode (see Fig. 2.7). Even in the decay measurements, a GR+LAS coincidence trigger started the data acquisition system, while a coincidence signal of an SSD OR and a GR+LAS trigger was used only for the gate of the 3351 ADC's.

2.3.4 Data acquisition system

A schematic view of the data acquisition (DAQ) system [66, 67] is shown in Figs. 2.12 and 2.13. The characteristics of this DAQ system is that the CAMAC actions are excluded in the data readout flow and that the VMIC 5576 reflective memory modules (RM5576) with fiber-optic link are used for the data transfer from the front-end parts in the experimental room to the online computer system in the counting room. A data acquisition rate of ∼1 MByte/sec has been achieved. In the present measurements, the DAQ system dealt with the data from the GR-MWDC's, the GR-scintillators, the LAS-MWDC's, the LAS-scintillators, and the SSD-ADC's, separately.

The data flow in the DAQ system was as follows:

- An event header, an event number, and input register words were attached to the data of each line before the data transfer using a special module, named Flow Controlling Event Tagger (FCET) [68]. These were conveniently used in the subsequent event reconstruction.
- The digitized data from each line were transferred in parallel via the ECL buses to high speed memory modules (HSM) in a VME crate without software managements.
- Each line had two HSM's, which worked as a double-buffer and reduced the dead time in transferring buffered data.

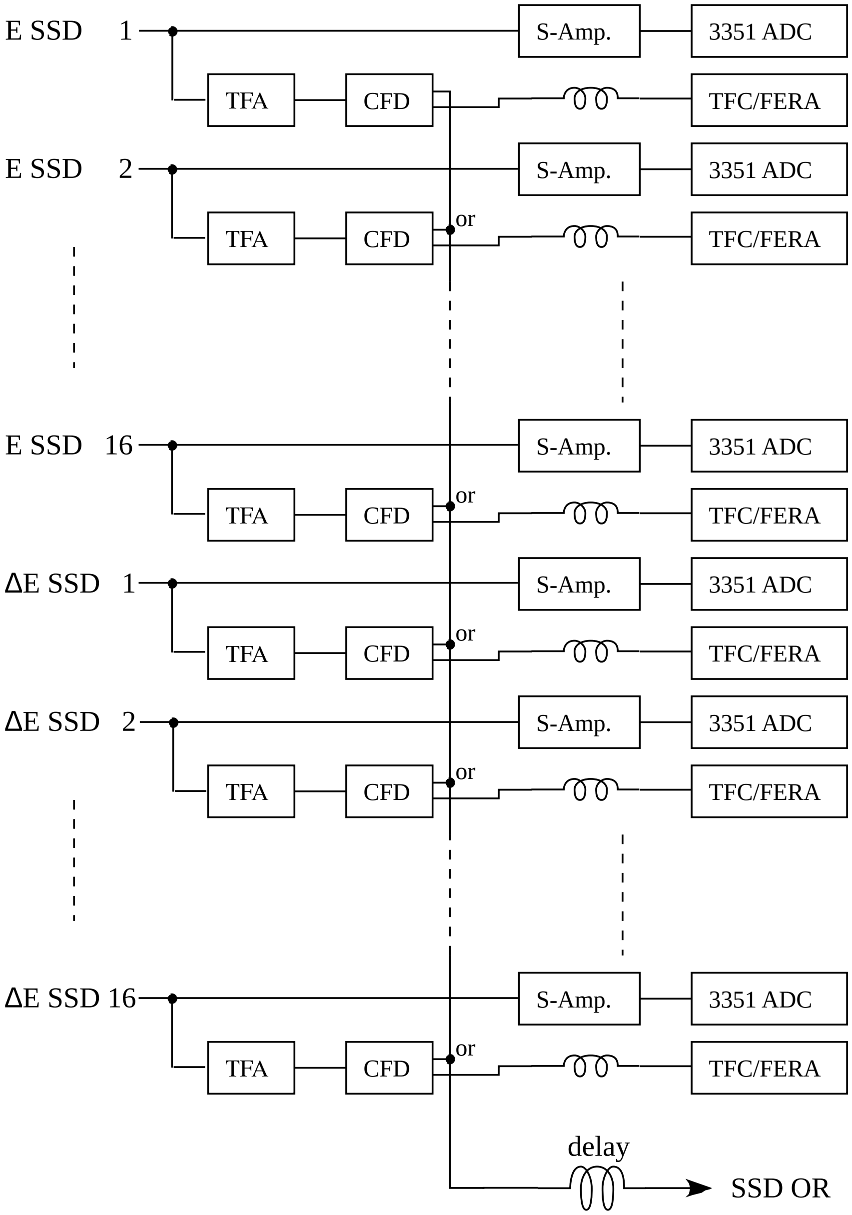

Figure 2.11: Circuit diagram for the SSD-Ball system.

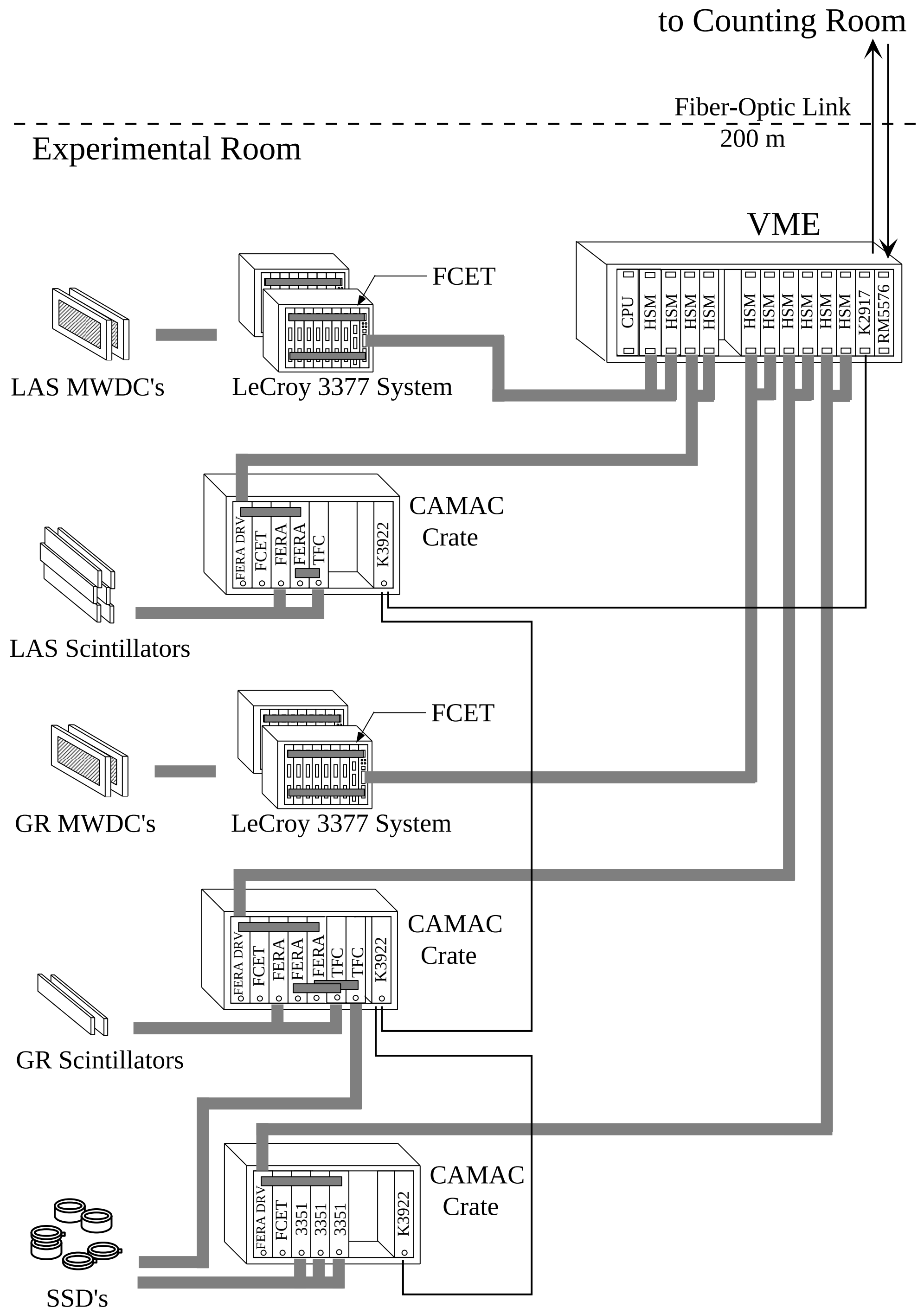

Figure 2.12: Schematic view of the data acquisition system in the experimental room.

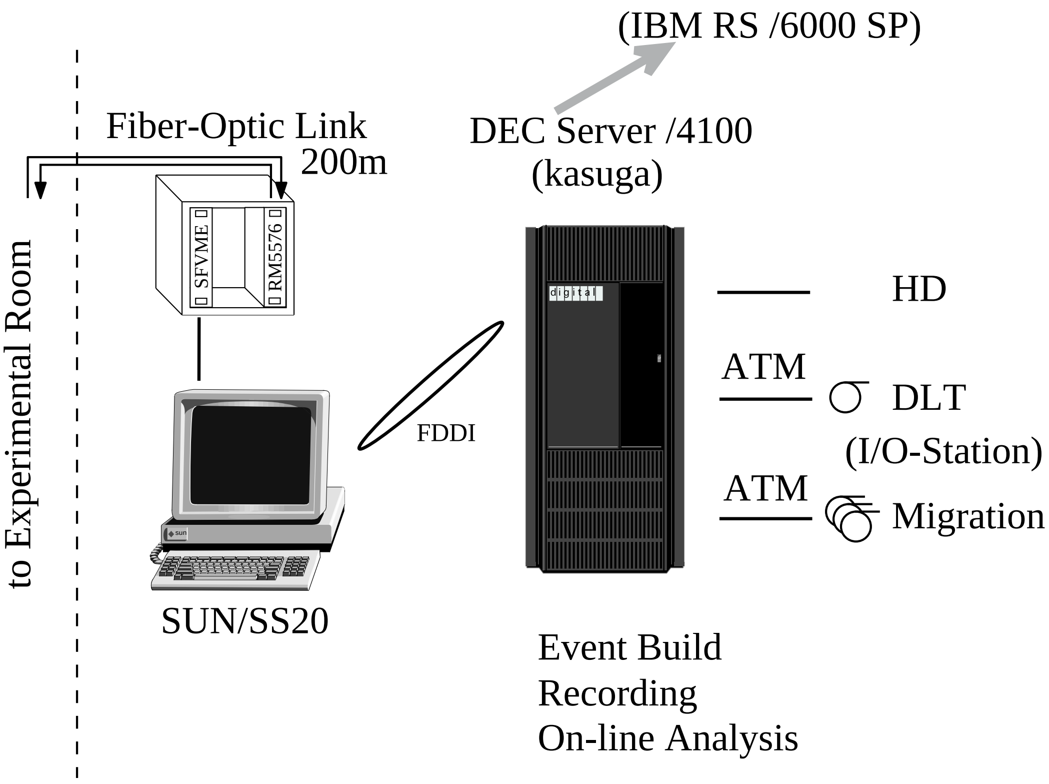

Figure 2.13: Online computer system for the data acquisition in the counting and computer rooms. The DEC computer systems was replace by the IBM system in the neutron decay measurements.

- The stored data in the HSM's were moved to a RM5576 through the VME bus by an MC68040 based CPU board, and the data of the RM5576 was automatically copied to another RM5576 in the counting room through the link of optical fiber cables.
- A SUN work station read the data from the RM5576 and transferred them to a DEC Server/4100 work station via the FDDI line.
- Finally, the data was stored in the large hard disk connected to the work station. The event reconstruction and online data analysis were also performed on this computer.

The online work station was replaced after the first beam time. Then, in the next neutron decay measurements, an IBM work station was used as the main computer. A typical dead time for an event was less than 30 μs. In the present decay measurements, the rate of the GR+LAS coincidence trigger was usually less than 100 Hz and, then, the live time of the DAQ system was more than 98 %.

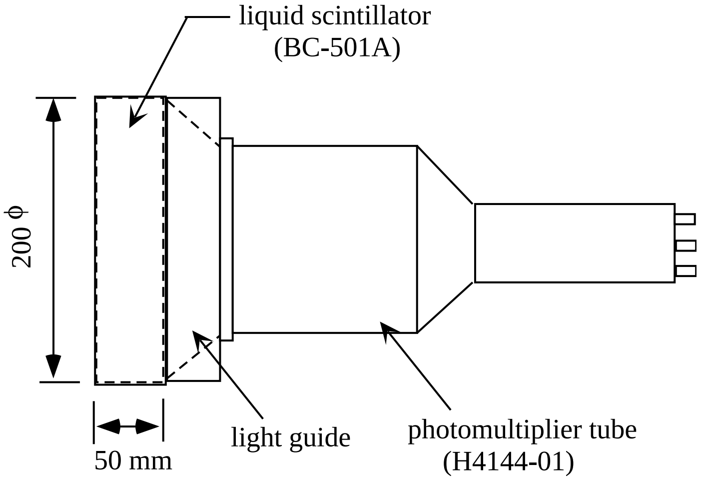

Figure 2.14: Side view of a BC-501A neutron detector.

2.4 Measurements of neutron decay

2.4.1 Neutron detectors

In the second beam time, we measured neutron decay of the s-hole state produced by the $(p, 2p)$ reaction, using a neutron multi-detector array system at RCNP [65]. Owing to the restricted beam time, the measurements were carried out only for the ^{16}O target. The neutron detector array was similar to that of EDEN [69] and consisted of, at maximum, forty-eight BC-501A liquid organic scintillation counters. In the present experiment, thirty BC-501A scintillators were used, because some of the readout circuits were out of order.

Each neutron detector has a scintillator cell with a diameter of 20 cm and a thickness of 5 cm, which is connected to a Hamamatsu H4144 5" PMT through a Pyrex glass window. The scintillating liquid in the BC-501A detector was made of aromatic hydrocarbon (H:C=1.212:1) and was contained in the cylindrical aluminum cell, the inside of which was coated with MgO. A schematic view of a neutron detector is shown in Fig. 2.14.

The BC-501A detector is characterized by the fast response which is suitable to time-of-flight (TOF) measurements and by the good pulse shape discrimination property. The difference of the pulse shape between neutrons and γ-rays is accounted as follows: Some materials like the BC-501A scintillating liquid exhibits a substantial slow component in the pulse shape, while the light emission of most scintillators is dominated by a single fast decay components. A high dE/dx particle increases the slow component, because it produces a high density of excited molecules and increases intermolecular interactions which hinder the normal singlet internal degradation pro-

Table 2.7: Specifications of the BC-501A liquid scintillator.

Cell size	200 mm$\phi\times$ 50 mm$^{\mathrm{L}}$
Cell material	aluminum
Optical window	Pyrex glass
Photomultiplier tube	Hamamatsu H4144-01
H/C (atomic ratio)	1.212
Wave length of maximum emission	425 nm
Decay time (short component)	3.2 nsec

cess. Neutrons are detected by mainly scattering of protons while γ-rays interact through the usual, Compton, photoelectric, and pair creation processes which produce energetic electrons. Thereby, the slow component is enhanced in the neutron detection. The result of the neutron-γ discrimination in the present experiment will be given in § 3.4.2.

Specifications of the BC-501A neutron detector are shown in Table 2.7. The properties of the BC-501A is almost the same as those of the old familiar NE213 detectors [70]. Thus, in the Monte-Carlo simulation to obtain the neutron-detection efficiency, we substitute the NE213 liquid scintillator for the BC-501A (see § 3.4.1).

2.4.2 Detector setup

A schematic view of the setup of neutron detectors and a small scattering chamber is shown in Fig. 2.15. Five neutron detectors were mounted in a steel frame with aluminum spacers adjusted to look toward the target. On the left side of the beam line, six frames were placed at a distance of 2.0 m from the target with the relative angle of 11.25° between neighboring detector frames. A photograph of the neutron detector array is also shown in Fig. 2.16.

Since the wall of the standard scattering chamber was very thick (5 cm aluminum), low energy neutrons emitted from the target would be largely absorbed if we used it. For the neutron and γ-ray measurements, we have newly constructed a small scattering chamber made of stainless steel with a wall thickness of 4 mm. Charged particles decaying at backward angles from the target almost stop in the wall up to the energy of 50 MeV even for protons. Therefore, no counters for the charged-particle veto were prepared in front of the neutron detectors. In order to reduce the energy losses of protons entering the spectrometers, the scattering chamber had two windows on both side of the beam line which were gas-sealed by thin aramid films. The scattering angles between 20° and 80° were covered. Extension pipes, whose ends

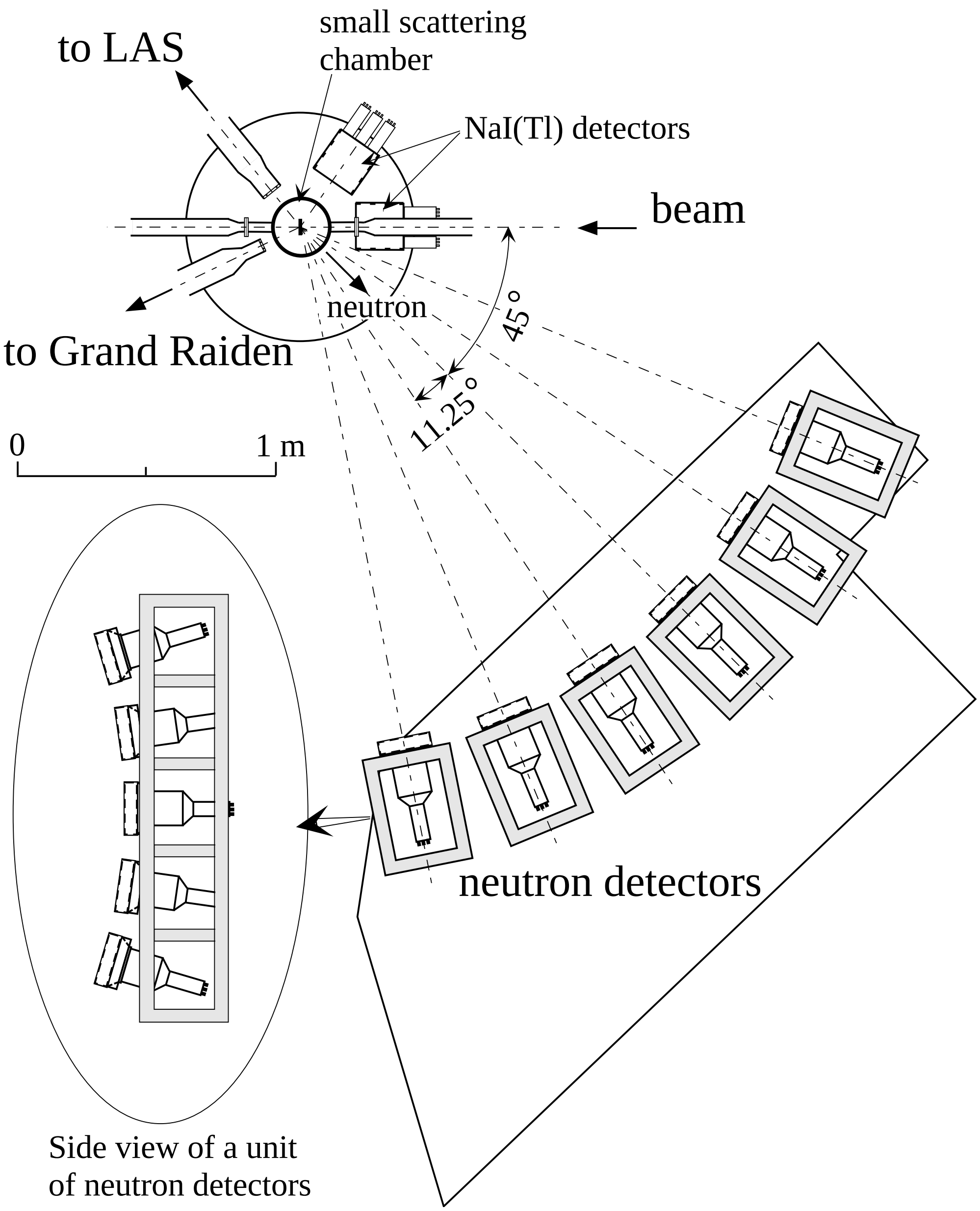

Figure 2.15: Setup of neutron detectors and a small scattering chamber. NaI(Tl) detectors are also placed near the scattering chamber for detecting γ-rays.

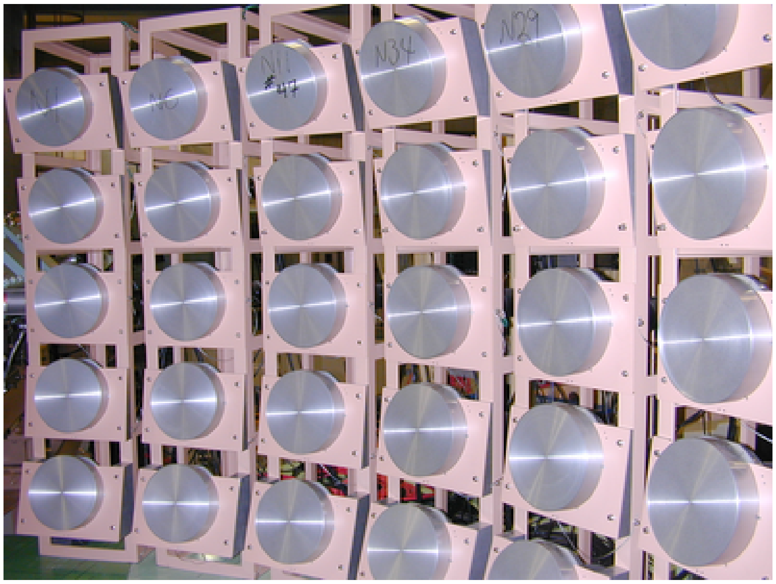

Figure 2.16: Photograph of the neutron-detector array.

were also gas-sealed, were attached to the entrances of both spectrometers.

The deexcitation γ-rays from the hole states of ^{15}N is also interesting in the relation to the nucleon life-time measurements in water Čerenkov detectors. Therefore, three sets of NaI(Tl) γ-ray detector arrays were prepared simultaneously in the neutron decay measurements. Each γ-detector array consisted of nine 5 cm×5 cm×15 cm NaI(Tl) scintillators as shown in Fig. 2.17. Since the γ-decay data are being analyzed by another group, the γ-decay results will not been presented in this paper.

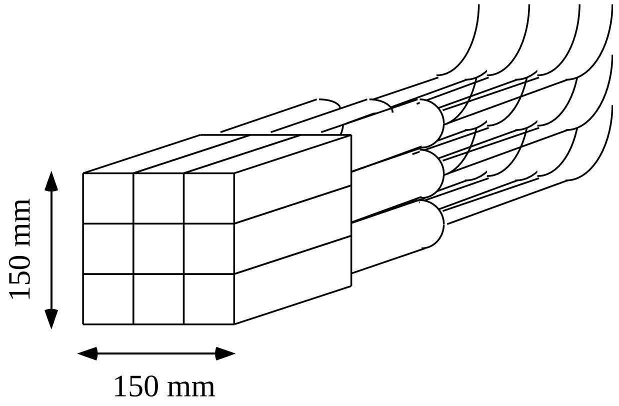

Figure 2.17: Schematic view of a set of 3×3 NaI(Tl) detectors.

2.4.3 H_2O ice target

In the measurements of neutron decay, the thickness of the target is not a serious problem but the detection efficiency and the solid angle are, in general, small compared to the charged particle decay measurements. If one use a chemical compound like SiO_2, separate measurements for the 'contaminant' target are needed to extract the oxygen events. This procedure often deteriorates the statistics and quality of spectra. Therefore, in the present experiment, we adopted an H_2O ice sheet as a background-free oxygen target, which was recently developed by Kawabata *et al.* [71] for the $^{16}O(p,p')$ scattering at forward angles including 0° [72]. The hydrogen contaminants were out of the GR momentum range in the present kinematical setting for the $^{16}O(p,2p)$ reaction.

Two self-supporting ice sheets made of pure water were mounted on the target holder (see Fig. 2.18) and put in the scattering chamber. The ice targets were cooled down to below 140 K by liquid nitrogen (LN_2). The loss of the target material by the sublimation process is negligible at this temperature under the vacuum ($\leq 10^{-3}$ Pa). A schematic view of the target cooling system is shown in Fig. 2.19. LN_2 was periodically transfered from the large LN_2 container to the reservoir connected to the target holder by using an automatic feeding system. The vertical position of the target was remotely changed. The thickness of the ice target used in the experiment was about 40 mg/cm^2 with the uniformity of $\sim$10 %.

2.4.4 Readout system of neutron detectors

The energy of a decay neutron was measured by means of the time-of-flight (TOF) method. The following three kinds of information are needed:

- Flight time from the target to the neutron detector, which determines the velocity of the particle.
- Pulse shape discrimination (PSD) for the separation of neutrons and γ-rays.
- Light-output information corresponding to the detection threshold, because the efficiency is dependent on this threshold energy.

A block diagram of the readout electronics of the neutron detectors is shown in Fig. 2.20. Any output of photomultiplier tube (PMT) was first divided into two signals and one was discriminated by a CFD (LeCroy 3420) and another was sent to a charge sensing ADC (Pantechnik QDC1612F) module. One of the CFD outputs was transmitted to a TDC (Pantechnik TDC812F). Another output of the CFD was sent to a gate-and-delay generator (GDG: CAEN C469), which generated two independent gates for each input. These two outputs were sent to the QDC1612F as a fast gate

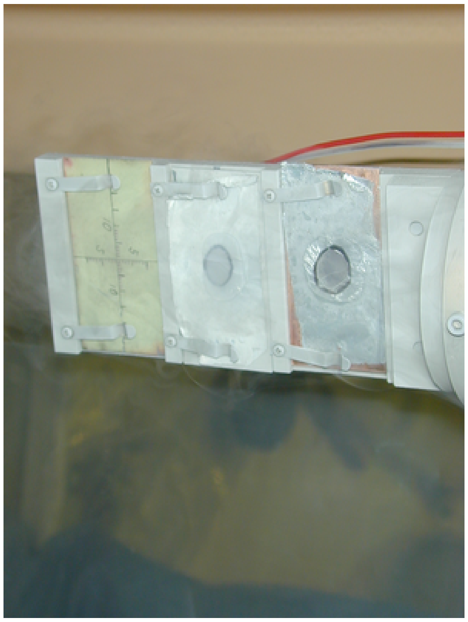

Figure 2.18: Photograph of the ice targets. Each ice sheet built on aluminum foil with a hole (∼10 mmϕ) is mounted on a copper frame.

and a slow gate. The input charge to the QDC1612F was internally divided into two signals (1/6 for the fast gate and 5/6 for the slow gate), and separately converted to create two ADC spectra. The gate timings and widths against the corresponding analog input should be adjusted so that the neutrons and γ-rays are well separated in the two-dimensional spectrum of the fast-ADC versus the slow-ADC. We adopted the same time sequence as that optimized in Ref. [65], which is shown in Fig. 2.21.

The first delay from each neutron detector was adjusted to coincide with the GR+LAS trigger. The CFD worked only during the 500 nsec after the GR+LAS trigger was generated. Because of the path differences in the spectrometers from the target to the focal planes, the trigger timing did not precisely reflect the reaction time at the target. The beam frequency is determined by the radio-frequency (RF) of the AVF cyclotron. Thus, we used the AVF-RF timing, after adjusting the delay to coincide with the GR+LAS trigger, as the start signal of the TDC's for the convenience of subsequent data analysis. The usual RF value is 16.845 MHz for the 392 MeV protons corresponding to the interval of RF pulses of only 59.36 nsec, where the low energy neutron events less than 6 MeV would overlap with the events of next beam bunch in the TDC spectrum. In the present measurements, the beam was reduced by 1/3 with the pulsing magnet between the AVF and Ring cyclotrons so that the bunch interval became 178.1 nsec, which was usable enough for the neutron energy above 0.6 MeV without overlapping.

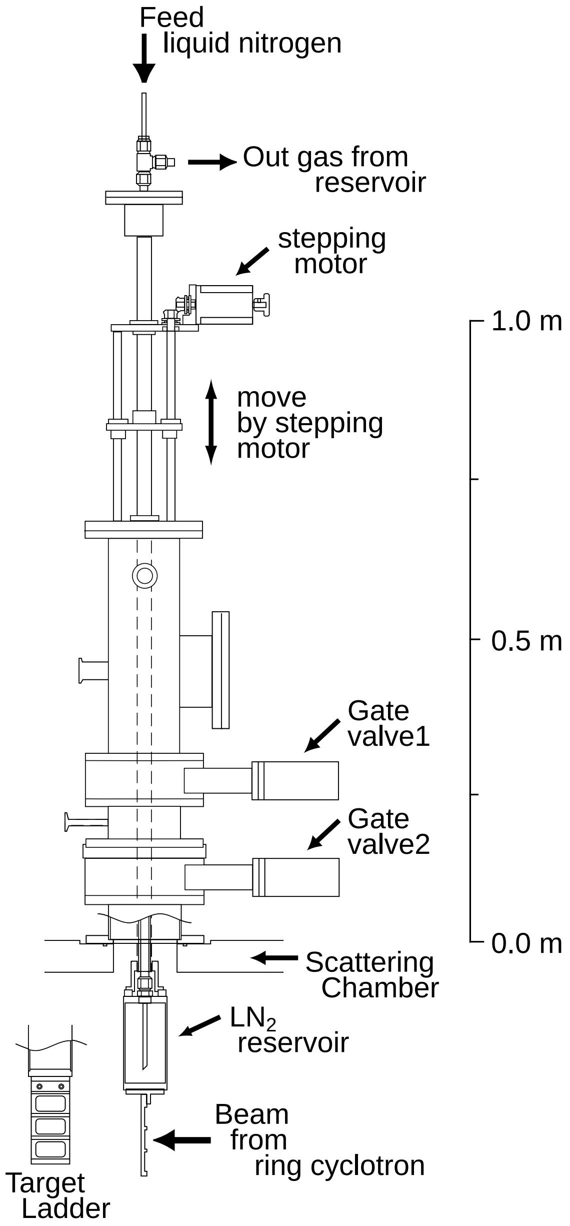

Figure 2.19: Schematic view of the target cooling system installed on top of the scattering chamber. (The figure is taken from Ref. [71].)

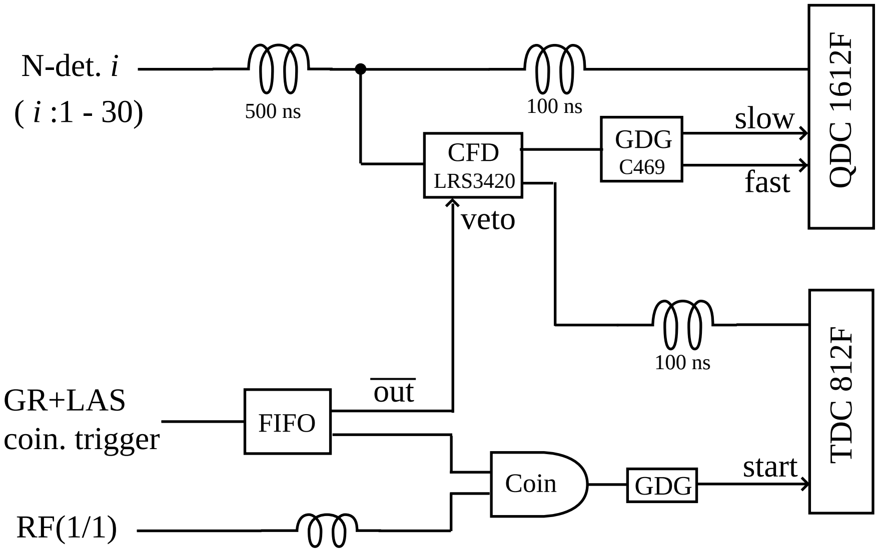

Figure 2.20: Circuit diagram for the neutron detectors.

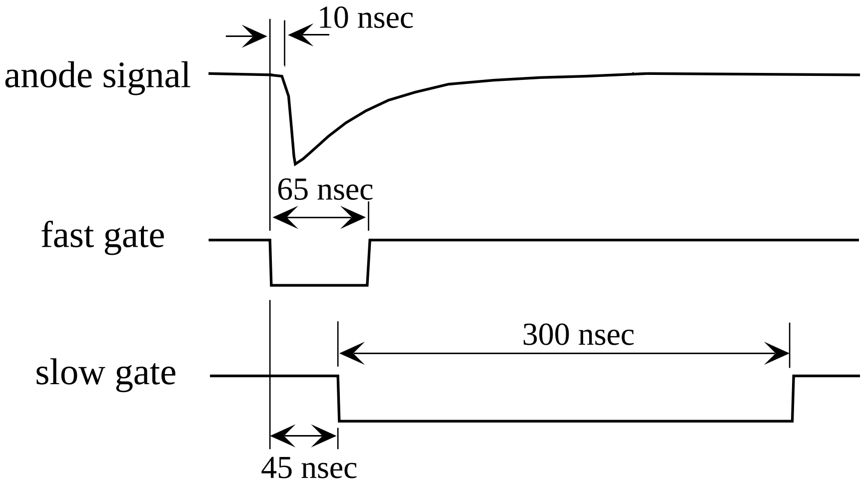

Figure 2.21: Timing chart of the fast and slow gates for an anode signal from the neutron detector.

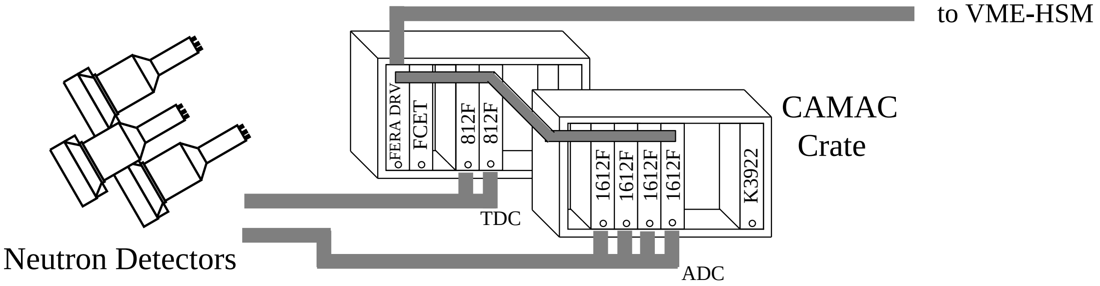

Figure 2.22: Schematic view of the additional part of the data acquisition system for the neutron detectors. (See Fig. 2.12.)

The data from neutron detectors were transfered to the HSM in the VME through the ECL bus, after adding an event header and an event number like other data in Fig. 2.12. Here, only the additional part of the data acquisition system to Fig. 2.12 is shown in Fig. 2.22. The SSD line in Fig. 2.12 was also used for the NaI(Tl) detectors.

Chapter 3

Data analysis and results

3.1 Analyzer program

A program code for the data analysis has been developed, which is called ‘Yosoi-ana’ and widely used for analyzing experimental data obtained at RCNP using GR and/or LAS spectrometer system. This code is used in both the online and offline analysis almost in the same manner. The program first reads a configuration file for spectrum definitions and gate conditions that users need to modify in advance and analyzes a series of data following the instruction of a job-control file. The analyzed results are stored in an HBOOK [73] file and graphically displayed using the program PAW [74].

The data analysis was mainly carried out by using the central computer system at RCNP, namely, old DEC/4100 system and new IBM RS/6000SP system. A part of the analysis was made on PC-Linux computers.

3.2 Energy spectra of $(p, 2p)$ reactions

3.2.1 Plastic scintillation counters

Since particles entering a spectrometer with the same p/Z (momentum/charge) reach the same position at the focal plane, one need to know what kind of particles is coming to the focal plane by using the focal plane detectors. Particle identification was made with the pulse-height information of trigger plastic scintillators (PS1(2) of GR and PS1(2)-u,m,d of LAS). The energy loss of a charged particle in a scintillator depends on its charge (Z), mass (M), and energy (E) as described well by the Bethe-Bloch formula, which is roughly proportional to MZ^2/E. Thus, the energy loss (ΔE) spectrum can be used for the particle identification. (For example, $\Delta E(p)$:$\Delta E(d)$:$\Delta E(t) \approx$ 1:4:9 for the same momentum.)

The primary scintillation photons produced in each scintillator, which were proportional to ΔE, were detected by PMT’s attached on both sides of the scintillator.

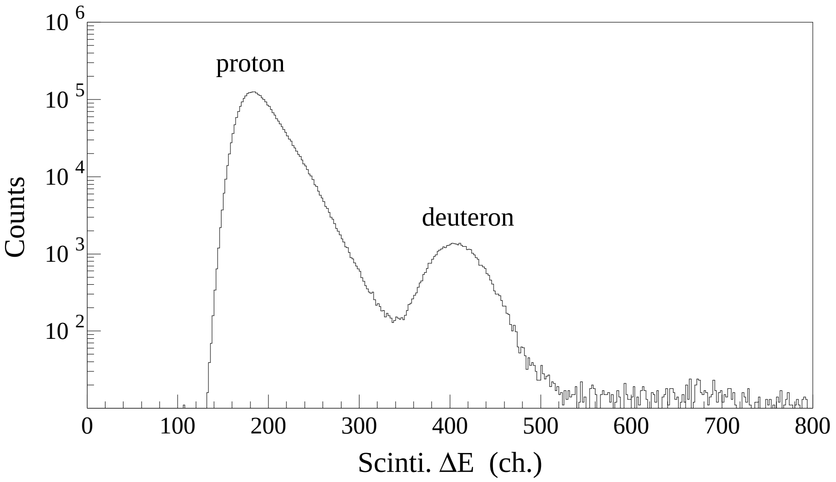

Figure 3.1: Geometrical mean of the pulse-height signals of the left and right PMT outputs from the trigger scintillator (GR-PS1).

Owing to the absorption in the material of the scintillator during the transmission, the photon intensity is attenuated as a function of position x as follows:

$$I(x) = I_0 \exp\left(-\frac{x}{l}\right), \tag{3.1}$$

where I_0 is the initial photon intensity and l is the attenuation length of the material. When the total length of the scintillator is L, the photon intensities at both ends are $I(x)$ and $I(L-x)$, respectively. The outputs of the left and right PMT's (P_L and P_R) are independently proportional to $I(x)$ and $I(L-x)$. If we calculate the geometrical mean of the outputs of two PMT's as

$$P_m = \sqrt{P_L \cdot P_R} \propto \sqrt{I(x) \cdot I(L-x)} = I_0 \exp\left(-\frac{L}{2l}\right), \tag{3.2}$$

P_m is independent of the position x and proportional to initial intensity I_0, *i.e.* proportional to $\mathit{\Delta E}$. Strictly speaking, the coefficient of the linear relation between I_0 and $\mathit{\Delta E}$ is dependent on the type of particle [75] and, moreover, Eq. (3.1) should be slightly modified near PMT's due to another light component with a different attenuation length. However, P_m calculated with Eq. (3.2) was enough to separate protons and deuterons in the present experiment. A sample spectrum for the particle identification in GR-PS1 is shown in Fig. 3.1, where the events in the channels below 350 ch were selected as protons.

The time difference of two PMT's on the both sides of each scintillator also gave rough information on the hit positions with the resolution of ∼1 cm, which were always used for the check of the event consistency between the data of scintillators and those of the MWDC's.

3.2.2 Multi-wire drift chambers

The trajectories of charged particles entering the focal planes of both spectrometers were determined with the GR- and LAS-MWDC's. As shown in Fig. 2.5, the position p of an incident charged particle at an anode plane of the MWDC's is determined from the drift lengths, d_{i-1}, d_i, $\cdots$ of at least more than two wires in the same cluster. (Here, a cluster means that it has at least two adjacent hit wires. Since the X- and γ-rays mostly hit only one wire, background events by photons can be much excluded.) For example, when $|\, d_i \,|$ is the minimum in a cluster with three hits, the position p is simply calculated as

$$p = p_i + l_{WS} \frac{d_{i-1} + d_{i+1}}{d_{i-1} - d_{i+1}}, \quad (d_{i-1} > 0, \;\; d_{i+1} < 0) \tag{3.3}$$

where p_i is the position of i-th wire, l_{WS} is the sense wire spacing, and a negative value is taken for d_{i+1} because electrons moving to $(i-1)$-th wire and $(i+1)$-th wire drift in the opposite direction. In the standard setting of both the GR- and LAS-MWDC's, particles with correct trajectories usually hit more than three sense wires, except for the events with small scattering angles in the region of the low momentum end of the GR focal plane. The incidence angle (θ) are also roughly estimated by $\tan\theta = (d_{i-1} - d_{i+1})/2l_{WS}$ with the angular resolution of about 2°.

A typical TDC spectrum for the X-plane of GR-MWDC1 is shown in Fig. 3.2(a). The drift velocity is almost constant but it considerably deviates near the sense wires due to the steep gradient of the electric field. Since the TDC value only gives the drift time of each wire, one must convert this to the drift length. The so-called x-t calibration was made for each wire plane in the following conditions using the real data taken in the present measurements:

- The histogram of drift length should have a flat distribution up to the anode-cathode gap of 10 mm for the continuum excitation spectrum without sharp peaks.
- The residual distribution defined as

  $$Res = \frac{d_{i-1} + d_{i+1}}{2} - d_i, \tag{3.4}$$

  should be sharply distributed around zero for the correct x-t curve.

The x-t curve obtained for the X-plane of GR-MWDC1 is shown in Fig. 3.2(b). Except for the region of the drift length less than 2 mm, x-t relation was almost linear with the drift velocity of 48 μm/nsec.

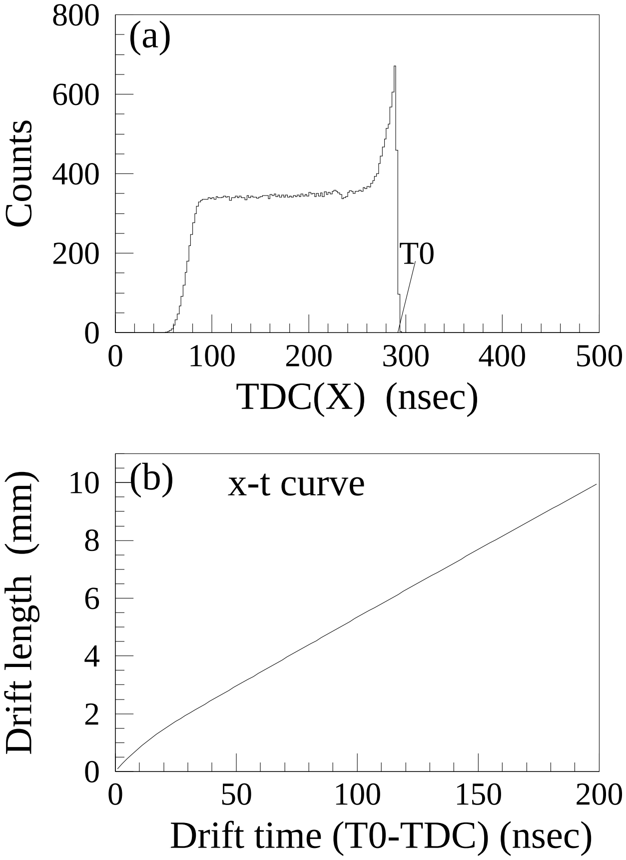

Figure 3.2: (a) TDC spectrum for the X-plain wires of GR-MWDC1. (b) x-t curve for the conversion of drift times into drift lengths.

The residual distribution gives a good index of the position resolution of each plane of the MWDC's. A two-dimensional scatter plot for the residual distribution is shown in Fig. 3.3(a), where the vertical axis denotes half of the distance from the sense wire, and a projected residual distribution is shown in Fig. 3.3(b) for the X-plane of GR-MWDC1. The residual resolution of 330μm (FWHM) was obtained. (For all planes of the GR- and LAS-MWDC's, the resolutions were less than 380μm.) The TDC time resolution of 1 nsec corresponding to $\sim$50μm contributed little to the total resolution. The position resolution δp is dependent on the incidence angle and mostly better than the residual resolution because the intrinsic resolution δd_i of each wire is $\sqrt{6}/3$ of the residual distribution, which is easily deduced from Eq. (3.4). Since the correction was not perfect near the sense wires as seen in Fig .3.3(a), the least square method with all hit wires was not used in determining the position p but Eq. (3.3) was employed in the present analysis. (In the 2-hits cases at the low momentum side of GR, the position was determined as p=p_i+$l_{WS} d_i/(d_i - d_{i+1})$.)

The efficiency of each wire was also estimated as

$$\epsilon_i = \frac{N_{i-1,i,i+1}}{N_{i-1,i+1}}, \tag{3.5}$$

where $N_{i-1,i,i+1}$ is the number of events when three adjacent (i−1,i,i+1)-th wires hit, while $N_{i-1,i+1}$ is the number for the hits of only $(i-1)$-th and $(i+1)$-th wires. The mean hit efficiency was 99.8 % for all planes of the MWDC's. The position resolution of about 300μm corresponded to an energy resolution of 7 keV at E_p= 265 MeV for GR and 10 keV at E_p= 88 MeV for LAS, which was much smaller than the energy spread of the beam ($\sim$250 keV) in the present experiment.

3.2.3 Track reconstruction

Two sets of X and U positions of anode planes can completely determine the three dimensional trajectory of the charged particles. The wire configurations of the X-planes and U-planes of the GR- and LAS-MWDC's are shown in Fig. 3.4 and the relative positions of four anode planes at the focal plane is shown in Fig. 3.5 with their coordinate systems. We define two coordinate systems: the central-ray coordinate in which the z-axis is the momentum direction of the central ray and the focal-plane coordinate in which the z'-axis is perpendicular to the anode planes of the MWPC's. Here, the $z^{(\prime)}$-$x^{(\prime)}$ plane is the median plane of the spectrometer. In both coordinate systems, the center of the X1-plane is taken as the origin. In the focal-plane coordinate system, the horizontal and vertical positions (x', y') and angles $(\theta'_x = \frac{dx'}{dz'}, \theta'_y = \frac{dy'}{dz'})$ of an incident particle are calculated from p_{x1}, p_{u1}, p_{x2}, and p_{u2}, that are obtained using

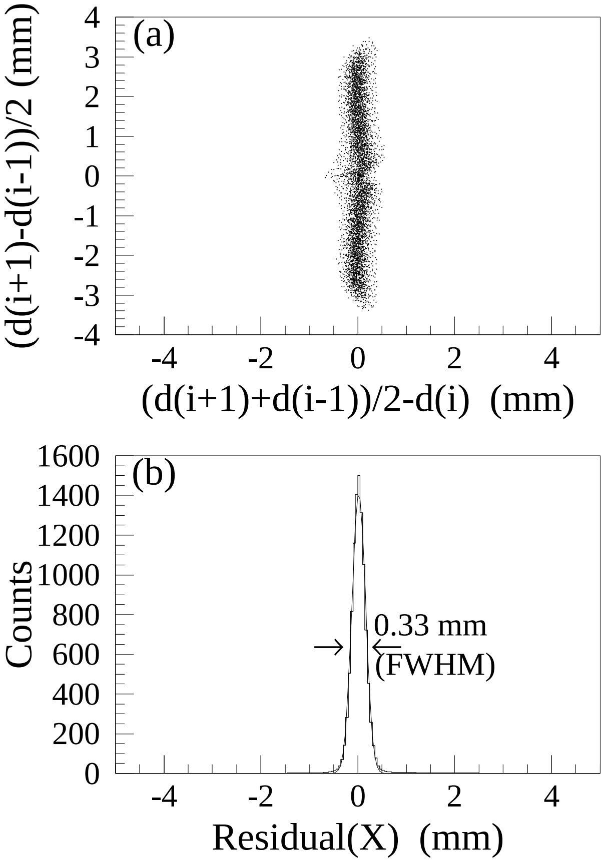

Figure 3.3: Position resolution for the X-plain of GR-MWDC1. (a) Scatter plot for the check of the x-t calibration, where $d(i-1)$, $d(i)$, and $d(i+1)$ indicate the drift lengths for the $(i-1)$-, i-, and $(i+1)$-th wires, respectively, in which the i-th wire has the minimum drift time. Here, $d(i+1)$ takes a negative value (see Fig. 2.5). (b) Residual distribution obtained from projecting the spectrum (a).

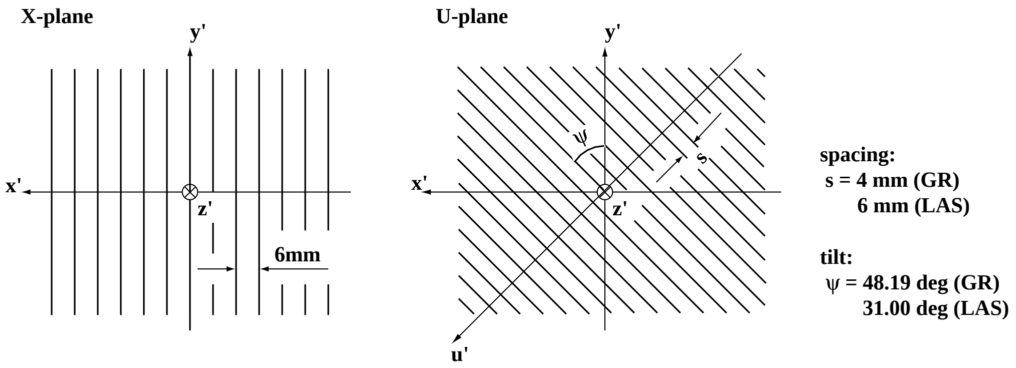

Figure 3.4: Wire configurations of the X-plane and U-plane of the MWDC's. The tilting angle and the spacing of sense wires in the U-planes are different between the MWDC's of GR and those of LAS.

Eq. (3.3).

$$\begin{aligned} \tan\theta'_x &= (p_{x2}-p_{x1})/L_{DC}, \quad \tan\theta'_u = (p_{u2}-p_{u1})/L_{DC}, && (3.6)\\ \tan\theta'_y &= \frac{\tan\theta'_x}{\tan\psi} - \frac{\tan\theta'_u}{\sin\psi}, && (3.7)\\ x'_0 &= p_{x1}, \qquad\qquad u'_0 = p_{u1} - z'_{u1}\cdot\tan\theta'_u, && (3.8)\\ y'_0 &= \frac{x'_0}{\tan\psi} - \frac{u'_0}{\sin\psi}, && (3.9) \end{aligned}$$

where $L_{DC}{=}z'_{x2}{-}z'_{x1}{=}z'_{u2}{-}z'_{u1}$ is the distance of two MWDC's, ψ is the tilting angle of U-planes, and x'_0 (y'_0) is the horizontal (vertical) position at the $z'{=}0$ plane. L_{DC} was 250 mm for GR and 164 mm for LAS. When the position resolution δp is 300 μm and the multiple scattering effect is neglected, the horizontal angular resolution is given as $(0.3\sqrt{2}/250)\cdot\cos^2\theta_{\mathrm{GR}}\approx 0.85$ mr for GR ($\theta_{\mathrm{GR}}\approx 45°$) and $(0.3\sqrt{2}/164)\cdot\cos^2\theta_{\mathrm{LAS}}\approx 0.89$ mr for LAS ($\theta_{\mathrm{LAS}}\approx 54°$), respectively. The vertical position and angular resolutions are worse compared to horizontal ones by ×1.7 for GR and ×2.6 for LAS.

In the central-ray coordinate, the horizontal and vertical angles are converted as

$$\begin{aligned} \theta_x &= \theta'_x - \Theta_{VDC}, && (3.10)\\ \tan\theta_y &= \tan\theta'_y\cos\Theta_{VDC}, && (3.11) \end{aligned}$$

where Θ_{VDC} is the tilting angle of the MWDC's (45° for GR and 54° for LAS). Using the ion-optical matrix, one can trace these angles back to the scattering angles on the target. The focal plane of GR almost agreed with the X-plane of MWDC1, and small aberrations were empirically corrected by looking at some two-dimensional plots like an x-θ_x correlation spectrum. In the case of LAS, the momentum deviation and scattering angle relative to the central ray was obtained from the trajectory at the

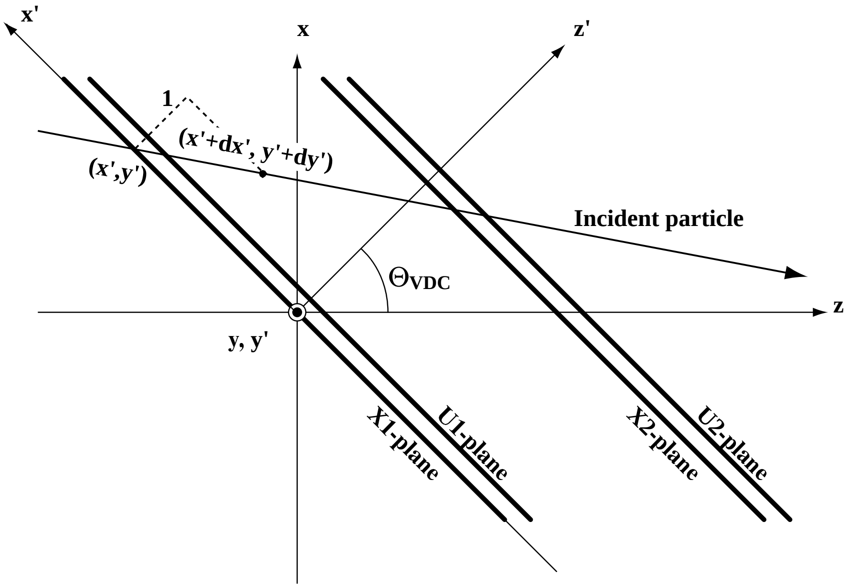

Figure 3.5: Coordinate systems for the ray-tracing with two MWDC's.

focal plane by calculating the 4th-order matrix. The matrix elements of LAS were estimated in a Monte-Carlo simulation [77]. In the present analysis, we used the matrix empirically modified by Noro with use of a sieve-slit calibration.

If an anode plane has more than two clusters, the position p is calculated for every cluster. In the analysis, we required that all the anode planes have one cluster or that only one plane has two clusters but the other three planes have one cluster. Since vertical effective areas of the MWDC are not large owing to the double focusing property of the focal plane, the x-position and u-position in the same MWDC are strongly correlated. Thus, more strongly correlated cluster was chosen in the latter case.

The efficiency of each anode plane was calculated as follows:

$$\epsilon_{X1} = \frac{N_{x1\otimes u1\otimes x2\otimes u2}(E_x)}{N_{u1\otimes x2\otimes u2}(E_x)}, \tag{3.12a}$$

$$\epsilon_{U1} = \frac{N_{x1\otimes u1\otimes x2\otimes u2}(E_x)}{N_{x1\otimes x2\otimes u2}(E_x)}, \tag{3.12b}$$

$$\epsilon_{X2} = \frac{N_{x1\otimes u1\otimes x2\otimes u2}(E_x)}{N_{x1\otimes u1\otimes u2}(E_x)}, \tag{3.12c}$$

$$\epsilon_{U2} = \frac{N_{x1\otimes u1\otimes x2\otimes u2}(E_x)}{N_{x1\otimes u1\otimes x2}(E_x)}, \tag{3.12d}$$

where $N_{x1\otimes u1\otimes x2\otimes u2}(E_x)$ denotes the number of events in which the positions are successfully determined in all four planes, and $N_{u1\otimes x2\otimes u2}(E_x)$ is the number of events in which the position determination only for the X1-plane is failed, and so on. The time-difference spectra from the trigger scintillators can be used as a gate for roughly estimating the position dependence, *i.e.*, the E_x dependence. The position dependence of efficiencies was negligible in the present measurements. The efficiencies of 98 - 99 % were obtained for all planes. The overall tracking efficiency ($\epsilon_{x1} \times \epsilon_{u1} \times \epsilon_{x2} \times \epsilon_{u2}$) was 96 % for GR and 94 % for LAS.

3.2.4 ^{12}C$(p,2p)^{11}$B reaction

The energies of emerging two protons were determined from the focal-plane position spectra of GR and LAS combining with the magnetic field strengths. A two-dimensional spectrum of the proton energies measured with GR and LAS is shown in Fig. 3.6(a) for the ^{12}C$(p,2p)^{11}$B reaction. Several locus lines with constant values of E_p(GR)+E_p(LAS) are observed, which correspond to the states of ^{11}B except for a small contaminant locus of the ground state of ^{15}N. The excitation energy E_x of ^{11}B is obtained from Eq. (2.2) using $T_1(=E_p(\text{GR}))$, $T_2(=E_p(\text{LAS}))$, and the recoil energy T_3 of $^{11}\text{B}^{(*)}$. In the present experiment, T_3 is very small, for example, $T_3 \simeq 0.5$ MeV even for k_3=100 MeV/c. The calculated excitation spectrum of ^{11}B is shown in Fig. 3.6(b). Several discrete states, such as the ground state ($3/2^-$) and the first excited state (2.125 MeV, $1/2^-$), are observed with the energy resolution of 450 keV (FWHM). This resolution was mainly due to the energy width of beam itself and the time fluctuation of the beam energy. The s-hole state is strongly excited in the higher excitation energy region. The bump corresponding to the s-hole state in ^{11}B obviously shows some sub-structures. A similar structure could be seen in the spectrum of the ^{12}C$(e,e'p)^{11}$B experiment at $E_e = 0.5$ GeV [76], although the statistics was not enough to discuss the splitting of the s-hole state. The discussion on this structure of s-hole state will be given in Chap. 4.

As already mentioned in § 2.4.4, the beam from the cyclotron has a bunch structure with ~60 nsec periods. A TDC spectrum for the time difference between the trigger signals of GR and LAS is shown in Fig. 3.7. Each peak corresponds to one beam bunch. A prompt peak includes both the true and accidental coincidence events, while other peaks only include the accidental coincidence events. Assuming the beam has no micro-structures, namely, the same number of protons are included in all beam bunches, the yield of only true coincidence events can be extracted by means of subtracting the events of one of the accidental bunch from those of the true bunch. In Fig. 3.6(b), the accidental events were already subtracted. In the charged particle decay measurements, the accidental coincidence events in the prompt peak were ~1 % of true coincidence events as shown in Fig. 3.7, while they were about 10 % in the neutron decay measurements. The TDC spectrum like Fig. 3.7 must be taken into consideration in the subtraction process of the accidental decay events. In the charged

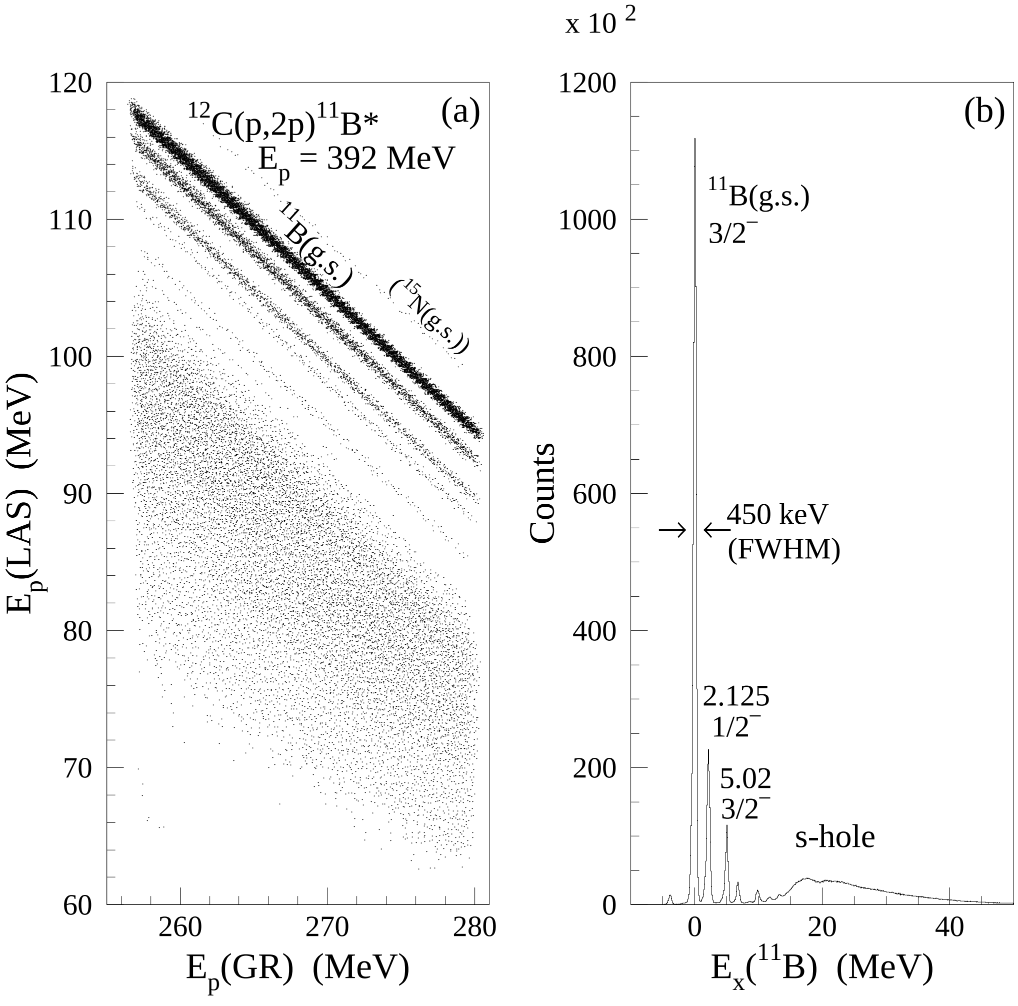

Figure 3.6: (a) Two-dimensional scatter plot of the energies of coincidence two protons measured with GR and LAS in the ^{12}C$(p, 2p)$ reaction at E_p = 392 MeV. All locus lines correspond to the states of ^{11}B except for a small contaminant locus of the ground state of ^{15}N from the ^{16}O$(p, 2p)$ reaction. (b) Excitation spectrum of ^{11}B evaluated by the missing energy in the ^{12}C$(p, 2p)$ reaction after subtraction of accidental coincidence events.

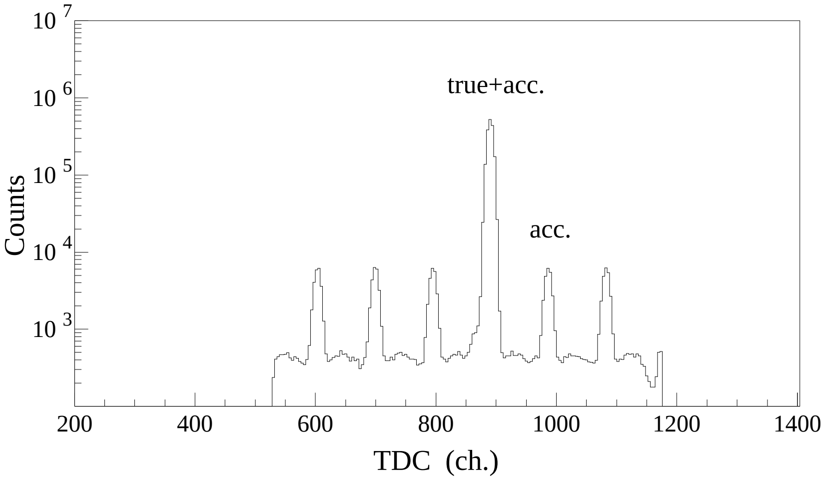

Figure 3.7: TDC spectrum for the time difference between the GR and LAS trigger signals in a measurement of the ^{12}C$(p, 2p)$ reaction.

particle decay measurements, however, we neglected this 1 % effects because the statistical errors of decay particles were much larger than 1 %.

3.2.5 ^{16}O$(p, 2p)^{15}$N reaction

The excitation energy spectrum of ^{15}N via the ^{16}O$(p, 2p)^{15}$N reaction is obtained in the similar way for the ^{12}C$(p, 2p)^{11}$B reaction. In the charged particle decay measurements, the SiO_2 and Si targets were used, while the H_2O ice target was employed in the neutron decay measurements. In the latter, there was a large uncertainty in the target thickness and the energy resolution was not so good partly due to the energy loss of the incident and emerging protons in the thick target. Thus, the energy spectrum of ^{15}N obtained in the first experiment is mainly used in the discussion.

Separation energy spectra of the $SiO_2(p, 2p)$ and Si$(p, 2p)$ reactions are shown in Fig. 3.8(a), where the horizontal axis is taken as the excitation energy of ^{15}N and the spectra below 8 MeV are multiplied by 1/10. The accidental coincidence events were subtracted in the spectra. The spectrum for the Si$(p, 2p)$Al reaction is normalized by the second $3/2^+$ state of ^{27}Al, because there are no states of ^{15}N in this energy region. This normalization factor was consistent with the value that was extracted from the total beam charges and the target thicknesses (listed in Table 2.6) within the errors. The excitation spectrum of ^{15}N obtained by subtracting the Si$(p, 2p)$ spectrum from the $SiO_2(p, 2p)$ spectrum is shown in Fig. 3.8(b). The bump around 16 MeV to 40 MeV is expected to correspond to the s-hole state in ^{15}N, which also seems to have

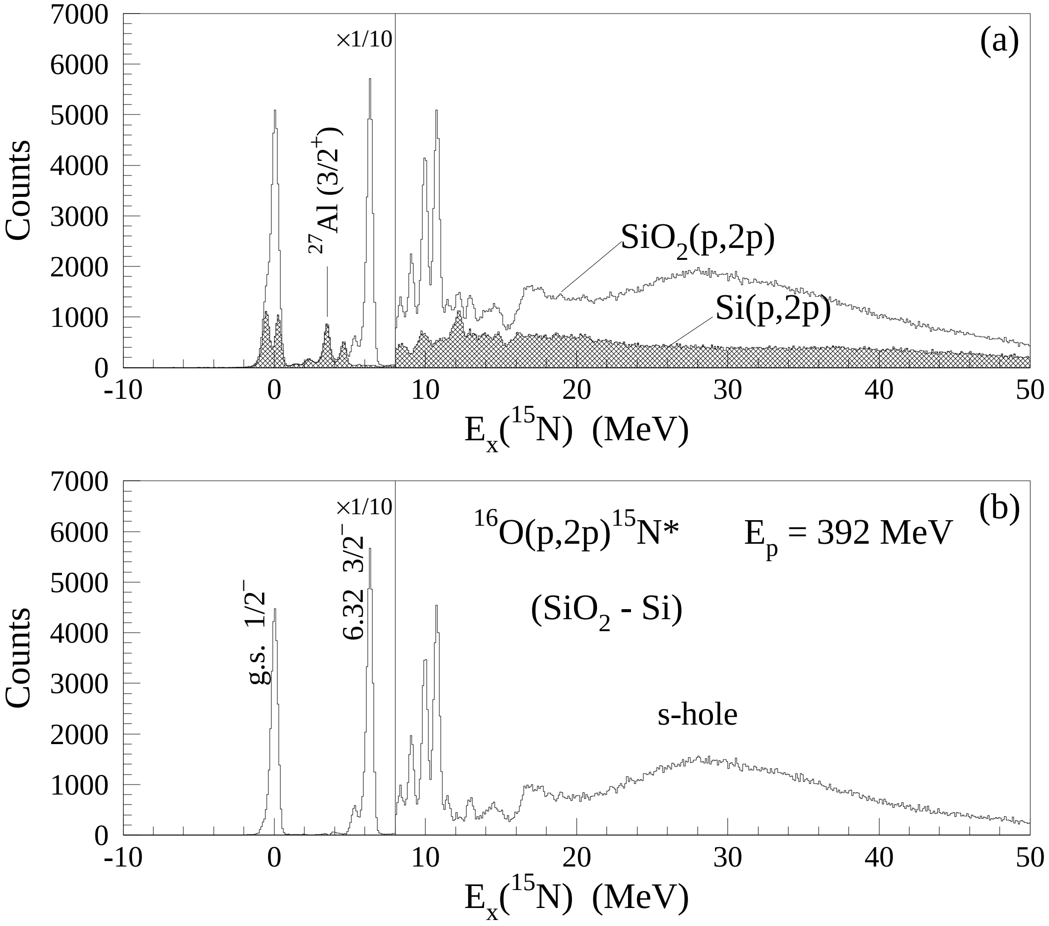

Figure 3.8: (a) Separation energy spectra obtained from the SiO$_2$($p, 2p$) and Si($p, 2p$) reactions. The energies are scaled onto the excitation energy axis of ^{15}N. The spectrum for the Si($p, 2p$) reaction is normalized by the second $3/2^+$ state of ^{27}Al. (b) Excitation spectrum of ^{15}N obtained by subtracting the energy spectrum of the Si($p, 2p$) reaction from that of the SiO$_2$($p, 2p$) reaction.

sub-structures.

An identical spectrum was obtained in the second experiment using a H_2O ice target, if the difference of the energy resolution is taken into account (see Fig. 3.22(a)).

3.2.6 Cross sections and angular correlations

The differential cross section of the $(p, 2p)$ reaction in the laboratory system is written as

$$\frac{d^4\sigma}{d\Omega_1 d\Omega_2 dE_1 dE_2} = \frac{Y}{n_i N_T \mathit{\Delta}\Omega_1 \mathit{\Delta}\Omega_2 \mathit{\Delta} E_1 \mathit{\Delta} E_2 \epsilon \eta}, \tag{3.13}$$

where Y is the $(p, 2p)$ coincidence yield, n_i is the total number of protons in the incident beam, N_T is the number of target particles per unit area, ϵ is the detection efficiency, and η is the live time ratio of the data acquisition system. $\mathit{\Delta}\Omega_{1,2}$ are the solid angles of the spectrometers, and $\mathit{\Delta}E_{1,2}$ are the energy ranges. As mentioned before, $\mathit{\Delta}\Omega_{1,2}$ were slightly ambiguous because the entrance slits of both spectrometers were fully opened in the coincidence measurements with decay particles. Therefore, the measurements of the $(p, 2p)$ reaction with slits defining the solid angles of GR and LAS to 2.4 msr and 12.0 msr, respectively, were separately performed for the normalization of the absolute cross section. Moreover, the energy range of GR was restricted within 12.5 MeV by the offline cut taking into account the small decrease of the acceptance near the both edges of focal planes, while the data with the full energy ranges of GR and LAS are used in the case of the decay analysis. Because the cross sections of the discrete p-hole states are largely dependent on the acceptance in the present kinematical setting, the s-hole yield of the excitation energy of ^{11}B between 16 MeV and 35 MeV was used for the normalization in the ^{12}C$(p, 2p)$ reaction. (The yield of E_x=16 to 40 MeV was used in the ^{16}O$(p, 2p)$ reaction.) Although the cross section of the s-hole state is very flat, the acceptance dependence was still corrected by using the results of distorted wave impulse approximation (DWIA) calculations (for the DWIA calculation, see § 4.2.1). The solid angle of LAS was studied in detail by Okihana *et al.* [77] and they obtained averaged value of ∼20 msr for the full opening case. When using this value, the averaged solid angle of GR was estimated from the above normalization procedure. The obtained value is ∼4.3 msr, which agrees with that used in Ref. [78].

The differential cross sections calculated with $\mathit{\Delta}\Omega_1$=4.3 msr, $\mathit{\Delta}\Omega_2$=20.0 msr, and $\mathit{\Delta}E_1$=12.5 MeV, are shown in Fig. 3.9 with $\mathit{\Delta}E_2$=0.1 MeV bins for both the ^{12}C$(p, 2p)^{11}$B and ^{16}O$(p, 2p)^{15}$N reactions. In Fig. 3.9(a), the portion of the small oxygen contaminant seen in Fig. 3.6 was subtracted using the ^{16}O$(p, 2p)^{15}$N spectrum (Fig. 3.9(b)). The systematic errors of the absolute cross sections are estimated to be 10 % to 15 %, which are due to the uncertainties of the target thicknesses (including

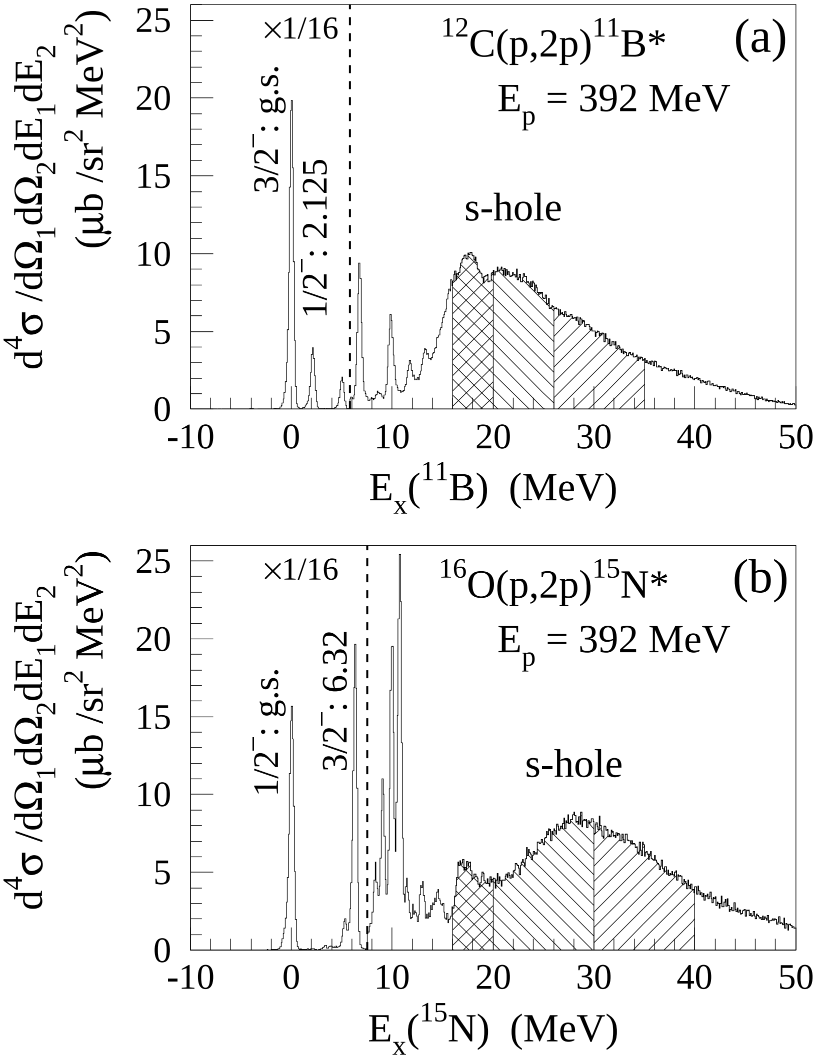

Figure 3.9: Energy spectra of the differential cross sections of (a) ^{11}B produced by the ^{12}C$(p,2p)^{11}$B* reaction and (b) ^{15}N produced by the ^{16}O$(p,2p)^{15}$N* reaction at E_p = 392 MeV. Decay fragments from the hatched regions are mainly studied for both the s-hole states.

contaminant subtractions) and charge collections and the acceptance normalization mentioned above. In the higher excitation energies, the detection efficiencies decrease gradually in both reactions due to the finite momentum acceptance of the spectrometers. Moreover, in the decay measurements, the decay particles were detected mostly for the excitation energy above ~16 MeV. Therefore, the hatched regions of the *s*-hole states in both Fig, 3.9(a) and (b) are studied in the decay analysis, which are further separated into three regions in order to investigate the sub-structures of the *s*-hole states.

In the second beam time, we also measured the angular correlation of the *s*-hole state in the $^{16}\mathrm{O}(p,2p)^{15}\mathrm{N}$ reaction for $30^\circ \leq \theta_{\mathrm{LAS}} \leq 65^\circ$ corresponding to the recoil-momentum dependence of -100 MeV/c to 150 MeV/c. At $\theta_{\mathrm{LAS}}= 60^\circ$, huge background events originating in the *p*-*p* scattering from the hydrogen of the $\mathrm{H_2O}$ target reached the GR focal plane due to re-scattering in the spectrometer, although the true *p*-*p* events come out of the momentum range. Thus, the 60° data was not used in the analysis. Since the thickness of the $\mathrm{H_2O}$ ice target has a relatively large uncertainty, the angular correlations are scaled using the data at $\theta_{\mathrm{LAS}}= 51.0^\circ$, where the cross section is determined by normalizing the results in the first beam time. The measured angular correlations will be shown in Fig 4.4 in § 4.2.2 together with the results of the DWIA calculations.

3.3 Charged particle decay

3.3.1 Particle identification

Charged particles decaying from the *s*-hole states in $^{11}\mathrm{B}$ and $^{15}\mathrm{N}$ were detected by the SSD-Ball system consisting of sixteen $\mathit{\Delta E}$-E SSD telescopes. The gain factors of the S-AMP's for all the SSD's were calibrated using a $^{241}\mathrm{Am}$ α-source and the offsets of the ADC's were determined from the pulser data. Typical two-dimensional spectra of $\mathit{\Delta E}$ versus $\mathit{\Delta E}+E$ obtained for the $^{12}\mathrm{C}(p,2p)$ reaction are shown in Fig. 3.10 for both the telescopes with a thick $\mathit{\Delta E}$ (100 μm) and a thin $\mathit{\Delta E}$ (20 μm). In the set with the 100 μm $\mathit{\Delta E}$ (Fig. 3.10(a)), the locus curves corresponding to p, d, and t are clearly seen from the left-down side toward the right-up side and also the loci of ^{3}He and α can dimly be seen. On the other hand, in the set with the 20 μm $\mathit{\Delta E}$ (Fig. 3.10(b)), p, d, and t were not separated and the locus of α is seen in the upper part with a weak ^{3}He locus. These spectra includes accidental coincidence events with several bunches in order to plot with enough statistics.

Since a few $\mathit{\Delta E}$-E telescopes did not show the good two-dimensional spectra like Fig. 3.10, six 20 μm $\mathit{\Delta E}$'s, five 100 μm $\mathit{\Delta E}$'s, and a 50 μm $\mathit{\Delta E}$ were used in the following analysis. Moreover some of the E-SSD's were found to have much different

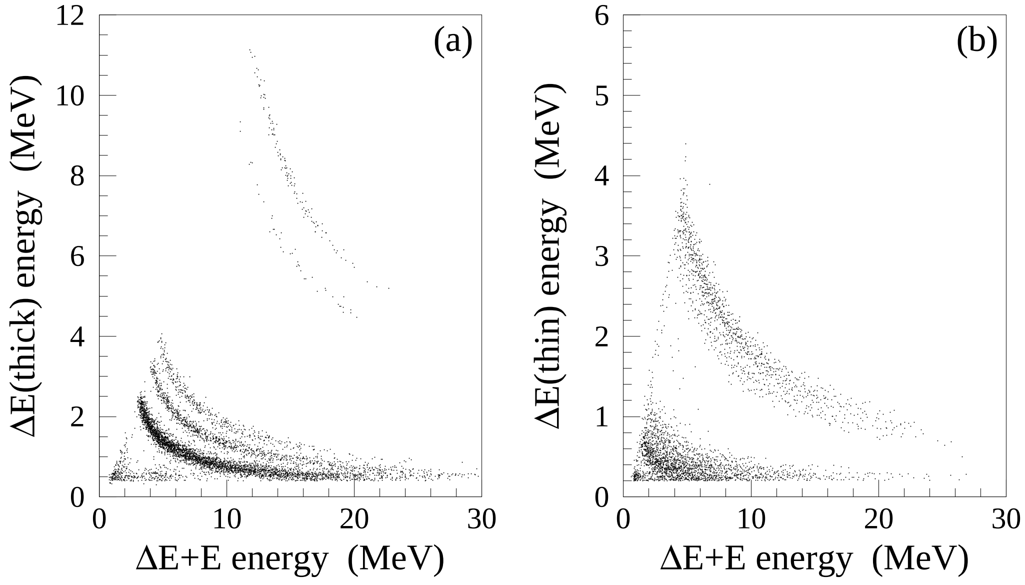

Figure 3.10: (a) Two-dimensional scatter plot of the energy loss in a 100 μm $\mathit{\Delta E}$-SSD versus the summed energy in its $\mathit{\Delta E}$-E telescope. (b) The same as figure (a), except for a 20 μm $\mathit{\Delta E}$-SSD.

effective areas from the nominal values (450 mm^2). We calibrated the actual effective areas of the E-SSD's from the data of the gain calibration of the E-SSD's that was measured with the ^{241}Am α-source placed at the target point, *i.e.*, the center of the hemisphere frame. For the telescopes with the 300 mm^2 $\mathit{\Delta E}$'s, the solid angles are determined by the effective areas of $\mathit{\Delta E}$'s. As the result, it was estimated with the errors of about 5 % that the total solid angle of six sets of the $\mathit{\Delta E}$-E telescopes with the thin (20μm) $\mathit{\Delta E}$'s used in the analysis was 161 msr and that of other six sets was also 161 msr.

In order to identify decay particles, we calculated a useful value PI defined as

$$\mathrm{PI} = \frac{(E + \mathit{\Delta E})^{1.73} - E^{1.73}}{(\text{arb. factor})} \times (\text{small correction}). \tag{3.14}$$

Using this, the same particles have almost the same PI values independently of their energy. Fig. 3.11(a) and (b) show a typical two-dimensional plot of $\mathit{\Delta E}$ versus PI and a projected PI spectrum for a 100 μm $\mathit{\Delta E}$-E telescope. A small correction factor is determined so as to vertically straighten each locus of two-dimensional plot. Three peaks corresponding to p, d, and t are well separated. In Fig. 3.11(c) and (d), the similar figures are shown for a 20 μm $\mathit{\Delta E}$-E telescope. The α events are separated from the p, d, and t events but are not completely discriminated from the

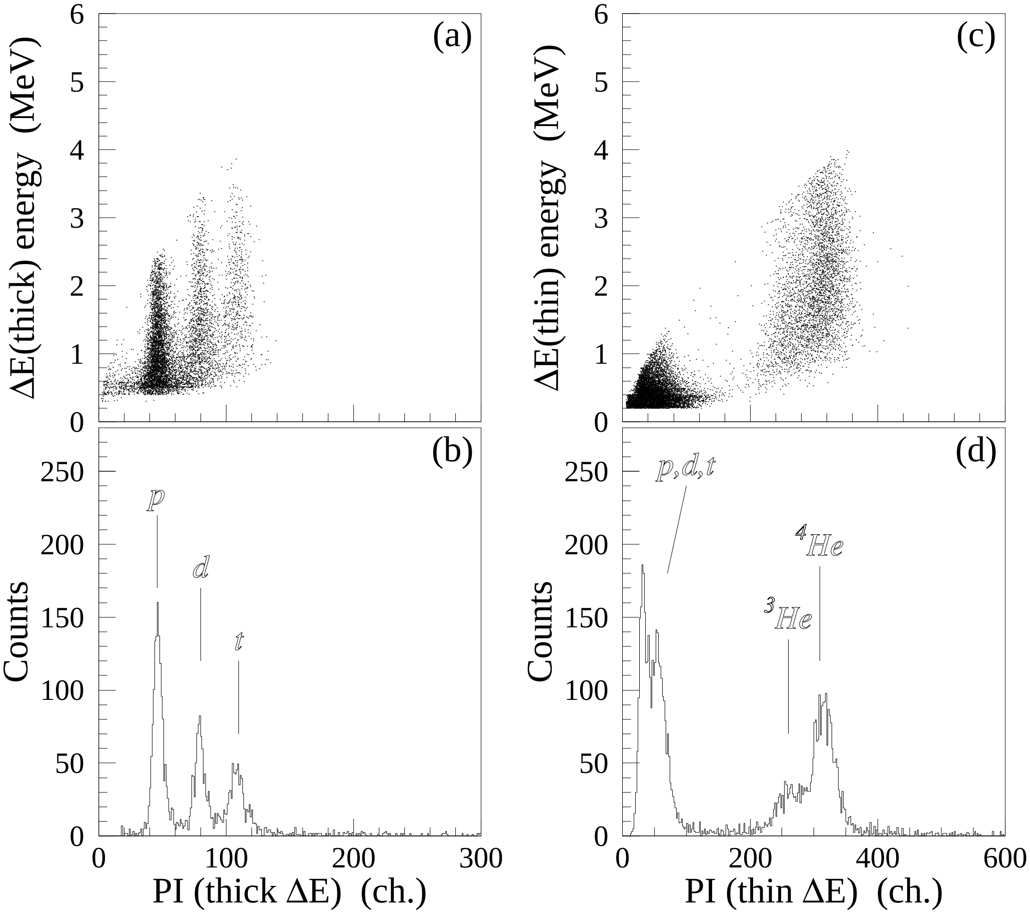

Figure 3.11: Particle identification (PI) with ΔE-E telescopes. (a) A two-dimensional scatter plot of the energy of ΔE versus PI and (b) its projection spectrum onto the PI axis for a 100 μm ΔE-SSD. (c) and (d) are the same as panels (a) and (b), respectively, except for a 20 μm ΔE-SSD.

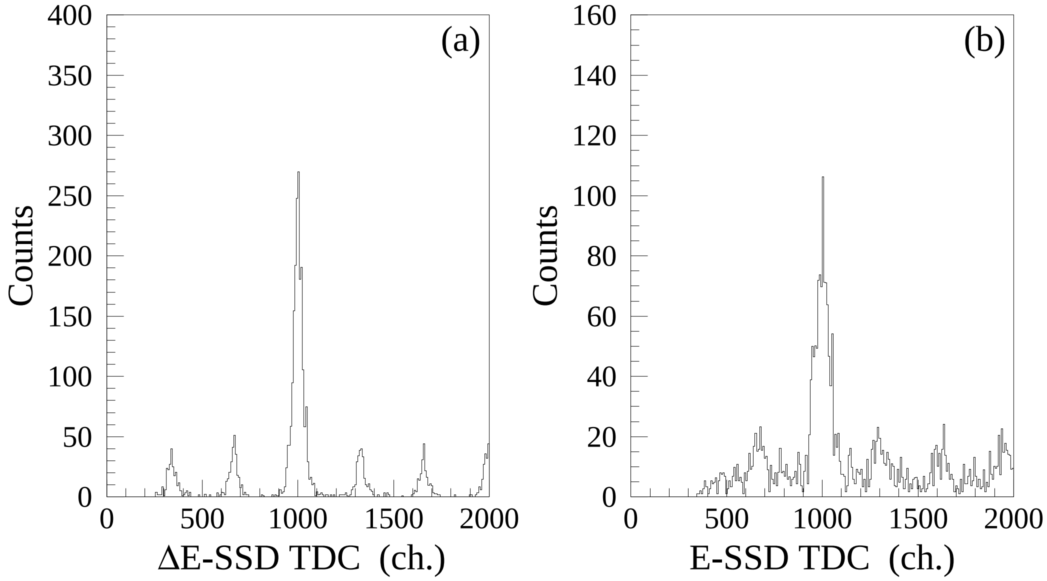

Figure 3.12: (a) TDC spectrum after the pulse-height corrections for a 20 μm $\mathit{\Delta E}$-SSD. (b) The same figure as (a), but for a 5 mm E-SSD.

^{3}He events. The ^{3}He events are, however, almost vanished when we select the true triple coincidence events, because the decay threshold energy of ^{3}He is very high in both ^{11}B and ^{15}N. In the analysis, the possible ^{3}He events are included in the α events.

As mentioned in § 3.2.4, accidental $(p, 2p)$ coincidence events in the prompt peak of the TDC spectrum are only 1 % in the charged particle decay measurements and, then, the true $(p, 2p)$ events can be selected by this prompt peak. Hence, we neglect the 1 % $(p, 2p)$ accidental coincidence because the statistical uncertainties of charged particle decay events are much large compared to this 1 % effect. TDC spectra of a 20 μm $\mathit{\Delta E}$-SSD and a 5 mm E-SSD after selecting the true $(p, 2p)$ coincidence events are shown in Fig. 3.12. These TDC spectra have already been corrected for the pulse-height dependence of time by using the TDC-ADC correlations caused by the time difference of particles with different energies. The ratio of the prompt events to the accidental events is about 5. If we used the coincidence of the both the true bunches in the $\mathit{\Delta E}$- and E-TDC's as a gate, the event with small energy deposit in the $\mathit{\Delta E}$- or E-SSD would be excluded due to the threshold of the discriminator. In the analysis, the true(+accidental) gate is defined as that the event is in the true bunch of the $\mathit{\Delta E}$-TDC, or in the true bunch of the E-TDC with no data of the $\mathit{\Delta E}$-TDC. The accidental gate for one of the other bunches is similarly defined as that the event is in the corresponding accidental bunch of the $\mathit{\Delta E}$-TDC, or in the same accidental bunch of the E-TDC with no data of the $\mathit{\Delta}E$-TDC. For the subtraction of the accidental events, we used the averaged number of events in the first and second accidental bunches after the true bunch because the bunch just before the true bunch might include true coincidence events with fast electrons.

3.3.2 Charged particle decay of the s-hole state in ^{11}B

The energy spectra of ^{11}B in coincidence with decay particles are shown in Fig. 3.13(a). Accidental coincidence events were subtracted. The threshold energies (E_{th}) of 2-body decay from ^{11}B to the channels ^{10}Be+p, ^{9}Be+d, ^{8}Be+t, ^{8}Li+^{3}He and ^{7}Li+α are 11.2, 15.8, 11.2, 27.2 and 8.7 MeV, respectively. The ^{3}He-decay events, which are hardly expected due to its large threshold energy, are included in the α-decay portion as mentioned before. It is apparent in Fig. 3.13(a) that the triton contribution is the largest, although the Q-value is smaller than that of α-decay.

If the momentum of ^{11}B* with an excited energy of E_x is 0 MeV/c, the energy of a decay particle (E_{dcy}) is given by

$$E_{dcy} = \frac{m_{dcy}}{m_{dcy} + M^*_{res}}(E_x - E_{th}), \tag{3.15}$$

where m_{dcy} is the mass of the decay particle and M^*_{res} is the mass of the residual nucleus including the excitation energy.

The panels (a), (b), (c) and (d) in Fig. 3.14 show four two-dimensional spectra of the energies of p-, d-, t- and α-decay particles versus the excitation energy E_x of ^{11}B, where the lines calculated using Eq. (3.15) for the ground state (M^*_{res}=M_{res}) are also shown. The loci corresponding to the ground states in the residual nuclei are clearly observed in all spectra. The projection spectra onto the excitation energy axes of the residual daughter nuclei are shown in Fig. 3.14(e), (f), (g) and (h). The peaks populating low-lying states up to the excitation energy of about 5 MeV in each nucleus indicate that those events occur mainly through a binary decay process, while events in the higher excited region include the 3-body decay and sequential decay processes. The energy resolution of the ground state peak of ^{10}Be is 1.1 MeV (FWHM) and the resolution gradually worsens as the mass of the decay particle increases. These values are much larger than the energy resolution of the $(p, 2p)$ reaction (450 keV) and also than the resolution of SSD's ($\leq$50 keV for the 5.5 MeV α particles). The main part of the above resolution comes from the small recoil momentum of ^{11}B distributed around zero, and a part of it is due to the energy loss of the decay particle in the target.

The experimental differential cross sections and the branching ratios of decay particles are listed in Table 3.1. The excitation energy region is restricted to the

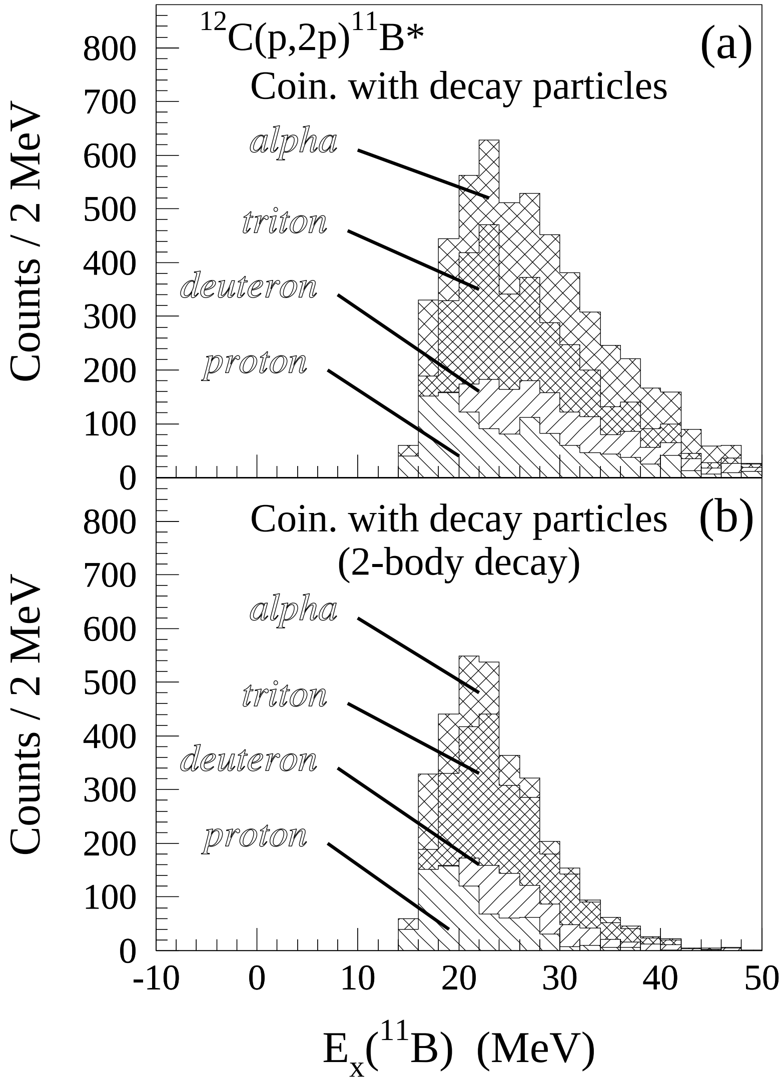

Figure 3.13: (a) Excitation energy spectra of ^{11}B in coincidence with decay charged particles. The contributions of the p-, d-, t- and α-decays are separately shown. (b) The same figure as (a), but for the decay onto the ‘2-body decay’ regions (see text).

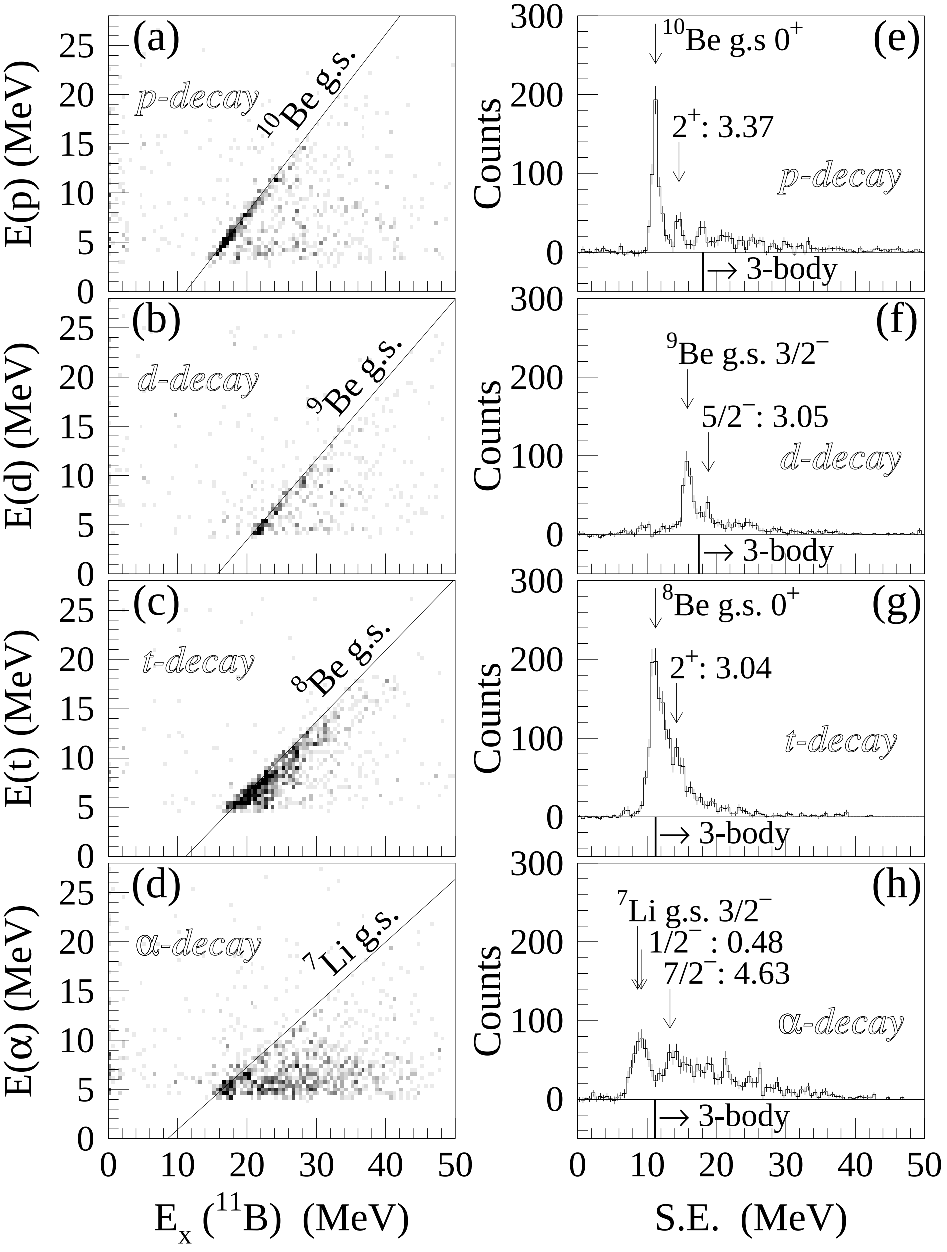

Figure 3.14: The left side panels show two-dimensional plots of the energies of the decay particles versus the excitation energy E_x of ^{11}B for (a) p-, (b) d-, (c) t- and (d) α-decay channels. The locus lines for the ground states in the corresponding residual nuclei are shown. The right side panels display separation energy spectra for the final states of (e) ^{10}Be, (f) ^{9}Be, (g) ^{8}Be and (h) ^{7}Li obtained from projecting events in panels (a), (b), (c) and (d) onto the excitation energy axes of the residual nuclei, respectively. The threshold energies of the 3-body decay channels are indicated.

Table 3.1: Measured differential cross sections of the s-hole state in ^{11}B and the branching ratios of decay particles are listed. Only statistical errors are shown. The branching ratios of the decay onto the '2-body decay' regions are given in parentheses (for further details see text).

$E_x(^{11}\mathrm{B})$	$d^3\sigma/d\Omega_1 d\Omega_2 dE$ †		Branching ratio (%) ‡				
(MeV)	(μb/sr^2 MeV)		p	d	t	α	
16 – 35	128.7		11.7±0.6	6.5±0.4	18.6±0.6	16.8±0.6	
		(	8.5±0.5	5.3±0.3	16.4±0.6	7.7±0.4	)
16 – 20	36.3		13.6±1.1	0.0±0.04	9.1±0.8	11.3±1.0	
		(	13.6±1.1	0.0±0.04	9.1±0.8	11.1±1.0	)
20 – 26	48.9		9.7±0.9	7.4±0.6	23.3±1.1	15.5±1.0	
		(	8.2±0.8	7.4±0.6	22.6±1.1	9.3±0.8	)
26 – 35	43.5		12.3±1.0	11.0±0.9	21.4±1.1	23.1±1.3	
		(	4.4±0.6	7.4±0.7	15.6±1.0	3.1±0.5	)

† The normalization errors due to the uncertainties of the target thickness and the acceptances normalization and the charge collection are estimated to be about 10 %.
‡ Lower limits of the detection energies are 3.1, 4.0, 4.6 and 4.5 MeV for p, d, t and α, respectively.

range between 16 MeV and 35 MeV, because high energy protons above 35 MeV decaying to the ground state of ^{10}Be were not detected due to the small energy losses in the $\mathit{\Delta}E$-SSD. The branching ratios are calculated on the assumption that the decay from the s-hole state is isotropic:

$$Br_i = \frac{\int n_i \; (4\pi/\mathit{\Delta}\Omega_{SSD}) \; dE_x}{\int N \; dE_x}, \qquad i = p, d, t \text{ and } \alpha, \tag{3.16}$$

where N is the number of events of the $^{12}\mathrm{C}(p, 2p)$ reaction, n_i is the number of particles detected for i-decay and E_x is the excitation energy of ^{11}B. The sum of the branching ratios including that of n-decay can exceed 100 % if the decay multiplicity is more than 1. Thus, the n-decay probability can not be estimated unambiguously from the results of the present charged particle decay measurements. The branching ratios of the decay to the low-lying states of the residual nuclei are also calculated. The '2-body decay' region in each decay channel is defined as $E_x(\mathrm{res}) \leq \mathrm{Max}(5$ MeV, $E_{\mathrm{th}}(3\text{-body}))$, where $E_x(\mathrm{res})$ indicates the excitation energy relative to the ground state and $E_{\mathrm{th}}(3\text{-body})$ denotes the threshold energy of particle decay in the residual nucleus. The energy spectra in coincidence with decay particles in the '2-body decay' regions are shown in Fig. 3.13(b). It is clearly seen that the portion of α-decay from the higher excitation energies is much reduced. It should be noted that, for particles with small E_{th}(3-body), the 3-body decay and sequential decay processes are partially included in the '2-body decay' region defined above. Taking the sub-structures around the s-hole state into consideration, we separately evaluated the branching ratios for three excitation energy regions of 16–20, 20–26 and 26–35 MeV in ^{11}B (see Table 3.1).

3.3.3 Charged particle decay of the s-hole state in ^{15}N

The energy spectra of ^{15}N in coincidence with decay charged particles are shown in Fig. 3.15(a). Accidental coincidence events were subtracted. The threshold energies of 2-body decay from ^{15}N to the channels ^{14}C+p, ^{13}C+d, ^{12}C+t, ^{12}B+^{3}He and ^{11}B+α are 10.2, 16.2, 14.8, 28.2 and 11.0 MeV, respectively. The ^{3}He-decay events are also included in the α-decay portion. As seen in Fig. 3.15(a), the α contribution is very small even in the higher excitation region.

The panels (a), (b), (c) and (d) in Fig. 3.16 show four two-dimensional spectra of the energies of p-, d-, t- and α-decay particles versus the excitation energy E_x of ^{15}N. The loci corresponding to the ground states in the residual nuclei are very weak in all spectra, which is totally different from the decay of ^{11}B where the loci of the ground states are very clear. The projection spectra onto the excitation energy axes of the residual daughter nuclei are shown in Fig. 3.16(e), (f), (g) and (h). The peaks due to binary decay processes are populating low-lying excited states up to about 3-body decay threshold energy in each nucleus, except for α-decay.

The experimental differential cross sections and the branching ratios of decay particles are listed in Table 3.2. The branching ratios are calculated using Eq. (3.16). The excitation energy region is restricted to the range between 16 MeV and 40 MeV. Although high energy protons above 35 MeV decaying to the ground state of ^{14}C were excluded due to the small energy losses in the ΔE-SSD, it is not expected from Fig. 3.16(a) that there exist significant decay events on the ground state locus at higher energies. The branching ratios of the decay to the low-lying states of the residual nuclei are calculated similarly in the case of ^{11}B. The '2-body decay' region in each decay channel is defined as $E_x(\mathrm{res}) \leq \mathrm{Max}(8\ \mathrm{MeV},\ E_{\mathrm{th}}(\text{3-body}))$. The 3-body decay and sequential decay processes are almost excluded in the '2-body decay' region, except for d-decay with the 3-body decay threshold energy of 5.0 MeV. The results of neutron decay described in the next section are also included in Table 3.2.

The energy spectra in coincidence with decay particles in the '2-body decay' regions are shown in Fig. 3.15(b). The portion of t-decay from the higher excitation energies seems to be relatively enhanced. We separately evaluated the branching ratios for three excitation energy regions of 16–20, 20–30 and 30–40 MeV in ^{15}N (see Table 3.2). In the first region, however, d- and t-decays could not be measured due to the lower limits of the detectable energies.

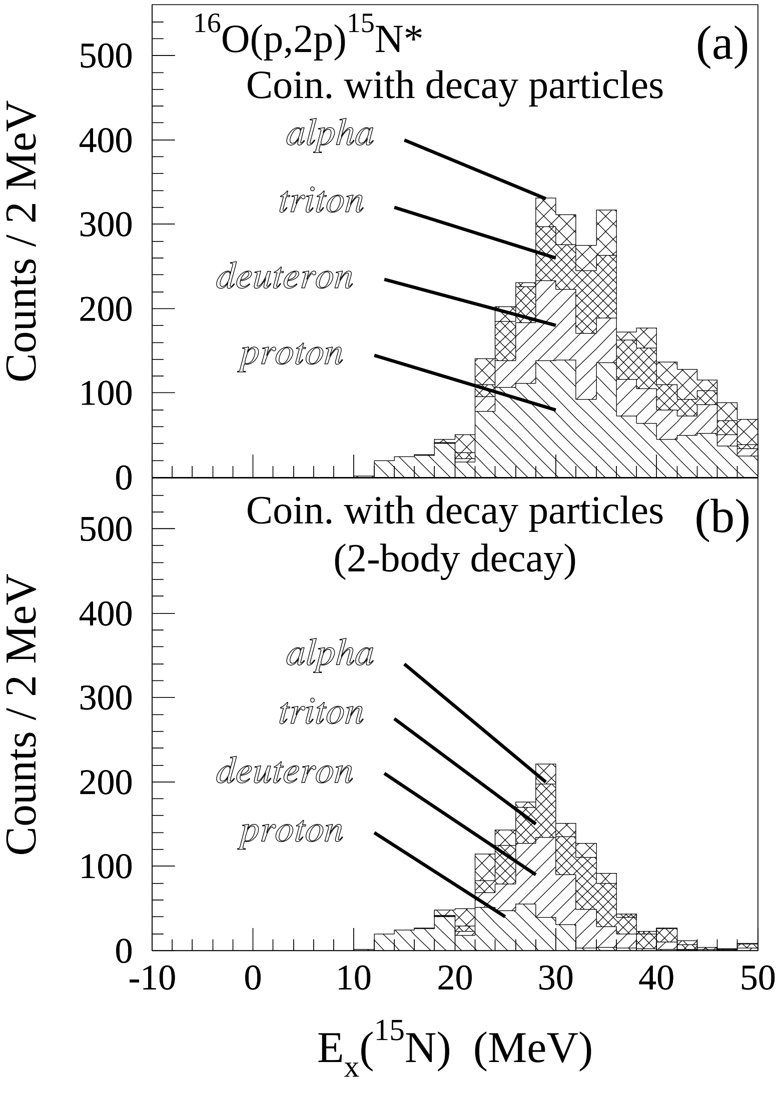

Figure 3.15: (a) Excitation energy spectra of ^{15}N in coincidence with decay charged particles. The contributions of the *p*-, *d*-, *t*- and α-decays are separately shown. (b) The same figure as (a), but for the decay onto the '2-body decay' regions (see text).

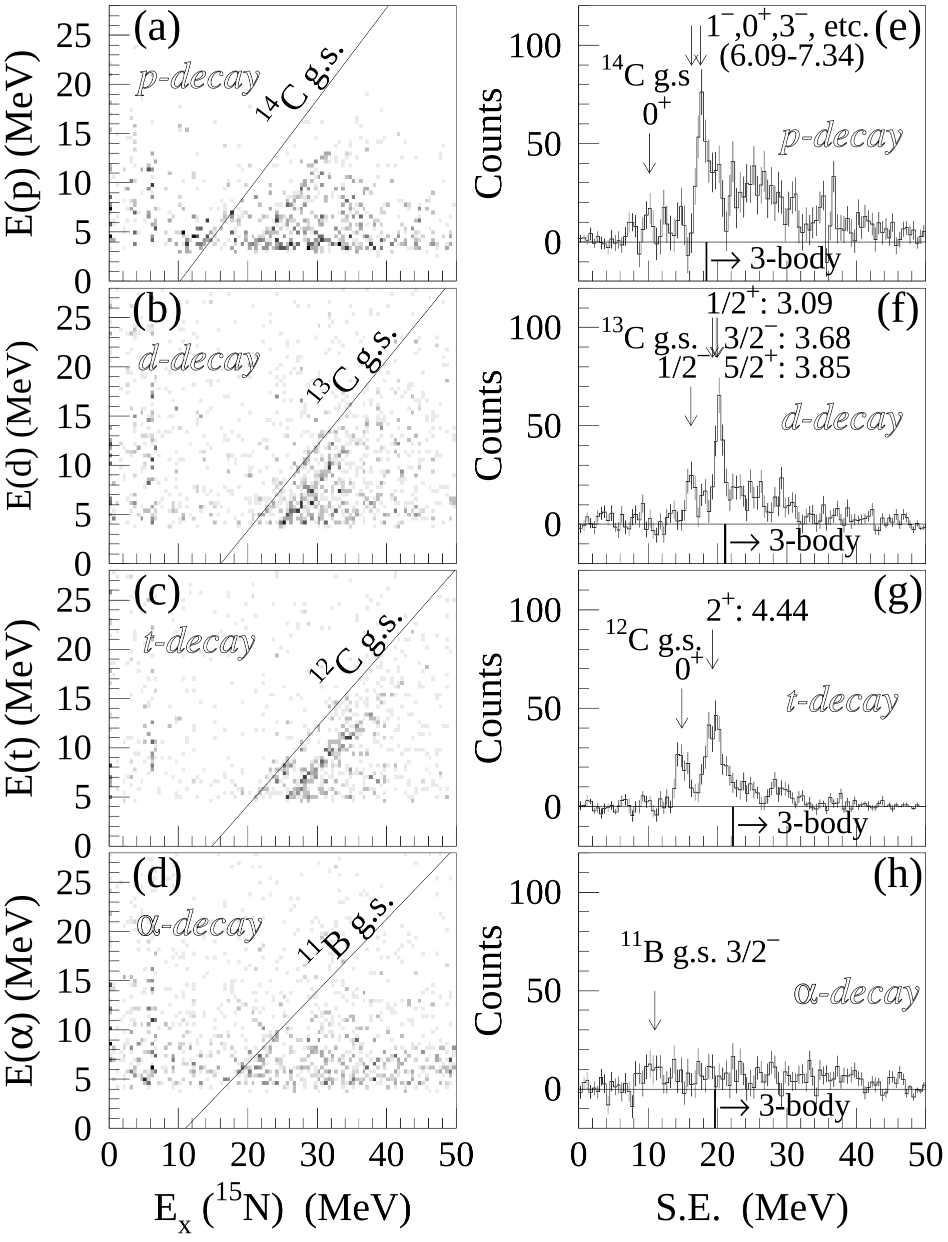

Figure 3.16: The left side panels show two-dimensional plots of the energies of the decay particles versus the excitation energy E_x of ^{15}N for (a) p-, (b) d-, (c) t- and (d) α-decay channels. The locus lines for the ground states in the corresponding residual nuclei are shown. The right side panels display separation energy spectra for the final states of (e) ^{14}C, (f) ^{13}C, (g) ^{12}C and (h) ^{11}B obtained from projecting events in panels (a), (b), (c) and (d) onto the excitation energy axes of the residual nuclei, respectively. The threshold energies of the 3-body decay channels are indicated.

Table 3.2: Measured differential cross sections of the s-hole state in ^{15}N and the branching ratios of decay particles are listed. Only statistical errors are shown. The branching ratios of the decay onto the '2-body decay' regions are given in parentheses (for further details see text).

$E_x(^{15}\mathrm{N})$ (MeV)	$d^3\sigma/d\Omega_1 d\Omega_2 dE^\dagger$ (μb/sr^2 MeV)		Branching ratio (%) ‡					
			n	p	d	t	α	
16 – 40	148.1		48.4±2.9	16.7±1.1	8.4±0.5	7.6±0.4	4.3±0.6	
		(	22.1±2.0	5.1±0.7	6.1±0.4	6.1±0.4	2.4±0.5	)
16 – 20	19.0		39.1±6.7	8.7±3.0	0.0±0.1	0.0±0.1	0.6±1.2	
		(	39.1±6.7	8.7±3.0	0.0±0.1	0.0±0.1	0.6±1.2	)
20 – 30	67.4		37.8±3.9	16.0±1.5	7.8±0.7	6.1±0.6	3.8±0.8	
		(	24.2±3.1	7.5±1.1	7.8±0.7	6.1±0.6	3.6±0.8	)
30 – 40	61.7		62.5±4.9	19.9±1.7	11.8±1.0	11.7±0.8	6.1±1.1	
		(	14.9±2.7	1.4±0.5	6.1±0.7	8.0±0.7	1.5±0.6	)

† The normalization errors due to the uncertainties of the target thickness and the acceptances normalization and the charge collection are estimated to be about 15 %.
‡ Lower limits of the detection energies are 3.2, 3.1, 4.0, 4.6 and 4.5 MeV for n, p, d, t and α, respectively.

3.4 Neutron decay

3.4.1 Efficiency of neutron detectors

In the second beam time, neutron decay of the s-hole state in ^{15}N produced via the $^{16}\mathrm{O}(p, 2p)$ reaction was measured with the thirty BC-501A liquid scintillators. The neutron energy E_n is determined by means of the time-of-flight (TOF) method as follows:

$$E_n = m_n c^2 \left[\frac{1}{\sqrt{1 - (L_{\mathrm{TOF}}/t_n c)^2}} - 1 \right], \tag{3.17}$$

where m_n is the neutron mass, c is the light speed, L_{TOF} is length from the target to the neutron detector, and t_n is the flight time of a neutron. t_n is given by the information on the time difference δt between the neutron and γ-rays as $t_n{=}t_\gamma{+}\delta t$, where t_γ is the flight time of γ-rays ($t_\gamma{=}L_{\mathrm{TOF}}/c$). δt is obtained from the TDC spectrum. All channels of the TDC's for the neutron detectors were calibrated with a time calibrator module. The linearities of the TDC812F's were slightly bad and the time-to-channel relations were fitted with third-order polynomials.

The efficiency and the n-γ separation of the neutron detector are dependent on E_n. We did not intend to detect neutrons with very low energies less than 2 MeV because, in the charged particle decay measurements, the lower limits of the detection energy were more than 3 MeV even for protons. The efficiency is strongly dependent on the threshold of the neutron detector. The gain of the fast-gated ADC of each detector was adjusted in advance, using a Compton edge of the 662 keV γ-ray of ^{137}Cs, and the hardware threshold was set at the electron equivalent energy of $\sim$200 keVee. The precise value of the threshold was determined by using the several background γ-rays and 4.44 MeV γ-ray obtained from the $^{12}\mathrm{C}(p,p')^{12}\mathrm{C}^*(2^+)$ inelastic scattering, which were measured several times during the experiment. The gain shifts of the neutron detectors in the experiment were negligible. ADC spectra for the 0.662 MeV γ-ray of ^{137}Cs, the background γ-rays (0.835 MeV of ^{54}Mn, 1.46 MeV of ^{40}K, 2.75 MeV of ^{24}Na), and the 4.44 MeV γ-ray from the $^{12}\mathrm{C}^*(2^+)$ state are shown in Fig. 3.17(a), (b), and (c), respectively, where the corresponding Compton edges are 0.477 MeV, 0.639 MeV, 1.24 MeV, 2.52 MeV, and 4.20 MeV. ^{24}Na was produced by the neutron capture reaction of ^{23}Na in the NaI(Tl) detectors.

There is a problem in the determination of the position of the Compton edge in the measured spectrum, which might increase systematic errors. We followed the prescription of Dietze and Klein [79] who gave the dependence of the Compton edge position on the energy resolution of the detector. The relation of the ADC channels with the Compton edge energies of γ-rays is shown in Fig. 3.17(d) with a straight line obtained from a least square fitting, where the energy shift of the 4.44 MeV γ-ray due to the Doppler effects was corrected. From this relation, the threshold used in the experiment was estimated as 220 keVee, since the light output for electrons is almost linear for energies $E_e \geq 40$ keV [80].

The efficiency is calculated using a computer code SCINFUL [81], where the neutron interactions within the detector are simulated with Monte-Carlo techniques. The calculated efficiency curves of the present neutron detector are shown in Fig. 3.18 for the three threshold energies, where the NE213 liquid scintillator is substituted for the BC-501A. The efficiencies of two neutron detectors were checked after the neutron decay measurements by using the low energy $d+d \longrightarrow {}^3\mathrm{He}+n$ reaction (see Appendix A).

3.4.2 n-γ separation

Most of γ-rays entering a neutron detector from the target are concentrated on a peak in the TDC spectrum corresponding to the time t_γ, which is called γ-flash. Some of γ-rays, however, come after the γ-flash due to the finite life time of the excited state. Moreover, there may be a lot of γ-rays from other materials besides the target such as the Faraday cup and the beam pipes. The pulse shape discrimination in the neutron detector is, therefore, essential to separate neutrons from γ-rays in the

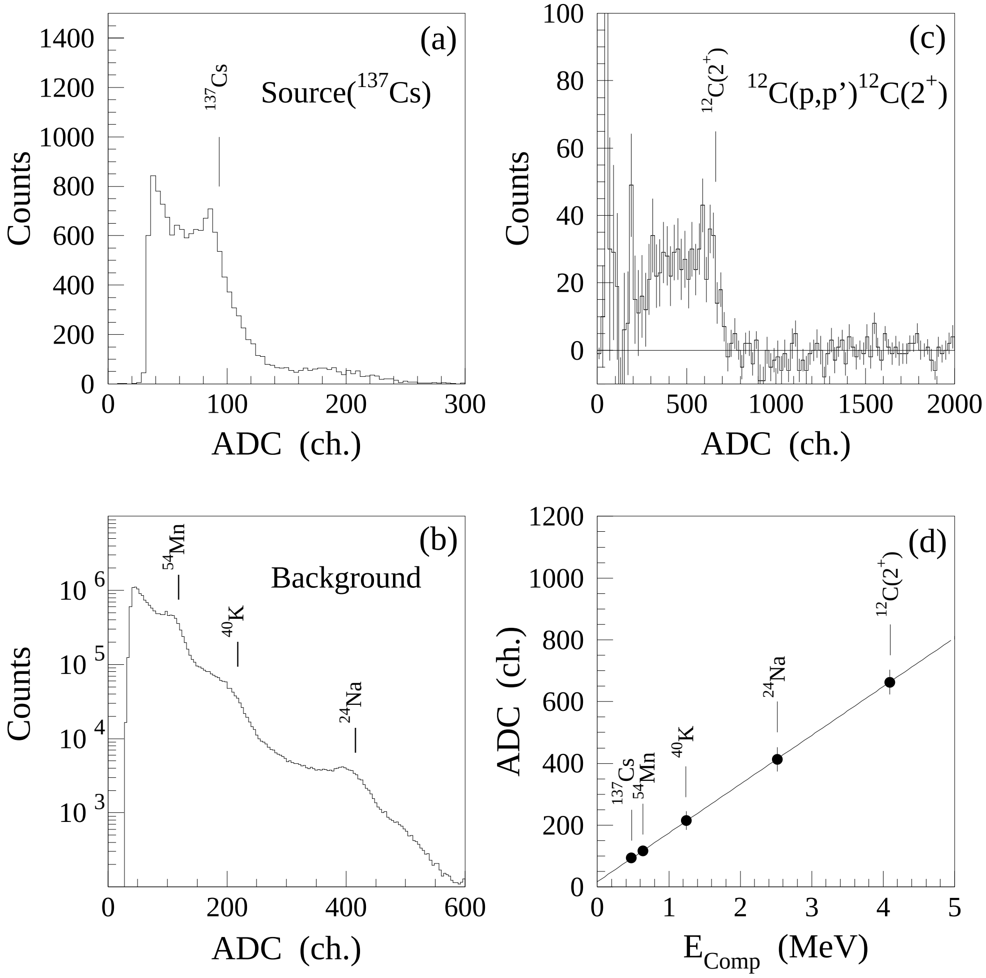

Figure 3.17: Energy calibration for the fast-gated ADC signals of liquid scintillators by several Compton edges of γ-rays. (a) ADC spectrum for 0.662 MeV γ-rays of ^{137}Cs source. (b) ADC spectrum for the background γ-rays during the beam-off time in the experiment. The γ-rays of ^{24}Na produced by the neutron capture reaction of ^{23}Na in NaI(Tl) detectors are seen with the γ-rays of ^{54}Mn and ^{40}K. (c) ADC spectrum for a γ-ray coincidence measurement of ^{12}C$(p,p')^{12}$C(2$^+$:4.44 MeV). Accidental coincidence events are subtracted and all available ADC spectra are added in this spectrum. (d) Relation of the ADC channels with the Compton edge energies of γ-rays. The energy shift due to the Doppler effect is corrected for the γ-ray from the ^{12}C(2$^+$) state. Five points are fitted well with a linear function.

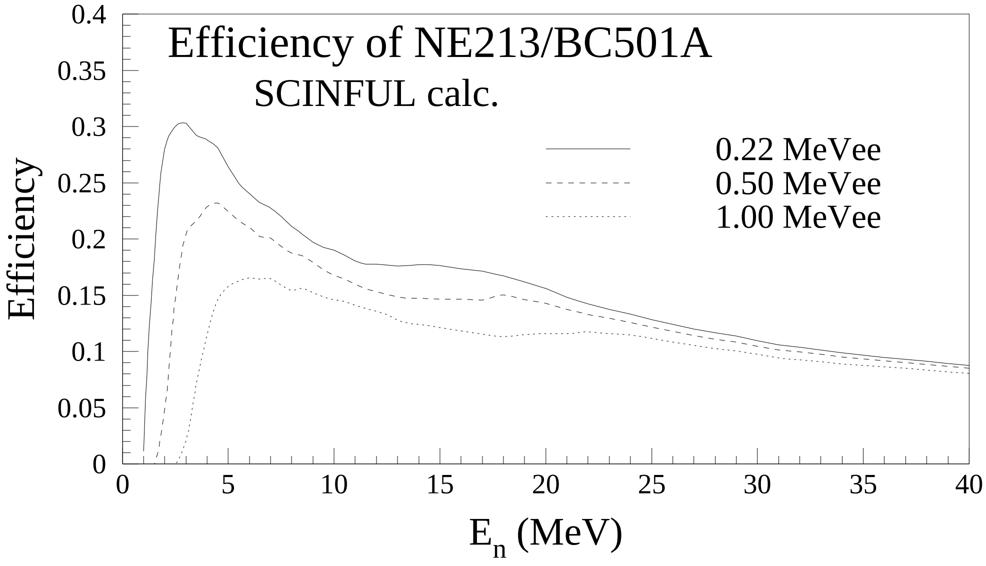

Figure 3.18: Neutron detection efficiencies calculated with the code SCINFUL for three threshold energies. The electron-equivalent energy of the detection threshold in the present experiment is 220 keVee.

present measurements.

A typical two-dimensional spectrum of the slow-gated ADC versus the fast-gated ADC is shown in Fig. 3.19(a). Two loci corresponding to neutron events and γ events are clearly seen with a good separation. A proper projection of the two-dimensional spectrum is displayed in Fig. 3.19(b), where the projection function is determined to connect the center points of two loci at several ADC channels. For the whole light-output energies above the present threshold of 220 keV, neutrons are unambiguously selected. Since two of the neutron detectors did not show the good n-γ separation properties due to the problem of the electronics, we used twenty-eight neutron detectors in the analysis.

A summed TDC spectrum for 15 neutron detectors with a gate of γ-ray events is shown in Fig. 3.20(a) and (b). (Fig. 3.20(b) is the expanded spectrum around the γ-flash region.) A prompt peak and an accidental peak of γ-flashes are displayed with the interval of 178 nsec. The time resolution of 0.8 nsec is obtained from the γ-flash peak, in which about 0.5 nsec is the resolution of the beam itself and the other is due to the resolution of the detector system. The time resolution for the neutron detection is determined by the above intrinsic resolution and the ratio of the detector thickness to the flight path. In the present experiment, the latter ($\delta L/L$=5/200=0.025) is dominant. The energy resolution is dependent on the neutron energy. For example,

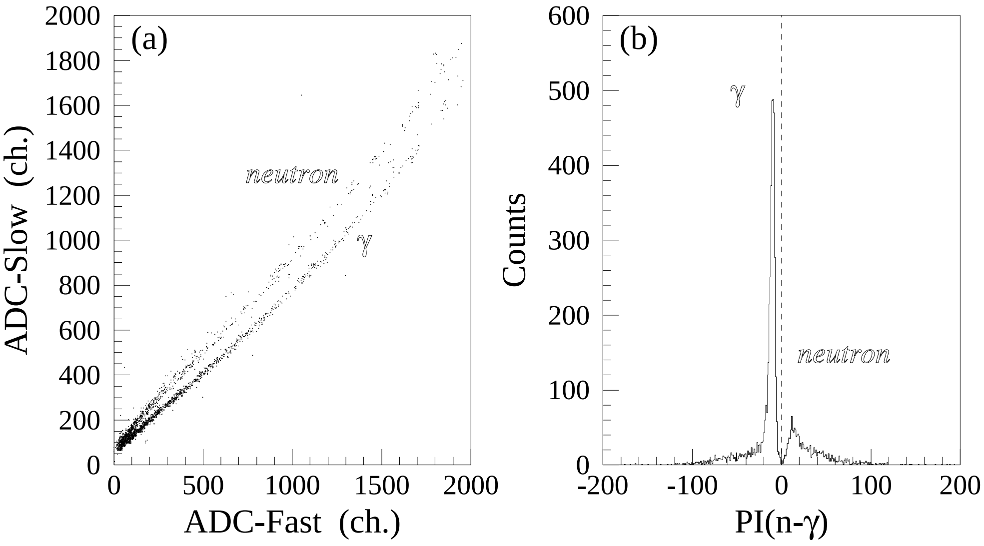

Figure 3.19: Pulse-shape discrimination (PSD) spectra of a BC-501A neutron detector. (a) Two-dimensional plot of the slow-gated ADC versus the fast-gated ADC. (b) Neutron-γ separation spectrum obtained from the proper projection of the spectrum (a).

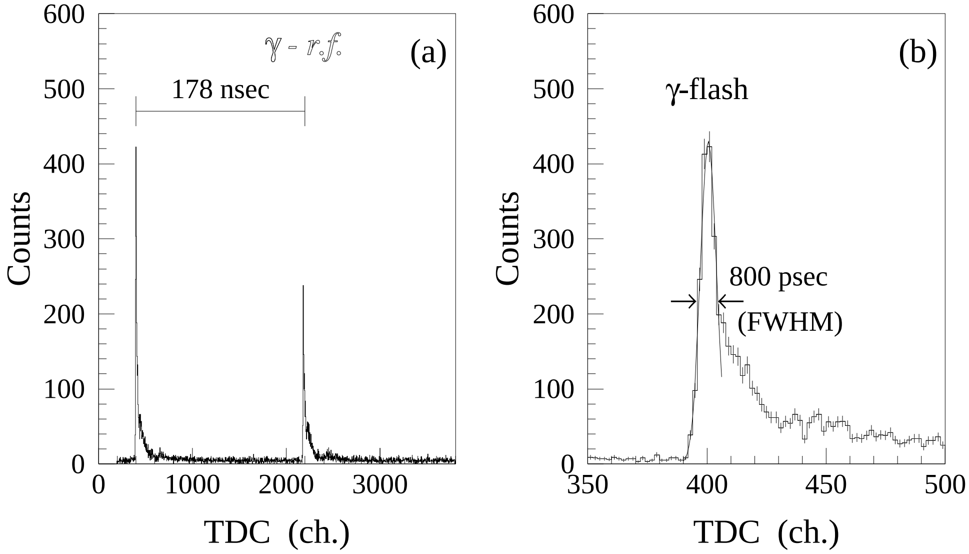

Figure 3.20: (a) TDC spectrum of a BC-501A neutron detector for γ-rays. The interval between the beam bunches is 178 nsec. (b) Expanded spectrum of (a) around the γ-flash region. The time resolution is typically 0.8 nsec (FWHM).

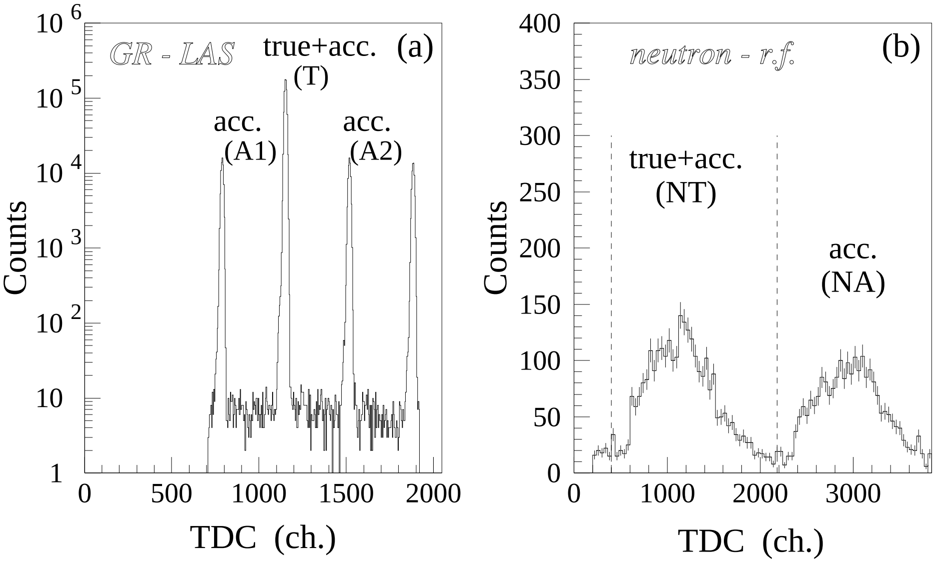

Figure 3.21: (a) TDC spectrum for the time difference between the GR and LAS trigger signals in a measurement of the $H_2O(p,2p)$ reaction. (b) TDC spectrum of a BC-501A detector for neutrons. Random coincidence events are subtracted using the prompt regions and accidental regions in both spectra (see text).

δE_n is 600 keV for E_n=10 MeV, and 1.4 MeV for E_n=20 MeV.

3.4.3 Subtraction of the accidental coincidence events

In the neutron decay measurements, since the ratio of the accidental to the true coincidence in the $(p,2p)$ reaction with the H_2O target was about 10 %, it should not be neglected in the subtraction process of the accidental events of neutron decay. A TDC spectrum for the time difference between the trigger signals of GR and LAS is shown in Fig. 3.21(a). A prompt peak includes both the true and accidental coincidence of GR and LAS, while other peaks only include the accidental coincidence events. Here, we labeled the prompt peak as (T) and the accidental peak on the both sides of (T) as (A1) and (A2). The spectrum for the $^{16}O(p,2p)^{15}N$ reaction is simply obtained from the gate condition of (T)-((A1)+(A2))/2. Fig. 3.21(b) shows a summed TDC spectrum of 15 neutron detectors with a gate of neutron events. Using the γ-flash channels in Fig. 3.20(a), we can determine the prompt region (labeled as (NT)) and the accidental region (labeled as (NA)). (NT) includes both the true triple coincidence events and the accidental coincidence events. The ratio of the true to the accidental coincidence is not so good. The accidental coincidence events in the prompt region were divided into some categories: only the event of the neutron detector is accidental [N$_{Ac}$], only the LAS event is accidental [L$_{Ac}$], only the GR event is accidental [G$_{Ac}$], and the all three events are random [3$_{Ac}$]. Some gate conditions are defined using the combinations of (T), (A1), or (A2) in Fig. 3.21(a) and (NT) or (NA) in Fig. 3.21(b) as follows:

[**1**] (T)$\otimes$(NT) includes [3$_{Tr}$]+[N$_{Ac}$]+[L$_{Ac}$]+[G$_{Ac}$]+[3$_{Ac}$],

[**2**] (T)$\otimes$(NA) includes [N$_{Ac}$]+[3$_{Ac}$],

[**3**] (A2)$\otimes$(NT) includes [L$_{Ac}$]+[3$_{Ac}$],

[**4**] (A2)$\otimes$(NA) includes [G$_{Ac}$]+[3$_{Ac}$],

[**5**] (A1)$\otimes$(NT) includes [L$_{Ac}$]+[3$_{Ac}$],

[**6**] (A1)$\otimes$(NA) includes only [3$_{Ac}$],

where [3$_{Tr}$] denotes the true triple coincidence. Thus, the accidental coincidence events are subtracted with following relation,

$$[3_{Tr}] = [\mathbf{1}] - [\mathbf{2}] - \frac{[\mathbf{3}] + [\mathbf{5}]}{2} - [\mathbf{4}] + 2 \times [\mathbf{6}]. \tag{3.18}$$

3.4.4 Neutron decay of the *s*-hole state in ^{15}N

An excitation energy spectrum of ^{15}N of the ^{16}O$(p, 2p)^{15}$N* reaction for the H_2O ice target is shown in Fig. 3.22(a). The energy resolution of 700 keV (FWHM) is worse compared to Fig. 3.8(b) mainly due to the energy losses in the thick ice target. Taking into account this difference of the resolution, the spectrum for the H_2O ice target agrees well with that obtained from the SiO_2 target after subtracting the Si contribution. This ensures the correctness of the subtraction process in the previous data.

The energy spectrum of ^{15}N in coincidence with decay neutrons is shown in Fig. 3.22(b). Accidental coincidence events were subtracted using Eq. (3.18). The threshold energy of 2-body decay from ^{15}N to the ^{14}N+n channel is 10.8 MeV. Fig. 3.22(d) shows a two-dimensional spectrum of the energy of decay neutrons versus the excitation energy E_x of ^{15}N and the projection spectrum onto the excitation energy axis of the ^{14}N is shown in Fig. 3.22(e). The peaks due to binary decay processes are populating low-lying excited states up to about 3-body decay threshold energy. The energy resolution of the ground state peak of ^{14}N is 2 MeV (FWHM). Since the tail of the peak just below the 3-body decay threshold goes above the 3-body decay threshold energy due to the energy resolution, the '2-body decay' region in the neutron decay channel is defined as $E_x(\mathrm{res}) \leq 8.2$ MeV. The energy spectra in coincidence with decay neutrons in the '2-body decay' region is shown in Fig. 3.22(c).

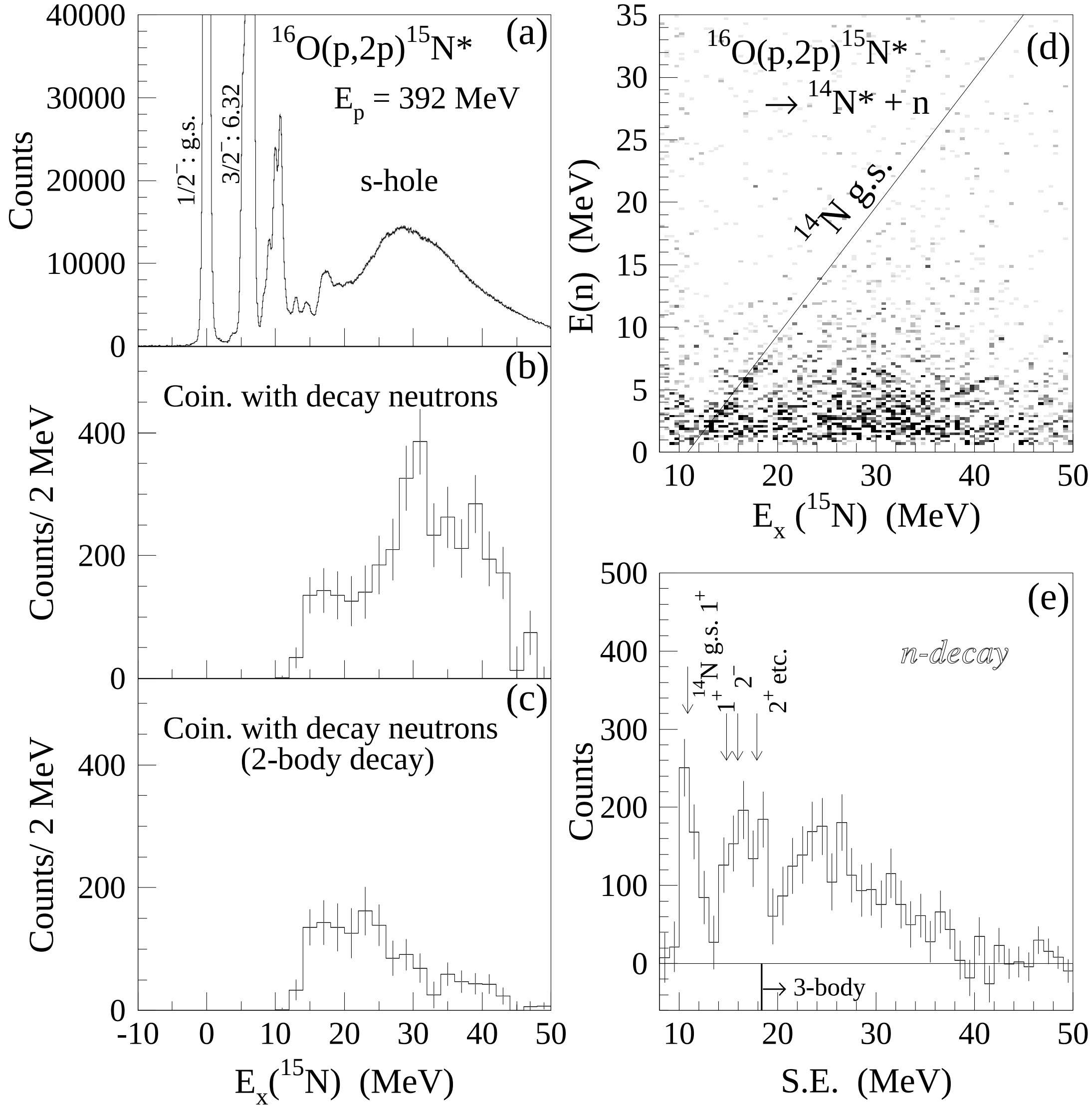

Figure 3.22: (a) Energy spectrum of ^{15}N of the ^{16}O$(p, 2p)^{15}$N* reaction for the H_2O ice target. (b) Excitation energy spectrum of ^{15}N in coincidence with decay neutrons after subtraction of random coincidences. (c) The same as (b), except for the decay onto the 'two-body decay' region (see text). (d) Two-dimensional plot of the energy of decay neutrons versus the excitation energy of ^{15}N. A locus line for the ground state in ^{14}N is shown. (e) Separation energy spectrum obtained from projecting panel (d) onto the final states of ^{14}N. The threshold energy of the 3-body decay channel is indicated.

Table 3.3: Transmission probabilities of the neutron flux for the wall (4 mm stainless steel) of the scattering chamber. Three probabilities are calculated with the code MCNP [82]: the flux without collisions in the wall, the flux in which the loss of the energy is only below 0.5 MeV, and the flux with the energy above 3.2 MeV.

E_n (MeV)	flux-1 (no collision)	flux-2 ($\geq E_n - 0.5$ MeV)	flux-3 ($\geq$3.2 MeV)
3.5	0.886	0.963	0.962
5.0	0.882	0.953	0.962
10.0	0.898	0.952	0.972
15.0	0.917	0.953	0.974
20.0	0.926	0.954	0.981

It is clearly seen that the portion of n-decay from the higher excitation energies ($E_x \geq$ 25 MeV) of ^{15}N is much reduced. It should be noted that the energy dependence of the efficiency has not yet been corrected for the all decay spectra in Fig. 3.22.

Here, we evaluate the neutron yield with the energy above 3.2 MeV in the calculation of the branching ratio. This lower limit is the same as the detection limit of the proton if the mean energy loss of protons in the target is considered. The yields of the decay neutrons are firstly corrected for the detection efficiencies with the SCINFUL calculation (see Fig. 3.18), and secondly the absorptions in the wall of the scattering chamber are taken into account. The absorption effects are estimated by using the Monte-Carlo Code for Neutron and Photon Transport (MCNP) [82]. The results of the simulation at several energies are shown in Table 3.3, where each value of the transmission probability denotes the ratio of the neutron flux emerging out of the wall to the source flux with the neutron energy E_n. Three flux ratios are calculated: the flux without collisions in the wall, the flux in which the loss of the energy is only below 0.5 MeV, and the flux with the energy above 3.2 MeV. The energy dependence of the absorption of the flux is not so large. In the analysis, we adopted the second flux ratio because the 0.5 MeV is nearly the typical experimental energy resolution. Thus, the efficiency-corrected yields are divided by 0.95. The uncertainties of this correction are smaller than the statistical errors.

After the correction for the detection efficiency and the absorption, the branching ratio of n-decay is calculated on the assumption that the decay from the s-hole state is isotropic, similarly for the charged particle decay. The branching ratio of n-decay of the s-hole state is also listed in Table 3.2, which is the largest among the all particle decay processes as expected from the property of the no-Coulomb barrier.

Chapter 4

Discussion

4.1 Low excitation spectra of ^{11}B and ^{15}N

One of the problems to study knockout reactions for deeply bound nucleons is how much other processes such as the multi-step scattering and the correlated reactions (e.g., $(p, 3p)$ and $(p, 2pn)$) than the direct quasifree knockout process contribute the final excitation spectra. Before discussing the s-hole states in ^{11}B and ^{15}N, we first briefly study which low-lying states are strongly excited. This teaches us to what extent the results of the present $(p, 2p)$ measurements are explained as the direct proton knockout process.

4.1.1 Low-lying states in ^{11}B

An energy spectrum below the excitation energy of 11 MeV for the $^{12}\mathrm{C}(p, 2p)^{11}\mathrm{B}^*$ reaction is shown in Fig. 4.1 with peak-fitting results. All peaks are well fitted with the Gaussian+tail functions. The J^π assignments used below are according to Ref. [87]. Three states corresponding to l=1 knockout, *i.e.* $0(\frac{3}{2}^-)$, $2.125(\frac{1}{2}^-)$, and $5.02(\frac{3}{2}^-)$ MeV are clearly visible. The strength at 4.445 MeV where $\frac{5}{2}^-$ state is located is absent, suggesting that the two-step process like 1p-knockout plus inelastic excitation appears to be negligible. The $\frac{7}{2}^-$ state at 6.74 MeV and the $\frac{1}{2}^+$ state at 6.79 MeV can not be separated due to the energy resolution of 450 keV. If the excitation mechanism of the 6.74 MeV is the same as that of the $\frac{5}{2}^-$ state, the forth peak may be dominantly $\frac{1}{2}^+$ as concluded by the analysis of the $(e, e'p)$ reaction [88]. In the peak-fitting procedure, small contributions at 7.29 MeV ($\frac{5}{2}^+$) and 8.56 MeV ($\frac{3}{2}^-$) are observed. The 9.88 MeV ($\frac{3}{2}^+$) peak is slightly broader (630 keV FWHM) than other peaks, which implies the doublet of two states or may be due to the high excitation energy above the particle decay threshold of the ^{7}Li+α channel.

Although the ground state of ^{12}C has the $(s_{1/2})^4(p_{3/2})^8$ configuration in the simple independent particle shell model (IPSM), nucleon-nucleon correlations cause a smear-

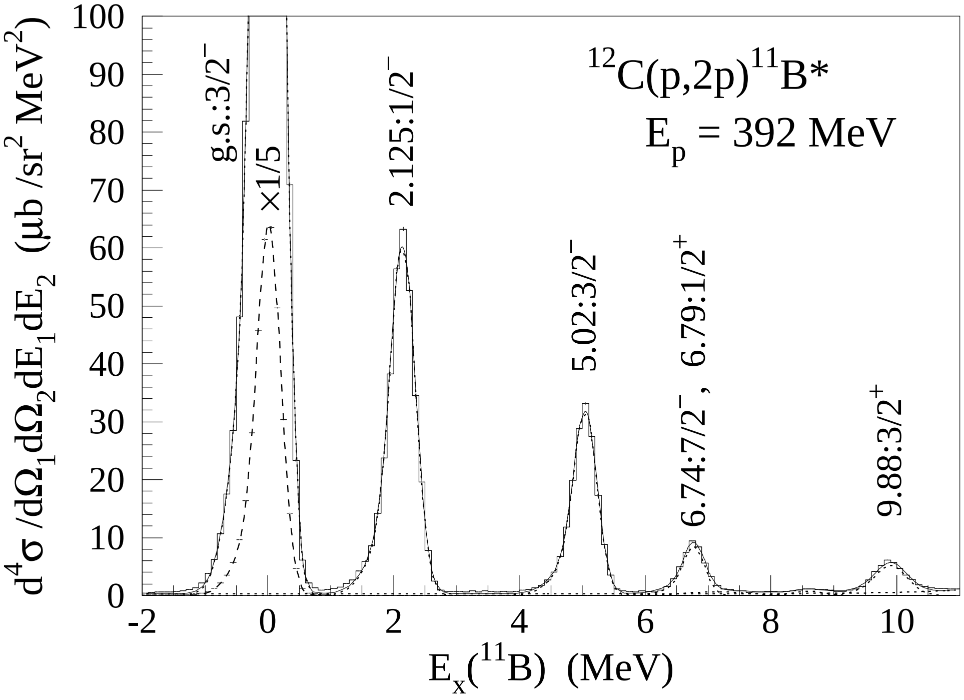

Figure 4.1: Energy spectrum of the low-lying states in ^{11}B obtained from the ^{12}C($p, 2p$) reaction. All peaks are well fitted with the same Gaussian+tail functions.

ing of the Fermi surface. Thus, the 2.125 MeV ($\frac{1}{2}^-$) state should not be regarded as the 1p-2h excitation but the direct knockout of the proton in the $p_{1/2}$ state. The 6.79 MeV ($\frac{1}{2}^+$) state is also considered to be the knockout of the $2s_{1/2}$ proton. The cross section ratio of the three p-hole states is similar to the result of the high resolution $(e,e'p)$ experiments [20]. The spectroscopic factors (C^2S) derived from the DWIA analysis for the present data are larger than those extracted from the $(e,e'p)$ but smaller than those of the $(d,^3\mathrm{He})$ reactions [89]. (For example, $C^2S(\mathrm{g.s}) = 2.45$ (for the present $(p,2p)$), 1.72 (for the $(e,e'p)$), and 2.98 (for the $(d,^3\mathrm{He})$).) However, the obtained values from the DWIA calculations have a large dependence on the choice of parameters. (Details for the DWIA calculations will be described in the next section.) Since the kinematical condition is optimized for exciting the s-hole states in the present $(p,2p)$ measurements, the absolute cross sections of the p-hole states and other states are not suitable to be discussed in detail. In fact, the cross sections of the p-hole states have large acceptance dependence and are varied by more than factor 2 with the different cuts of the spectrometer acceptances.

4.1.2 Low-lying states in ^{15}N

Fig. 4.2 shows an energy spectrum of the excitation energy from 4.5 MeV to 14 MeV for the $^{16}\mathrm{O}(p,2p)^{15}\mathrm{N}^*$ reaction. All peaks are well fitted with the Gaussian+tail functions determined by the peak shape of the ground state (g.s.), which is omitted in Fig. 4.2. The two p-hole states, *i.e.* 0.0 ($\frac{1}{2}^-$) and 6.32 ($\frac{3}{2}^-$) MeV, are dominantly excited. The cross section of the $\frac{1}{2}^-$ g.s. is 90 % of the 6.32 MeV state. The J^π assignments used below are according to Ref. [90]. The $\frac{5}{2}^+$ state at 5.27 MeV and the $\frac{1}{2}^+$ state at 5.30 MeV are not separated due to the energy resolution. Although the ground state of ^{16}O has the $(s)^4(p)^{12}$ configuration in the simple IPSM, there exit some occupation probabilities for the next sd-shells due to the ground state correlations. Thus, both the $\frac{5}{2}^+$ and $\frac{1}{2}^+$ states are considered to be the direct knockout of the proton in the $1d_{5/2}$ and $2s_{1/2}$ states.

In the peak-fitting procedure, the 7.16 MeV ($\frac{5}{2}^+$) and 7.30 MeV ($\frac{3}{2}^+$) states are included but the contributions are very small. Despite of the existence of many states in the excitation energy above 8 MeV, only seven peaks and a smooth background above the particle decay threshold are enough to obtain a small χ^2 values in the fitting. The extracted peak energies are consistent with three $\frac{1}{2}^+$ states (8.31, 9.05, and 11.44 MeV) and four $\frac{3}{2}^-$ states (9.93, 10.70, 12.15, and 12.92 MeV). The cross section ratio of four p-hole states (0.0, 6.32, 9.93, and 10.70 MeV) is similar to the results of the high resolution $(e,e'p)$ experiments [21]. The 8.31 and 9.05 MeV $\frac{1}{2}^+$ states are enhanced compared to the Fig. 1 in Ref. [21], maybe due to the different recoil momentum condition. According to the DWIA analysis for the $(e,e'p)$ spectral

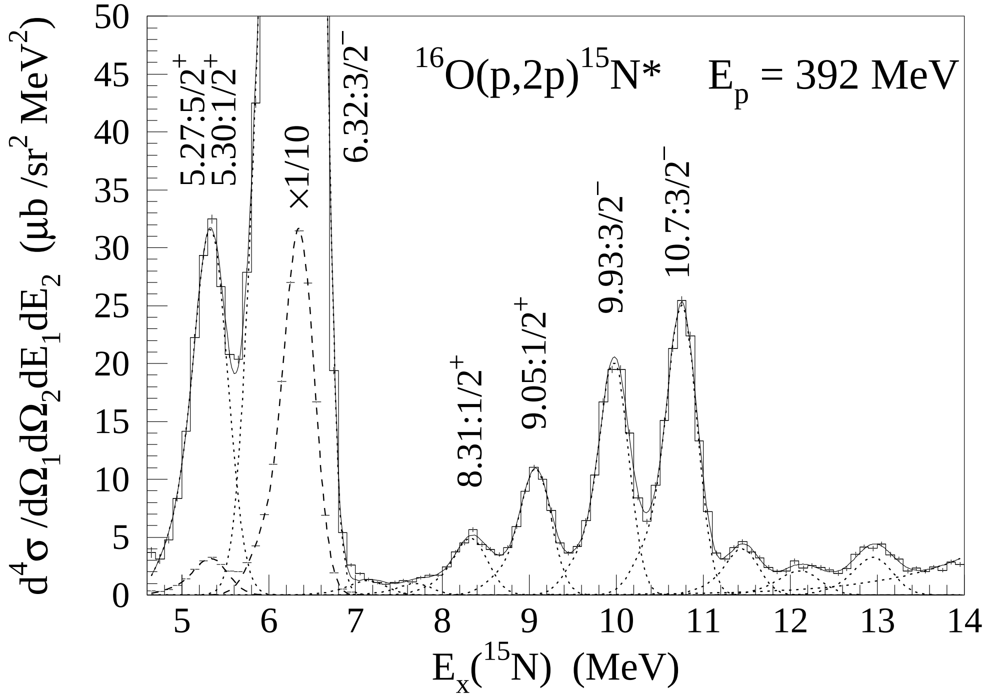

Figure 4.2: Energy spectrum of the low-lying states in ^{15}N obtained from the ^{16}O$(p, 2p)$ reaction in the first measurement. All peaks are fitted with the same Gaussian+tail functions determined by the peak of the ground state.

functions, both the 8.31 and 9.05 MeV states were concluded to be dominantly $1s$-hole states with small $2s$ contributions.

The spectroscopic factors derived from the DWIA analysis for the present data are larger than those extracted from the $(e, e'p)$ but smaller than those of the $(d,{}^3\mathrm{He})$ reactions [92, 91] similarly to the case of $^{11}\mathrm{B}$. They are also inconsistent with the results obtained from other $(p, 2p)$ reaction [18, 93] in which the values are small even compared to the $(e, e'p)$ reaction. (For example, $C^2S(\mathrm{g.s}) = 1.77$ (for the present $(p, 2p)$), 1.17 (for the $(e, e'p)$), 2.14 (for the $(d,{}^3\mathrm{He})$), and 1.05 (for other $(p, 2p)$).)

4.2 Excitation spectra around the s-hole states

4.2.1 Recoil momentum dependence

As discussed in the previous section, all visible states at low excitation energies in $^{11}\mathrm{B}$ and $^{15}\mathrm{N}$ produced via the present $(p, 2p)$ reactions are regarded as one-hole states except for the 9.88 MeV $\frac{3}{2}^{+}$ state in $^{11}\mathrm{B}$. This strongly supports that the direct knockout process is dominant in the reaction mechanism. However, at the energy above particle decay threshold, the excitation spectra include four-body final states in addition to possible multi-step scattering. In order to estimate these background processes, we compare the recoil momentum dependence of the experimental differential cross sections around s-hole states with DWIA calculations.

DWIA calculations

For the quasifree knockout reaction, usually a so-called 'factorization' approximation is introduced so that the projectile-struck particle elastic scattering cross section enters as a multiplicative factor. Here, we used the program code THREEDEE [83] for DWIA calculations, which explicitly includes spin-orbit distortion effects. Thus, the calculations utilize factorization of the NN amplitude, not the cross section, into DWIA and fully spin-dependent two-body terms.

When considering a quasifree reaction $A(a, cd)B$ where $A{=}B{+}b$, the cross section can be written as [83]

$$\frac{d^3\sigma}{d\Omega_c d\Omega_d dE} = \frac{2\pi}{\hbar v}\omega_B C^2 S \\ \times \sum_{\substack{\rho_a \rho'_c \rho''_d \\ JM}} \frac{\left| \sum_{\substack{\sigma_a \sigma'_c \sigma''_d \\ \Lambda\sigma_b}} (2L+1)^{\frac{1}{2}} (L\Lambda S_b \sigma_b | JM)\; T^{L\Lambda}_{\substack{\sigma_a \sigma'_c \sigma''_d \\ \rho_a \rho'_c \rho''_d}}\; \langle \sigma'_c \sigma''_d |\; t \;| \sigma_a \sigma_b \rangle \right|^2}{(2J+1)(2S_a+1)}, \qquad (4.1)$$

where S_a=S_b=$\frac{1}{2}$ are the spins of particles a and b, v is the incident velocity, ω_B is the phase space factor, and C^2S is the spectroscopic factor. J, M are the total angular momentum quantum numbers of particle b. The quantities L and Λ are, respectively, the orbital angular momentum carried by b and its projection. The two-body transition operator t is separated outside the distorted wave integral by the factorization approximation. The spin matrices are given in the different coordinates where the directions of propagation of particles a, c, and d are $\hat{z}$, $\hat{z}'$, and $\hat{z}''$ axes. Spin projections are denoted as ρ_i. The quantity $T^{L\Lambda}$ is defined by

$$T^{L\Lambda}_{\substack{\sigma_a\sigma'_c\sigma''_d \\ \rho_a\rho'_c\rho''_d}} = (2L+1)^{-\frac{1}{2}} \int \chi^{(-)}_{\sigma'_c\rho'_c}{}^{*}(\vec{r}\,')\chi^{(-)}_{\sigma''_d\rho''_d}{}^{*}(\vec{r}\,'')\ \phi_{L\Lambda}(\vec{r}\,)\ \chi^{(+)}_{\sigma_a\rho_a}(\gamma\vec{r}\,)\ d\vec{r}, \tag{4.2}$$

where γ=B/A, the $\chi^{(\pm)}$ are distorted waves which also convert the spin states from σ to ρ, and $\phi_{L\Lambda}$ is the spatial part of the bound state wave function of particle b. When there is no spin-orbit coupling, further simplification of Eq. (4.1) is possible and one can obtain the DWIA formula in its cross-section factorized form.

In the present calculations, the NN scattering t matrix with the on-shell amplitude was approximately employed in the final energy prescription, although the two-body t matrix used for the $(p, 2p)$ reaction should be evaluated in the nuclear medium including off-shell properties. The t matrix was taken from the solution of the phase shift analysis by Arndt *et al.* [84]. The wave function for the bound nucleon was generated in the usual fashion as an eigenfunction of a Woods-Saxon well adjusted to reproduce the empirical separation energy. The corresponding geometrical parameters were taken from Ref. [85] for the s-hole states, while radius parameters reproducing the rms radius of the wave functions derived from the $(e, e'p)$ experiments [20, 21] were used for the p-hole states in the calculations of the previous section.

The distorted waves were calculated using the Schrödinger equivalent reduction of a Dirac global optical model parameters of Cooper *et al.* [86] which were obtained from fits to proton elastic scattering data taken at incident energies of 20 to 1040 MeV for ^{12}C, ^{16}O, ^{40}Ca, ^{90}Zr, and ^{208}Pb. In Ref. [86], three different E- and A-dependent global potentials (EDAD-1, 2, and 3) were presented. The potential dependence of the calculated $(p, 2p)$ cross section is not so small, for example, the cross section for the s-hole state in ^{15}N at the recoil momentum k_3=0 calculated with the EDAD-2 potential is 12 % larger than the calculation with the EDAD-1 potential. Moreover, other correction terms such as the non-locality effects cause significantly different results. The absolute values of the calculated cross sections might contain more than 20 % uncertainties. We mainly present here the results of the calculations with the EDAD-1 potential parameters. The calculated cross sections were corrected for the finite solid angles and were averaged over the spectrometer momentum acceptance using the input option of the THREEDEE code.

Recoil momentum dependence of the s-hole state in ^{11}B

The recoil momentum dependence of the ^{12}C$(p, 2p)$ reaction at E_p= 392 MeV for the s-hole state in ^{11}B was already investigated by Noro *et al.* [59, 94]. The integrated cross sections at $\theta_{\rm GR} = 25.5°$ for the energy region of 30 MeV$\leq E_{sep} \leq$60 MeV in ^{11}B are plotted as a function of recoil momentum in Fig. 4.3. The open circles show the integrated cross section including background processes and the closed circles correspond to the results after subtraction. The background were estimated by extrapolating the spectrum shape in the higher excitation energy region. Two lines are the results of DWIA calculations with a global optical potential [86] and with a potential deduced by a relativistic impulse approximation [95]. Both of the DWIA results, which are normalized to the experimental data, give good fits to the experimental data with background subtraction. Moreover the choice of the optical potential is not sensitive to the recoil momentum distribution. They concluded that the inclusion of non-quasifree processes around the s-hole state in the ^{12}C$(p, 2p)$ reaction was less than 10 % in the present kinematical condition ($k_3 \approx 0$). The spectroscopic strength is dependent on the optical potential, bound state wave function, *etc.* When we assumed this 10 % background for the data of the present experiment, the spectroscopic strength extracted from the DWIA calculations with the parameters mentioned above exhausts 72 % of the IPSM in the region of the excitation energies of 16 MeV to 35 MeV.

Recoil momentum dependence of the s-hole state in ^{15}N

The angular correlation of the ^{16}O$(p, 2p)$ reaction for the s-hole state in ^{15}N were measured at $\theta_{\rm GR} = 25.5°$ in the present experiment. In Fig. 4.4(a), the cross sections integrated over the excited energy region of 16 MeV $\leq E_x(^{15}\text{N}) \leq$ 40 MeV are plotted as a function of the angle of LAS, which is equivalent the recoil momentum dependence. (The LAS angles of 30° to 65° correspond to the recoil momenta of -100 MeV/c to 150 MeV/c.) Since the higher excitation region is out of the full momentum acceptance in the present magnetic field setting, we assumed the constant non-quasifree background for the cross sections of all angles and fitted the data with the DWIA calculation + constant background. Good fits were obtained for the whole regions except for the slightly large experimental value at $\theta_{\rm LAS}$= 65°. The fitting result of the DWIA calculations with a constant background is also shown in Fig. 4.4(a) by solid and dashed curves. The spectroscopic strength of $1s_{1/2}$ below E_x = 40 MeV exhausts about 80 % of the IPSM. At the point of maximum cross section, the mixture of non-quasifree backgrounds of 15 % is estimated.

The microscopic structure of the s-hole state has recently discussed with the shell-

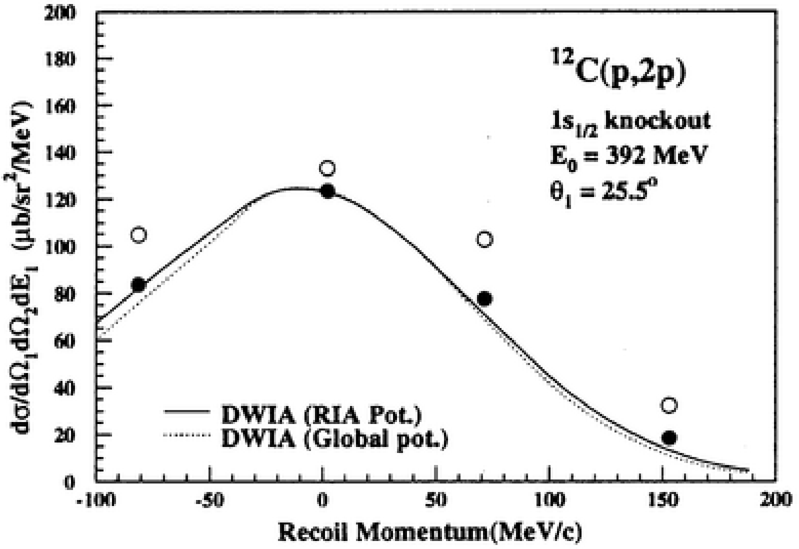

Figure 4.3: Recoil momentum dependence of the ^{12}C$(p, 2p)$ reaction for the s-hole state in ^{11}B obtained by Noro *et al.* [94]. Open circles are the integrated cross section over the s-hole region and the closed circles are those after subtraction of the background. Two curves are the results of the DWIA calculations with different optical potentials, which are normalized to the experimental data.

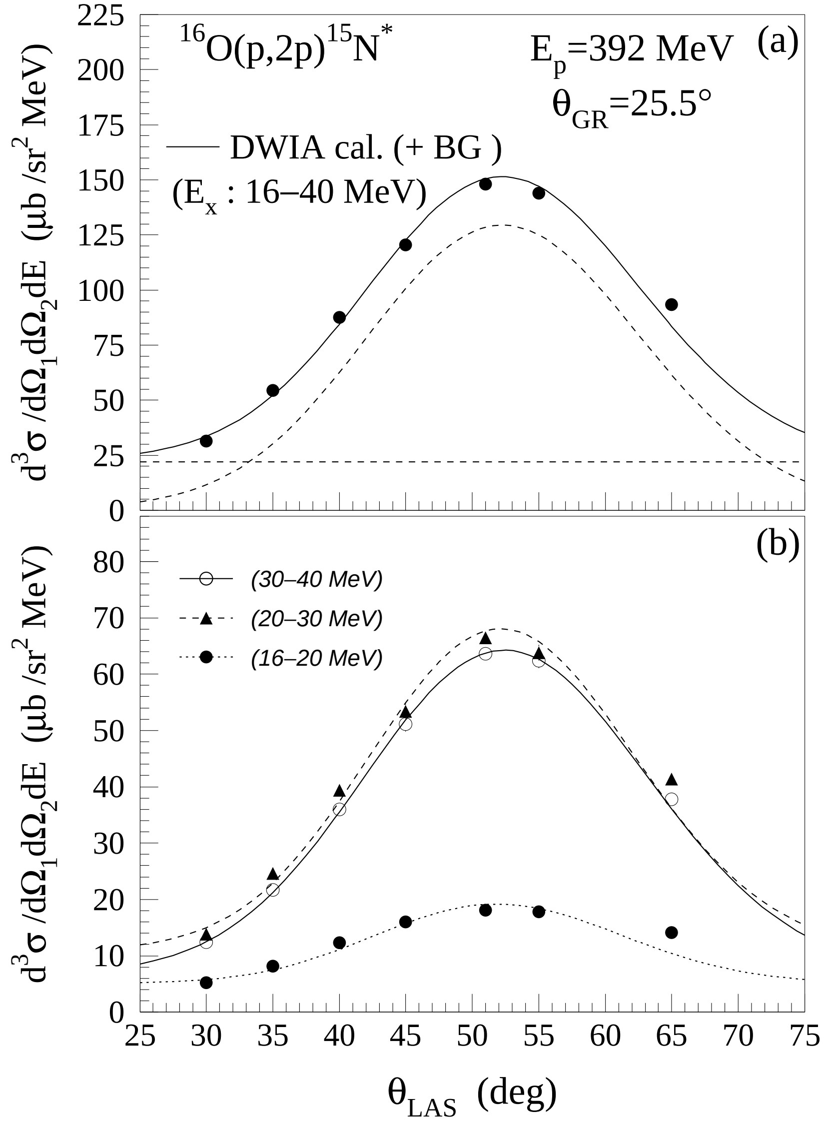

Figure 4.4: (a) Angular correlation of the ^{16}O$(p, 2p)$ reaction for the *s*-hole state in ^{15}N, which corresponds the recoil-momentum dependence of the differential cross sections. The closed circles are the measured cross sections integrated in the region of 16 MeV$\leq E_x \leq$40 MeV. The fitting result by the DWIA calculations with a constant background is shown by solid and dashed curves. (b) The same as figure (a), except for the three integrated energy region of 16 MeV$\leq E_x \leq$20 MeV (closed circles), 20 MeV$\leq E_x \leq$30 MeV (triangles) and 30 MeV$\leq E_x \leq$40 MeV (open circles), respectively. Three lines are the results of the DWIA calculations with mean separation energies in each energy region.

model calculations by Yamada [96]. Experimentally, a bump at 17 MeV with relatively narrow width and a broad bump around 30 MeV are recognized in the s-hole region of the ^{15}N excitation energy spectrum. We separate the bump region into three pieces: 16-20 MeV, 20-30 MeV and 30-40 MeV, especially in order to ascertain that the 17 MeV bump has a character of the s-hole state. In comparison with DWIA calculations, the angular correlations of all three regions are consistent with that of the s-hole state (see Fig. 4.4(b)), in which a flat distribution of background in each region was also assumed.

4.2.2 Strength distributions of the s-hole states

Shell-model calculations

The bumps corresponding to the s-hole states in ^{11}B and ^{15}N obviously split into some components as shown in Fig. 3.9(a) and (b). For the ^{11}B(s-hole) state, a similar structure could be dimly seen in the spectra of the $^{12}\mathrm{C}(e,e'p)^{11}\mathrm{B}$ experiment [76] and $^{12}\mathrm{C}(p,d\pi^+)^{11}\mathrm{B}$ reaction [97]. However, the statistics was not enough and, therefore, the splitting of the s-hole state had never been discussed before our preliminary results were presented [52, 53, 98].

Stimulated by our experimental data, Yamada has recently performed new calculations to study the bump structure within the framework of the 1 $\hbar\omega$ shell model [96]. The excitation spectrum of the $(p,2p)$ reaction was formulated within the impulse approximation,

$$\frac{d^3\sigma}{d\Omega_1 d\Omega_2 dE} = \left(\frac{d\sigma}{d\Omega}\right)_{NN} \sum_i F(E;E_i,\mathit{\Gamma}_i) S_i^2, \tag{4.3}$$

where $(d\sigma/d\Omega)_{NN}$ is the NN c.m. cross section, i denotes the i-th eigenstate obtained by the $1\hbar\omega$ shell-model calculations for $^{11}\mathrm{B}(\frac{1}{2}^+)$ [$^{15}\mathrm{N}(\frac{1}{2}^+)$], and calculated energy-dependent spectroscopic factors S_i^2 for the ^{12}C(g.s.)→ $p+^{11}\mathrm{B}(\frac{1}{2}^+)_i$ [^{16}O(g.s.)→ $p+^{15}\mathrm{N}(\frac{1}{2}^+)_i$] process were folded by a Lorentzian function $F(E,E_i,\mathit{\Gamma}_i)$. E_i and $\mathit{\Gamma}_i$ are the eigenenergy and total fragmentation width of the i-th eigenstate. $\mathit{\Gamma}_i$ is given as the sum of the partial fragmentation widths ($\mathit{\Gamma}_n$, $\mathit{\Gamma}_p$, $\mathit{\Gamma}_d$, $\mathit{\Gamma}_t$, and $\mathit{\Gamma}_\alpha$) for the 2-body n-, p-, d-, t- and α-decay channels. The partial fragmentation widths are evaluated with the separation energy method [101], where the decay width is given by the product of twice the penetration factor P_l and the reduced width γ_l^2;

$$\begin{aligned} \mathit{\Gamma}_l &= 2P_l\,\gamma_l^2, \\ P_l &= ka/(G_l^2+F_l^2), \\ \gamma_l^2 &= \theta_l^2(a)\,\gamma_W^2(a),\ \ \gamma_W^2 = \frac{3\hbar^2}{2\mu a^2}, \end{aligned} \tag{4.4}$$

where k is the wave number, F_l and G_l are the regular and irregular Coulomb wave functions, a is a channel radius, and the quantity θ_l^2 is the reduced amplitude in the unit of the Wigner limit value. In the calculations of the shell-model wave functions, the Cohen-Kurath interaction for $(1p)$-shell [99], the Millener-Kurath one for $(1p)$-$(2s1d)$ and $(1s)^{-1}$-$(1p)$ cross shells [100], and G-matrix elements for the Reid soft-core potential or the Bonn potential for others are used.

Sub-structure of the s-hole state in ^{11}B

In order to investigate the sub-structure of the s-hole state in ^{11}B, we fitted the excitation energy spectra between 11 MeV and 40 MeV with several peaks and a non-quasifree background. An asymmetric Lorentz formula [102] folded with an experimental energy resolution function was assumed for the shape of each peak. The asymmetric Lorentz shape is written as

$$f(E) \propto \frac{1 + (E - E_r)A}{(E - E_r)^2 + \mathit{\Gamma}^2/4}, \tag{4.5}$$

where E_r and $\mathit{\Gamma}$ is the central energy and width of the peak, respectively. This shape agrees with the theoretical spectral function derived by Sartor and Mahaux [32] for deep hole states. In the fitting procedure, A is determined so that $f(E)$=0 at the particle decay threshold energy. We fixed the integrated value of the background function to 10 % of the total yields, according to the results of the previous section. Here we adopted an almost flat background multiplied by a function gradually decreasing to zero at the threshold energy of the three-particle emission. At least three broad peaks except for two small sharp peaks at 11.7 MeV and 13.2 MeV were needed to obtain a good χ^2 value. The fitting result is shown in Fig. 4.5(a) with the experimental excitation spectrum of ^{11}B. The central energies (widths) of three broad peaks are 16.5±0.1 MeV (5.3±0.3 MeV), 21.8±0.2 MeV (8.1±0.3 MeV), and 28.6±0.7 MeV (9.7±2.5 MeV), respectively. The denoted errors are the maximum deviations of the fitting results obtained when the background contribution were varied from 5 % to 15 %. When integrating these peaks up to the excitation energy of 50 MeV, we can obtain the spectroscopic strength that exhausts 95 % of the IPSM in comparison with the DWIA calculations.

The excitation energy spectra derived from the shell-model calculations are shown in Fig. 4.5(b). Solid and dashed curves are, respectively, the results with use of the Reid soft-core potential and the Bonn potential. In both calculations, the distributions of the $\frac{1}{2}^+$ states in ^{11}B mainly split into three parts. Although the calculated strength ratios of the three regions are different from the experimental results, the sub-structure of the s-hole state is reasonably explained by the shell-model calculations. The experimental widths of three bumps are broader than the calculated ones,

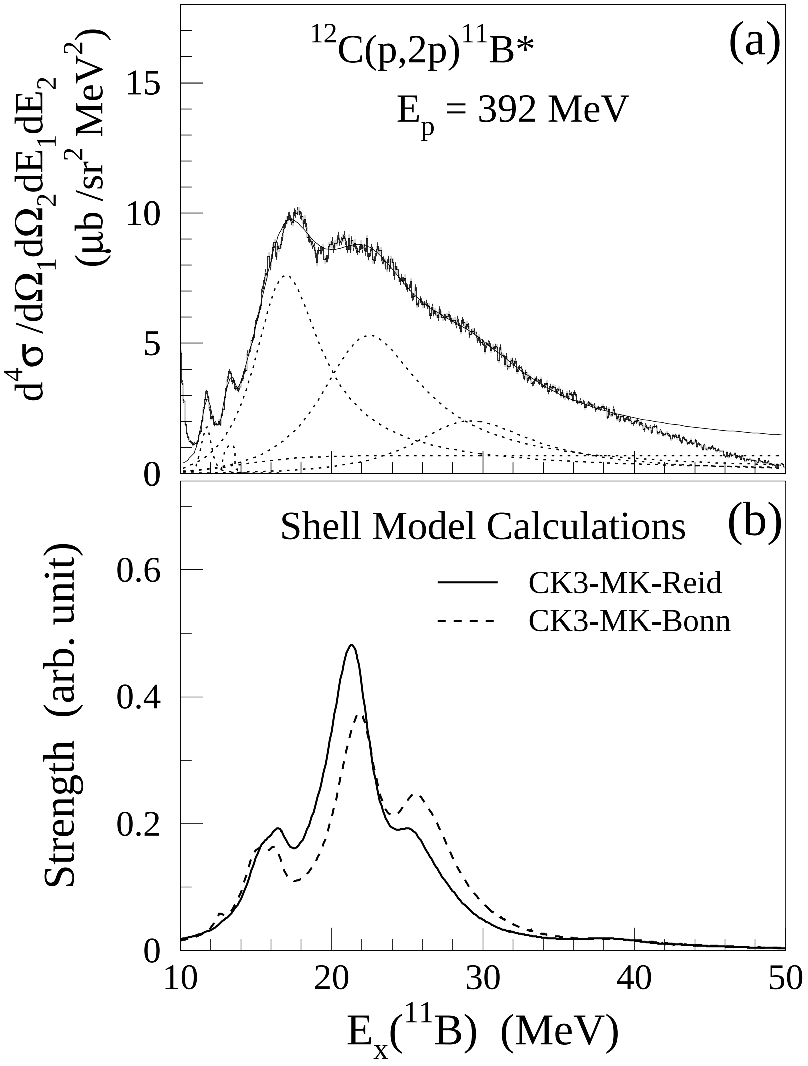

Figure 4.5: (a) Excitation energy spectrum of the s-hole region of ^{11}B. Dotted and solid lines show the results of a least χ^2 fit for the energy region between 11 MeV and 40 MeV (see text). The sum of all peaks (solid line) reproduces well the experimental data at energies below 40 MeV. The detection efficiency decreases gradually above this energy due to the finite momentum acceptance of the spectrometers. (b) Excitation spectra of ^{12}C$(p, 2p)^{11}$B$(1/2^+)$ reaction calculated with the 1 $\hbar\omega$ shell model using two different potentials [96].

suggesting that the spreading width by statistical decay also contributes to the total width because the calculated width only includes the escape width. The origin of the splitting of s-hole state will be discussed later together with the fragmentation of the s-hole state.

Sub-structure of the s-hole state in ^{15}N

In the similar way to the ^{11}B(s-hole) state, we fitted the excitation energy spectrum of ^{15}N between 14 MeV and 45 MeV with several peaks and a non-quasifree background. An asymmetric Lorentz formula folded with an experimental energy resolution function was assumed for the shape of each peak. The integrated value of the background function was fixed to 15 % of the total yields, according to the DWIA analysis for the recoil momentum dependence. The same background shape as that in the case of ^{11}B was used. At least two narrow peaks and three broad peaks were needed to obtain a good χ^2 value. The fitting result is shown in Fig. 4.6(a) with the experimental excitation spectrum of ^{15}N. The central energies (widths) of five peaks are 14.4±0.1 MeV (0.3±0.2 MeV), 17.0±0.1 MeV (1.0±0.1 MeV), 18.5±0.3 MeV (4.9±0.3 MeV), 26.6±0.2 MeV (11.5±1.1 MeV), and 33.9±0.2 MeV (8.9±0.7 MeV), respectively. The denoted errors are the maximum deviations of the fitting results obtained when the background contribution were multiplied by 0.5 to 1.5. When integrating these peaks up to the excitation energy of 50 MeV, we can obtain the spectroscopic strength that exhausts 94 % of the IPSM in comparison with the DWIA calculations.

The results of the shell-model calculations are shown in Fig. 4.6(b). Solid and dashed curves are, respectively, the results with use of the Reid soft-core potential and the Bonn potential. Two curves are slightly different in the high excitation region. The gross feature of the distributions of the $\frac{1}{2}^+$ states in ^{15}N is well reproduced by the shell-model calculations with the Reid soft-core potential, if the excitation energies extracted from the shell-model calculations would be shifted downward by about 5 MeV. The experimental total width, which includes both the escape and spreading widths, is larger than the calculated one similarly to the ^{11}B(s-hole) case.

4.3 Particle decay from the s-hole states

4.3.1 Decay angular correlation

The branching ratios of decay particles from the s-hole states in ^{11}B and ^{15}N are listed in Table 3.1 and Table 3.2, respectively, where we assumed that the decay particles were isotropically emitted because the s-hole state has no angular momentum and the recoil momentum was small and distributed around zero. In order to check

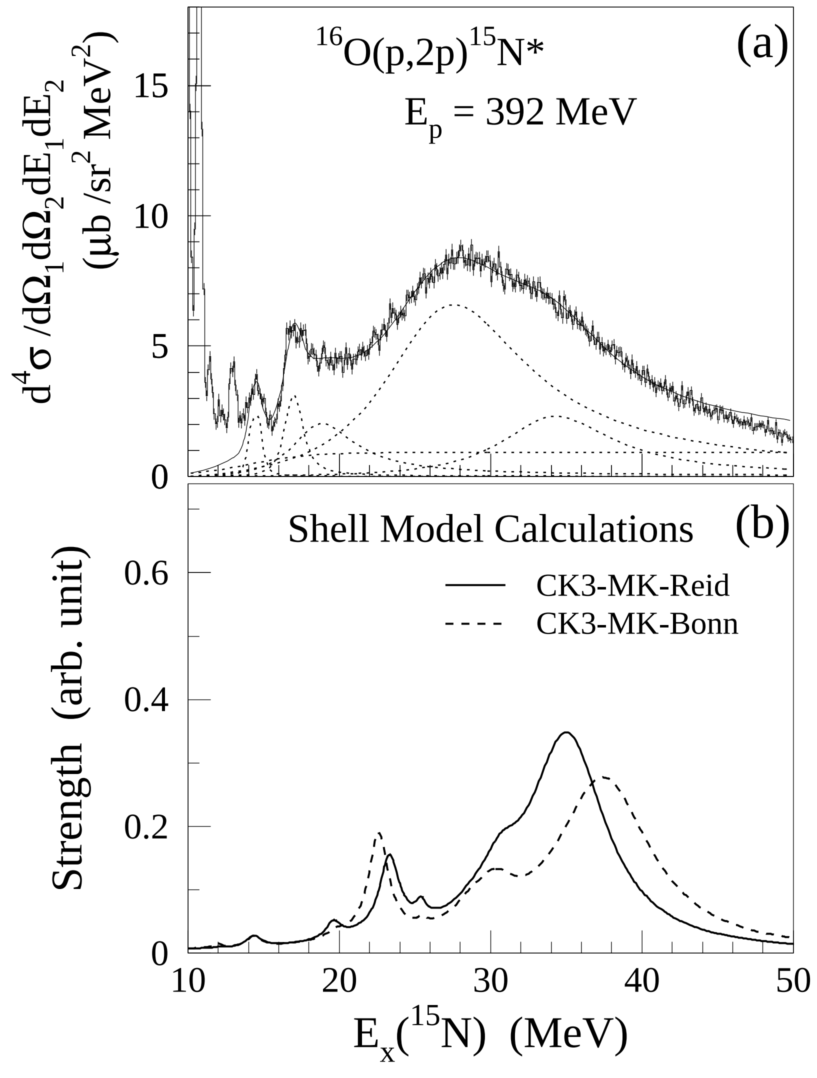

Figure 4.6: (a) Excitation energy spectrum of the s-hole region of ^{15}N. Dotted and solid Lines show the results of a least χ^2 fit for the energy region between 14 MeV and 45 MeV (see text). The sum of all peaks (solid line) reproduces well the experimental data at energies below 45 MeV. The detection efficiency decreases gradually above this energy due to the finite momentum acceptance of the spectrometers. (b) Excitation spectra of ^{16}O$(p, 2p)^{15}$N$(1/2^+)$ reaction calculated with the 1 $\hbar\omega$ shell model using two different potentials [96].

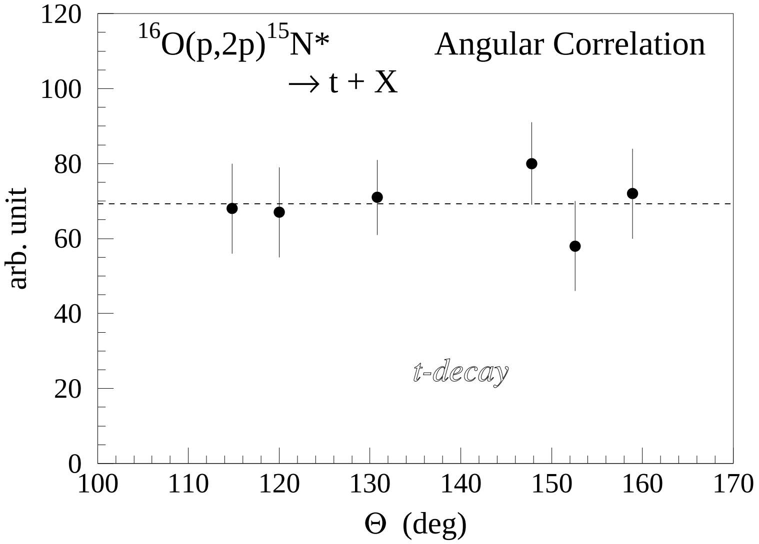

Figure 4.7: Angular correlation of t-decay from the s-hole state in ^{15}N. The abscissa is the scattering angle against the beam axis. Azimuthal angles of all points are not the same.

the assumption of isotropic decay, we evaluated the decay angular correlations from the yields of individual detectors. A sample spectrum for the t-decay channel in the $^{16}\mathrm{O}(p,2p)^{15}\mathrm{N}$ reaction is shown in Fig. 4.7 and a spectrum for the n-decay onto the '2-body decay' region is plotted in Fig. 4.8. Although the statistics for the individual detector is, unfortunately, not enough, the obtained angular correlations are not inconsistent with the isotropic decay. As an exception, the yield of the detector set at the most forward angle (θ_n= 100°) is slightly enhanced when n-decay is evaluated without the cut for the '2-body decay' region. However, this effect is small compared to the rather large statistical error of the n-decay branching ratio.

4.3.2 Statistical-decay calculations

As mentioned, the fragmentation of the s-hole state occurs through two processes: the statistical decay of the compound nucleus and the direct decay of the doorway s-hole state. The latter is discussed in terms of the microscopic SU(3)-cluster model [33] and the shell model [96], and the calculated results predict a selection rule for the fragmentation of the s-hole states in light nuclei. On the other hand, there are no quantitative calculations for the statistical decay of the s-hole states in light nuclei.

The experimental branching ratios of decay particles from the excitation energy

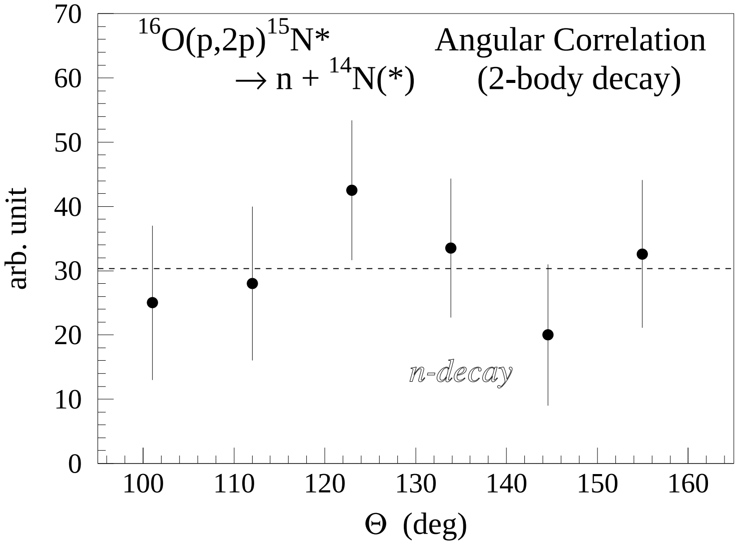

Figure 4.8: Angular correlation of n-decay from the s-hole state in ^{15}N onto the '2-body decay' region. The abscissa is the scattering angle against the beam axis. Each point indicates the summed value of a set of five detectors.

region of the s-hole states are first compared to the branching ratios with the statistical decay of a compound nucleus. The computer code CASCADE [103] is used for doing the statistical-decay calculations. (The version CASCIP that treats isospin and parity exactly is employed because the isospin plays an important role in determining the branching ratios for light nuclei.) A compound nucleus (C^*) in statistical equilibrium decays eventually through the emission of a nucleon, a cluster or a deexciting photon.

$$C^* \longrightarrow x + B, \tag{4.6}$$

where nucleus B may also be in an excited compound state which will decay. The calculation is performed for a decay cascade starting from a certain specified state ($\frac{1}{2}^+$ state in the present case), although the code can treat the initial formation of a compound nucleus by a fusion reaction.

The decay of the compound nucleus by particle emission is calculated from the Hauser-Feshbach formula [104]. The decay probabilities are determined by the statistical weight of the final state and the barrier penetrabilities for various channels. Following the presentation of Thomas [105], the particle emission probability is written in terms of transmission coefficients T_L^x. The rate $R_x d\varepsilon_x$ $(= \mathit{\Gamma}_x(\varepsilon_x)/\hbar)$ for emitting a particle x from an excited nucleus 1 with excitation energy E_1, spin J_1, and parity

π_1 to form a product nucleus 2 (at E_2, J_2, π_2) is

$$R_x d\varepsilon_x = \frac{\rho_2(E_2, J_2, \pi_2)}{2\pi\hbar\rho_1(E_1, J_1, \pi_1)} \sum_{S=|J_2-s_x|}^{J_2+s_x} \sum_{L=|J_1-S|} T_L^x(\varepsilon_x) d\varepsilon_x, \tag{4.7}$$

where ε_x and s_x are, respectively, the kinetic energy and spin of particle x, L is its orbital angular momentum, $\boldsymbol{S} = \boldsymbol{J_2} + \boldsymbol{s_x}$ is the channel spin, and ρ is the level density. The transmission coefficients T_L^x were calculated using the code TLCAL [108] with the global optical potential parameters of Ref. [109, 110, 113, 111, 112], which are well suited for light nuclei. The dependence of the calculated results on the optical potential parameters is described in Appendix B.

The level density ρ in addition to T_L^x is needed for the statistical-model calculations. In the CASCADE code, the energy scale is separated into four regions:

Region 1 (low excitation energy): The experimentally known levels are used.

Region 2 (medium excitation energy): The level density is calculated using a *back-shifted Fermi-gas model* [106, 107]. The level density parameter a and the back shift Δ are determined empirically for each nucleus (for example, in Ref. [114]).

Region 3,4 (High excitation energy): In this region, it is assumed that all nuclei behave as predicted by the liquid-drop model. The level density parameter a is set equal to $A/8$ MeV^{-1} in region 4 and the level density in region 3 are obtained by a smooth interpolation between region 2 and 4.

In the present calculations, the regions 1 and 2 are mostly important. Here, the energy levels known below 12 MeV excitation energy [115] were explicitly included for all nuclei ($6 \leq A \leq 15$) necessary for the calculations, while the levels at higher excitation energies were calculated using the parameters a and Δ given in the code.

In the CASCADE calculations, only neutron, proton, α-particle and other one-cluster emissions are treated simultaneously for decaying particles. We carried out the calculations for three sets: (n, p, α, d), (n, p, α, t), and (n, p, α, ^{3}He), and next averaged them with proper weights so that the yield of n+p+α for the first step decay become the same value. In this procedure, some sequential decay processes like t-decay after d-decay are, unfortunately, not included but the probabilities of these processes are considered to be small. The calculations were done for the excitation energies between 10 MeV and 50 MeV with the bin size of 0.2 MeV. The obtained decay probabilities at each energy was multiplied by the experimental cross section.

In evaluating the branching ratios from the results of the CASCADE calculations, decay particles above the experimental detection thresholds were only employed, taking into account not only the lower limit of the detection energies in the SSD telescopes

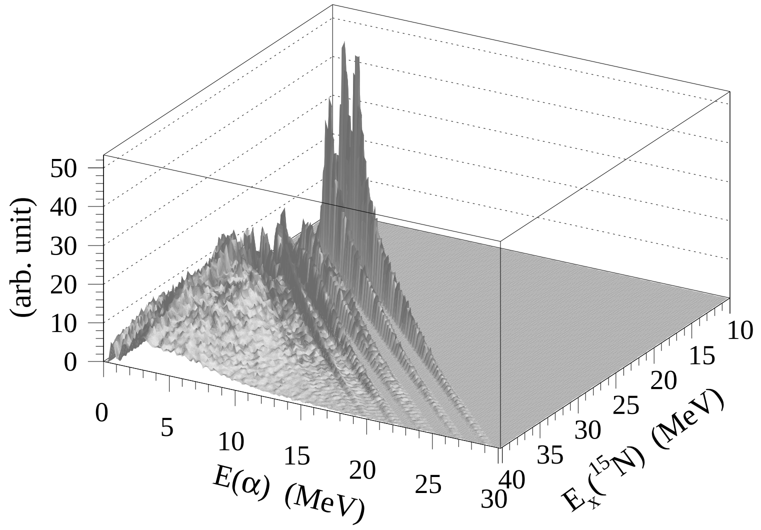

Figure 4.9: α-decay spectrum of the excited states in ^{15}N calculated with the code Cascade. The experimental differential cross section is used for the weight of each point of the excitation energy of ^{15}N. The linear loci indicate the 2-body decay, while the bump structure seen at the left side is mainly due to the sequential decay.

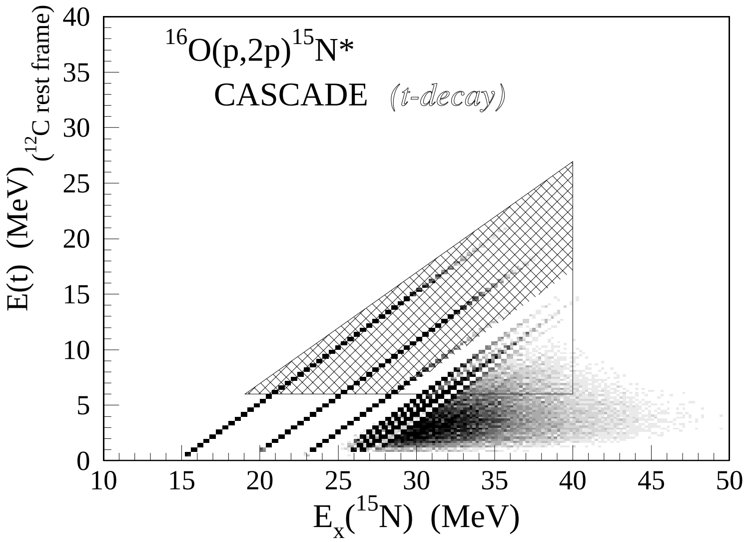

Figure 4.10: Two dimensional plot of t-decay from the excited states in ^{15}N calculated with the code Cascade. The region surrounded by solid lines is used for the comparison with the experiment. The hatched region corresponds to the '2-body decay' region defined in the text.

Table 4.1: Gate conditions for the ‘2-body decay’ regions in the statistical-decay calculations. $E_x(res)$ is the excitation energy of the each residual nucleus and E_{dcy} is the kinetic energy of each decay particle. The lower limit of E_{dcy} is determined by taking into account the threshold of the detectable energy in the SSD telescopes and the mean energy loss of emitted particles in the target.

	^{11}B		^{15}N	
	$E_x(res)$	E_{dcy}	$E_x(res)$	E_{dcy}
n	∼5.0 MeV	3.1 MeV∼	∼8.2 MeV	3.2 MeV∼
p	∼6.8 MeV	3.1 MeV∼	∼8.2 MeV	3.2 MeV∼
d	∼5.0 MeV	4.1 MeV∼	∼8.0 MeV	4.2 MeV∼
t	∼5.0 MeV	4.7 MeV∼	∼8.0 MeV	4.8 MeV∼
α	∼5.0 MeV	4.8 MeV∼	∼8.7 MeV	5.5 MeV∼

but also the mean energy losses of emitted particles in the target. The small branching ratio of ^{3}He-decay was included in that of α-decay. It should be noted that, in the output of the code CASCADE, the energy of the emitted particle is given as the value in the target-rest frame.

A sample spectrum of the result of the CASCADE calculations is shown in Fig. 4.9 for the α-decay from the excited states in ^{15}N. The linear loci corresponding to the low excitation levels of ^{11}B indicate the binary decay processes, while the bump structure in the left-side region is mainly due to the sequential cascade decay. The ‘2-body decay’ regions are also defined for the results of the CASCADE calculations in the exactly same manner as the experimental ‘2-body decay’ regions. In Fig. 4.10, the regions with the ‘2-body decay’ cut and without cut are shown for t-decay from the excited state in ^{15}N. The conditions for evaluating the branching ratios are summarized in Table 4.1.

4.3.3 Fragmentation of the s-hole state in ^{11}B

The experimental branching ratios of decay particles from the excitation energy region of 16–35 MeV in ^{11}B are shown in Fig. 4.11, together with the results of the statistical-model calculations. The branching ratios of the decay onto the ‘2-body decay’ regions are also indicated in Fig. 4.11 with dark areas. The measured branching ratios of both t-decay and α-decay are much larger than those of the statistical-model calculations. The experimental α-decay in the ‘2-body decay’ region is about one half of the total α-decay, suggesting that contributions of the sequential decay and 3-body decay processes are large in this channel. It should be noted that the α+α+t 3-body decay channel has a very low threshold energy of 11.2 MeV and may compete against

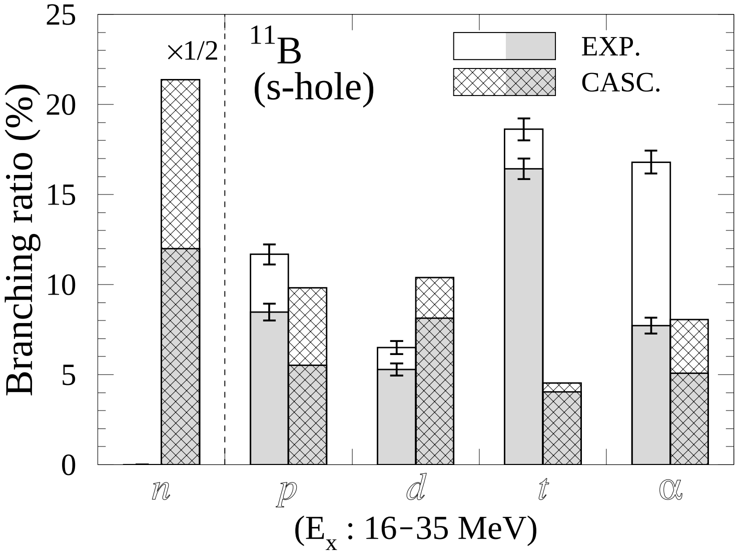

Figure 4.11: Comparison of the measured branching ratios of the p-, d-, t- and α-decays from the s-hole state in ^{11}B (16–35 MeV) with those of the statistical-model calculations using the code Cascade. The error bars shown include only statistical ones. The branching ratio of the n-decay with the energy above 3.1 MeV is also shown in the results of the statistical-model calculations. The branching ratios of the decay onto the '2-body decay' regions are indicated with dark areas (see text).

the 2-body decay process, while the statistical-model calculations include only the 2-body decay and sequential decay processes. This suggests that the 3-body decay process could contribute significantly to the branching ratios of α-decay. However, even in the '2-body decay' regions, the t-decay strength is still dominant. Furthermore, the relative ratio of the t-decay to the α-decay in the experiment is opposite to that of the statistical-model calculation as well as the ratio of the p-decay to the d-decay. It is difficult to determine the proportion of the statistical process to the fragmentation obtained in the present experiment.

Fig. 4.12(a) and (b) show the branching ratios of p-, d-, t- and α-decays in the whole regions and '2-body decay' regions, respectively, from the three excitation energy regions of 16–20, 20–26 and 26–35 MeV in ^{11}B. The difference between Fig. 4.12(a) and (b) is prominent in the energy region of 26–35 MeV, where the decay probabilities of not only α-particles but also protons are much reduced. As shown in Fig. 4.12(b), the decay patterns from the respective regions suggested by the substructures are very different, indicating that the s-hole state in ^{11}B splits into some components with different microscopic structures. Owing to the detection threshold, the measured deuteron branching ratio is zero in the low energy region. Predictions from the microscopic cluster model [33] are shown in Fig. 4.12(c), where the ^{11}B(s-hole) state has the same spatial symmetry as the ground state of ^{12}C, SU(3)($\lambda\mu$)=(04), and has two degenerated partition symmetries [f]=[443] and [4421]. The partial decay widths are calculated using the separation energy method of Eq. (4.4). The calculations in Ref. [33] were made for an assumed centroid excitation energy of E_x = 20 MeV. The energy dependence of the calculated branching ratios is not so much large as the qualitative change is caused in Fig. 4.12(c), although the calculated partial widths depend significantly on the energy. The branching ratio of α-decay is exactly zero in the calculations of the microscopic cluster model due to the selection rule. It should be noted that the SU(3)-cluster model calculations did not take into consideration the experimental limitation like the detection threshold. When the branching ratios of α-decay is neglected, the experimental decay pattern of the 26–35 MeV region is similar to that of the SU(3)[f]($\lambda\mu$)=[443](04) component. The first and second regions may have both the SU(3)[f]($\lambda\mu$)=[4421](04) and [443](04) components, whereas the mixing of [4421](04) component seems to decrease with increase of the excitation energy. The suppression of α-decay compared to p-decay and d-decay is, however, not clearly supported in the present experiment.

The energy dependence of the branching ratios for n-, p-, d-, t-, and α-decays from the ^{11}B(s-hole) state were also calculated by Yamada [96] with the shell model as mentioned in § 4.2.2. The results of the shell-model calculations with the Bonn potential and the Reid soft-core potential are shown in Fig. 4.13(a) and(b), respectively. The

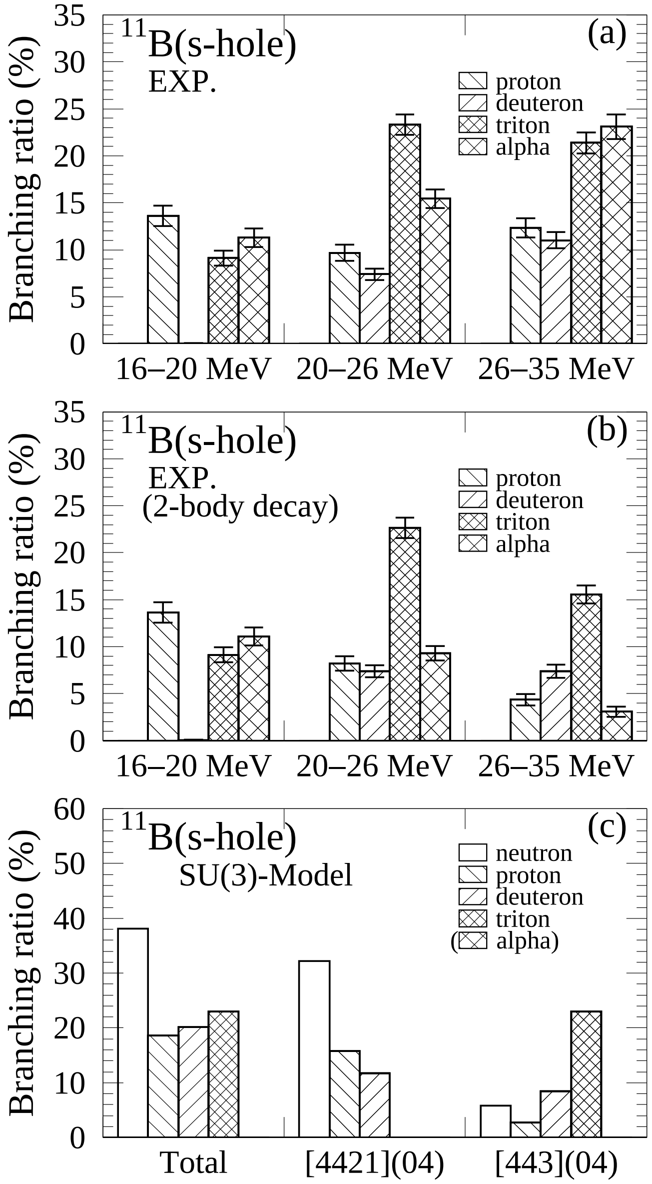

Figure 4.12: (a) Experimental branching ratios of the p-, d-, t- and α-decays from the three excitation energy regions of 16–20, 20–26 and 26–35 MeV in ^{11}B. (b) The same as (a), except for the decay onto the '2-body decay' regions. (c) Branching ratios of the n-, p-, d-, t- and α-decays from the doorway s-hole state in ^{11}B calculated by the microscopic cluster model with SU(3) wave functions [33]. Branching ratios for the states with $[f](\lambda\mu)$=[4421](04) and $[f](\lambda\mu)$=[443](04) and total branching ratios are shown.

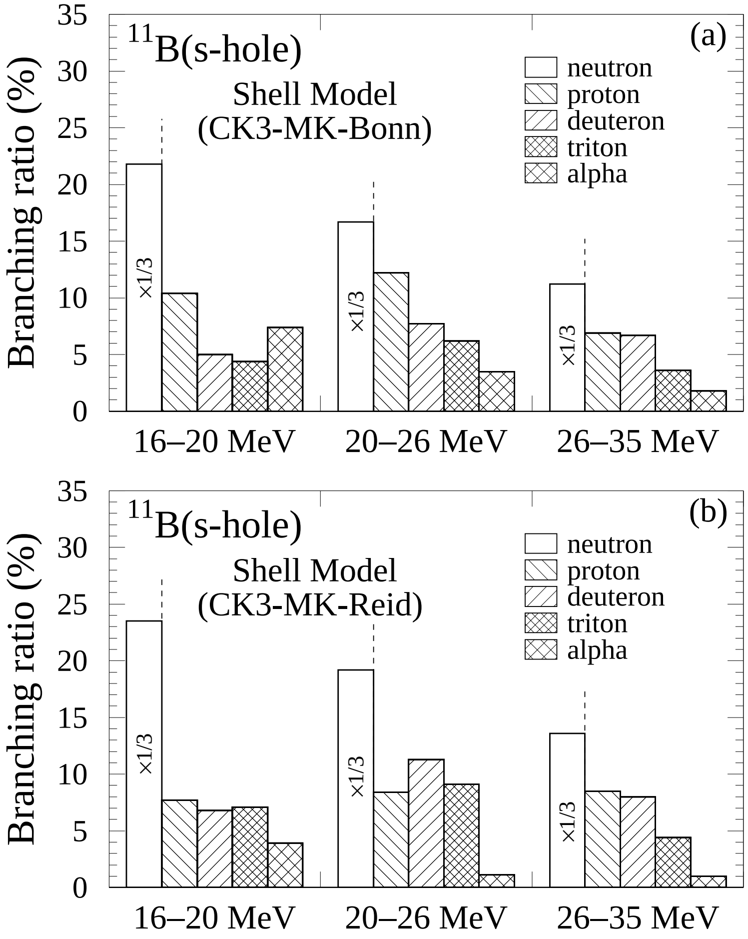

Figure 4.13: Branching ratios of the n-, p-, d-, t- and α-decays from the three excitation energy regions of 16–20, 20–26 and 26–35 MeV in ^{11}B obtained by the $1\hbar\omega$ shell-model calculations. [96] The results with two different G-matrix elements are shown for (a) the Bonn potential and (b) the Reid soft-core potential.

calculated branching ratio of the t-decay is larger than that of the α-decay, reflecting the selection rule as mentioned above. The calculated decay pattern in the low energy region (16 MeV–20 MeV) is fairly consistent with the experimental one. The enhancement of the t-decay observed in the higher energy regions, however, is not reproduced by the shell-model calculations. The reason why the SU(3)($\lambda\mu$)=[443](04) feature in the microscopic cluster model calculations disappears in the shell-model calculations is not clear. One of the differences is that ($\lambda\mu$)=(04) is assumed for the ^{11}B(s-hole) state in the microscopic cluster model, while the ^{12}C ground state in the shell model is described as

$$|^{12}\mathrm{C(g.s.)}> = \sqrt{0.784}[444](04) + \sqrt{0.173}[4431](21) + \cdots (\text{Cohen-Kurath}), \quad (4.8)$$

consequently the [4421](21) component is excited in ^{11}B(s-hole) as well as the [443](04) and [4421](04) states. As a result, the three components are coupled each other, and then the s-hole component splits mainly into three parts (see Fig. 4.5(b)). The coupling of the [4421](21) state allows the decay of α particles and might decrease the probability of t-decay. Further calculations including the direct 3-body decay process will be needed to explain the experimental decay pattern.

4.3.4 Fragmentation of the s-hole state in ^{15}N

In the case of the s-hole state in ^{15}N, the 3-body decay threshold is higher than those of the 2-body n-, p-, d-, t-, and α-decay. Moreover, the ground state of ^{16}O is more purely described as SU(3)($\lambda\mu$)=(00) state. Thus, the ^{15}N is more suitable to understand the microscopic structure and fragmentation mechanism of the s-hole state.

The experimental branching ratios of decay particles from the excitation energy region of 20–40 MeV in ^{15}N are shown in Fig. 4.14, together with the results of the statistical-model calculations. (Since, in the excitation energy below 20 MeV, only n- and p-decays are possible, we evaluated the branching ratios in Fig. 4.14 without the first region (16 MeV–20 MeV).) The branching ratios of the decay onto the '2-body decay' regions are also indicated in Fig. 4.14 with dark areas. The neutron fragments account for about a half of the total decay fragments in both the measurements and the statistical-model calculations. Only the measured branching ratio of t-decay is much larger than that of the statistical-model calculations. The n-decay and p-decay are considerably reduced in the '2-body decay' regions, suggesting the sequential decay processes are large in these channels. In the '2-body decay' regions, the measured n-decay and t-decay are larger than those of the statistical-model calculations, while the measured p-, d-, and α-decays are reasonably explained by the calculations. Although

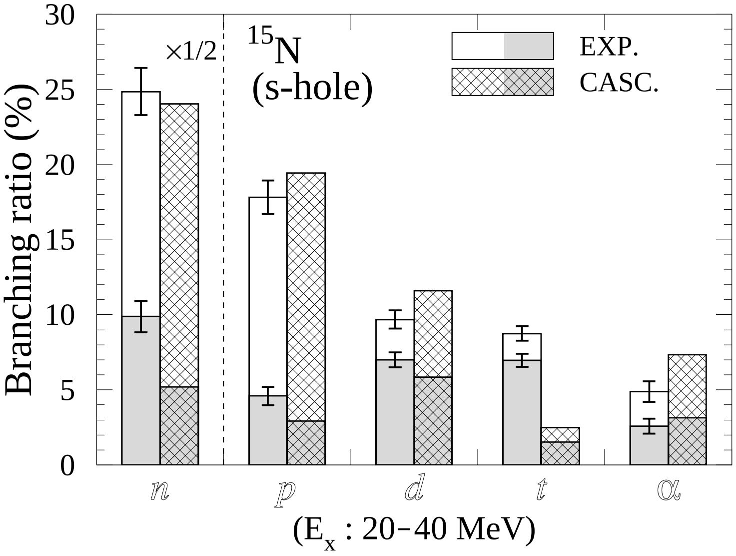

Figure 4.14: Comparison of the measured branching ratios of the n-, p-, d-, t- and α-decays from the s-hole state in ^{15}N (20–40 MeV) with those of the statistical-model calculations using the code Cascade. The error bars shown include only statistical ones. The branching ratios of the decay onto the '2-body decay' regions are indicated with dark areas (see text).

the large t-decay compared to α-decay supports the selection rule coming from the SU(3) spatial symmetry, the portion of the statistical decay may be considerable.

Fig. 4.15(a) and (b) show the branching ratios of n-, p-, d-, t- and α-decays in the whole regions and '2-body decay' regions, respectively, from the three excitation energy regions of 16–20, 20–30 and 30–40 MeV in ^{15}N. The difference between Fig. 4.15(a) and (b) is large in the energy region of 30–40 MeV, where the decay probabilities of neutrons, protons, and α-particles are much reduced. As shown in Fig. 4.15(b), the decay patterns between the lower region and higher region of the bump with the mean energy of 28 MeV are very different, indicating that this s-hole bump in ^{15}N includes a few components with different microscopic structures. Predictions from the microscopic cluster model [33] are shown in Fig. 4.15(c), where the ^{15}N(s-hole) state has the same spatial symmetry as the ground state of ^{16}O, SU(3)$(\lambda\mu)$=(00), and has two degenerated partition symmetries $[f]$=[4443] and [44421]. The calculations were made for an assumed centroid excitation energy of E_x = 30 MeV. The branching ratio of α-decay is exactly zero in the calculations of the microscopic cluster model due to the selection rule. The experimental decay pattern of the 30–40 MeV region strongly supports the selection rule and are similar to that of the SU(3)$[f](\lambda\mu)$=[4443](00) component. However, the large branching ratios of d-decay in the SU(3)-cluster model calculations do not agree with the experimental branching ratio, even taking into account the rather large lower limit of the detection energy. The second region may have both the SU(3)$[f](\lambda\mu)$=[44431](00) and [4443](00) components.

The branching ratios for two energy regions calculated with the shell model are shown in Fig. 4.16 for n-, p-, d-, t-, and α-decays from ^{15}N(s-hole) state. Here, the energy regions are shifted by 5 MeV compared to the experimental ones, reflecting the difference of the excitation spectra (see Fig. 4.6). The calculated results with the Bonn potential and the Reid soft-core potential are plotted in Fig. 4.16(a) and (b), respectively. The results of the both calculations are very similar. The branching ratio of the α-decay is very small owing to the selection rule as mentioned above. The agreement between the experimental branching ratios onto the '2-body decay' regions and calculated ones is fairly well in both the two regions, implying that the main part of the binary fragmentation is the direct decay of the doorway s-hole state. At first sight this seems to be inconsistent with the results obtained from the comparison with the statistical-decay calculations, where some (not small) amounts of the statistical decay are considered to contribute to the total branching ratios.

In order to try to separate the escape and spreading widths, we first assumed that the decay fragments to the higher excitation energies in the residual nuclei beyond the '2-body decay' regions were mainly produced by the sequential statistical-decay

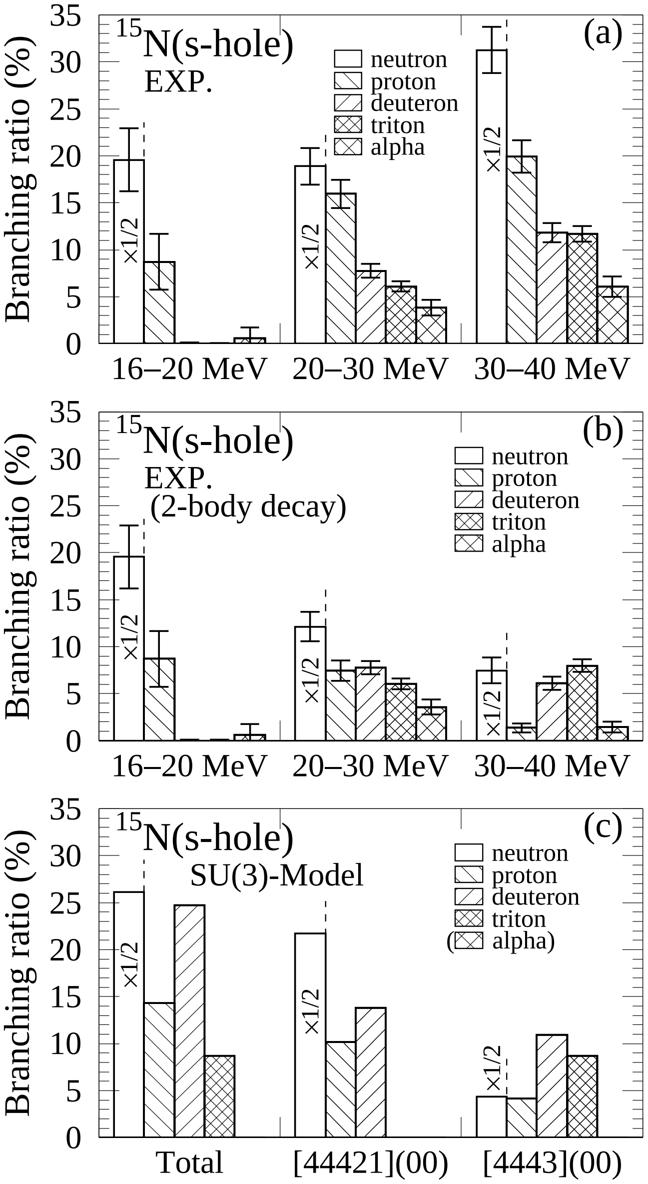

Figure 4.15: (a) Experimental branching ratios of the n-, p-, d-, t- and α-decays from the three excitation energy regions of 16–20, 20–30 and 30–40 MeV in ^{15}N. (b) The same as (a), except for the decay onto the '2-body decay' regions. (c) Branching ratios of n-, p-, d-, t- and α-decays from the doorway s-hole state in ^{15}N calculated by the microscopic cluster model with SU(3) wave functions [33]. Branching ratios for the states with $[f](\lambda\mu)$=[44421](00) and $[f](\lambda\mu)$=[4443](00) and total branching ratios are shown.

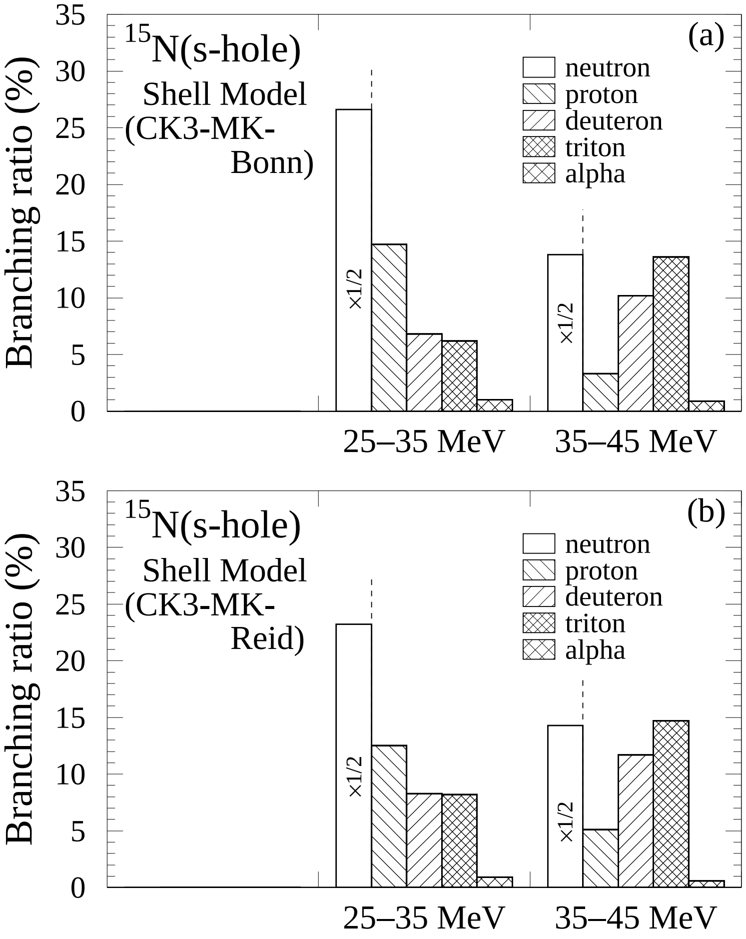

Figure 4.16: Branching ratios of the n-, p-, d-, t- and α-decays from the two excitation energy regions of 25–35 and 35–45 MeV in ^{15}N obtained by the $1\hbar\omega$ shell-model calculations. [96] The results with two different G-matrix elements are shown for (a) the Bonn potential and (b) the Reid soft-core potential.

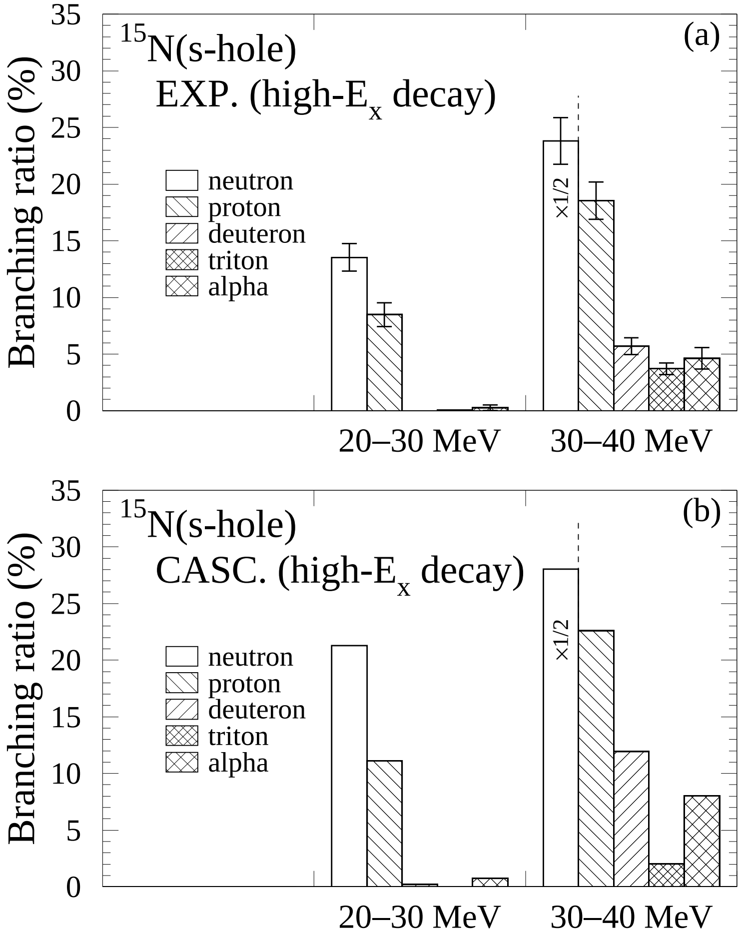

Figure 4.17: Comparison between (a) the experimental branching ratios and (b) the calculated ones with the code Cascade. The n-, p-, d-, t- and α-decays from the s-hole in ^{15}N onto the highly excited region in the residual nuclei beyond the '2-body decay' regions are shown in both figures.

process. The decay branching ratios obtained from subtracting the decay yields in the '2-body decay' region from the whole decay yields are shown in Fig. 4.17(a) and (b) for the measured ones and calculated ones with the statistical model, respectively. The decay patterns are very similar in both the spectra, except for t-decay. As mentioned before, in the present CASCADE calculations, the sequential t-decay after d-decay was not included. This may be one of the reasons why t-decay is small in the statistical-model calculations. The threshold energies of the 3-body decay channels, ^{12}C+p+n and ^{7}Li+2α, are less than 20 MeV and, then, some portions of the direct 3-body decay are included in the experimental values, while the direct 3-body decay is not taken into account in the statistical-model calculations. Therefore, we normalized the calculated branching ratios to the experimental ones using the value of d-decay. The normalization factor of 0.5 is obtained.

Next, we extracted the branching ratios of direct decay by subtracting the calculated statistical-decay ratios multiplied by 0.5 from the experimental ones in the '2-body decay' regions. The result is shown in Fig. 4.18(a). For a comparison, the result of the shell-model calculations of Fig. 4.16(b) multiplied by 0.5 is shown in Fig. 4.18(b). The agreement between two plots of branching ratios are very good not only for the decay patterns but also for the absolute values. We have not taken into consideration the non-quasifree background process of about 15 % in the discussion above, because we have no information on what particles are emitted through the background process. If it is assumed that no particles emitted at backward angles from the background process, the experimental branching ratios for the decay of the 'pure' s-hole state are all multiplied by 1.15. In that case, the normalization factor obtained by the procedure above also increases to 0.58. Taking into account this background effect, it is concluded that the ratio of the escape width ($\Gamma^{\uparrow}$) to the spreading width ($\Gamma^{\downarrow}$) of the ^{15}N(s-hole) state is about 0.7 to 1.

Finally, we shortly mention about the γ-decay of the s-hole state in ^{15}N. As shown in Fig. 3.16 and Fig. 3.22, the n-, p-, d, and t-fragments largely decay to the discrete excited states in residual daughter nuclei. These states are mostly deexcited by emitting γ-rays. (If the energy of the excited state is below its particle decay threshold, γ-ray decay rate is usually 100 %.) Although the energy resolution was not enough to separate each excited levels, the γ-rays of around 7 MeV from the excited states of ^{14}N and ^{14}C, and of 4.4 MeV from the ^{12}C(2^{+}) state will, particularly, be useful in the nucleon decay search in the water Čerenkov detectors as well as the γ-rays of 6.32 MeV, 9,93 MeV, *etc.* from the p-hole states. In Table 4.2, the yield ratios of the decay to excited states to the decay to the ground states are shown for the '2-body decay' regions and the branching ratios of the decay to excited states are also listed. In the '2-body decay' regions, γ-rays are mostly emitted except for a high

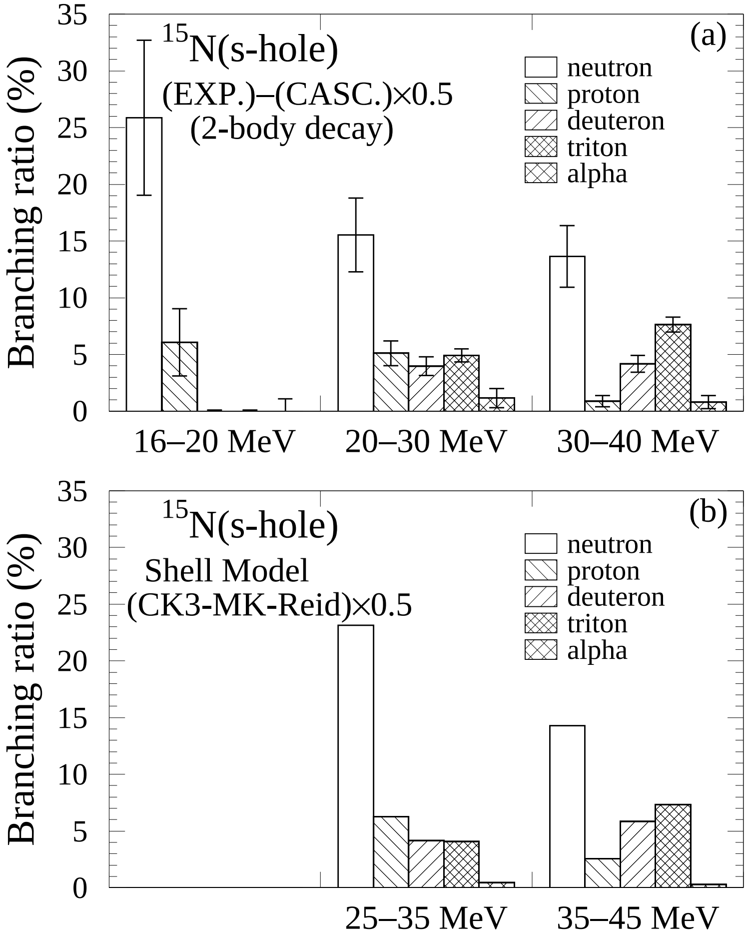

Figure 4.18: (a) Branching ratios of the *n*-, *p*-, *d*-, *t*- and α-decays onto the '2-body decay' regions obtained by subtracting 50 % of the statistical-decay ratios calculated with the code CASCADE from the experimental data. (b) The same as Fig. 4.16(b), but it is multiplied by 0.5.

Table 4.2: Ratios of the decay to the excited states to the decay to the ground states in the '2-body decay' regions for the ^{15}N(s-hole) state. The branching ratios of the decay to the excited states in the same regions are also listed. Only statistical errors are shown.

	N(excited)/N(g.s.)	Branching ratio (%)
n	2.3±0.5	15.5±1.7
p	3.4±1.2	3.9±0.6
d	2.7±0.5	4.5±0.4
t	2.4±0.3	4.3±0.3
α	1.7±0.6	1.5±0.4

excitation part of d-decay. Of course, in the higher excitation energies beyond the '2-body decay' regions, some levels can emit γ-rays and also the excited states of the next daughter nuclei after the sequential decay can also emit γ-rays. Therefore, it may be concluded that the probability of the γ-ray emission from the s-hole state is at least 30 %, which is the sum of the branching ratios listed in Table 4.2. This value will be compared to the succeeding result of the direct γ-decay measurement that carried out simultaneously with the second measurement of the present experiment.

Chapter 5

Summary and conclusions

We presented the first measurements of the *n*-, *p*-, *d*-, *t*-, and α-decays from the *s*-hole states in ^{11}B and ^{15}N excited by the $^{12}\mathrm{C}(p,2p)^{11}\mathrm{B}^*$ and $^{16}\mathrm{O}(p,2p)^{15}\mathrm{N}^*$ reactions at $E_p = 392$ MeV. (The measurements of *n*-decay were only performed for the ^{16}O target.) The quasifree $(p, 2p)$ reactions were measured with the dual spectrometer system consisting of the high resolution spectrometer Grand Raiden (GR) and the large acceptance spectrometer (LAS) at RCNP. The SSD-Ball system composed of sixteen telescopes of $\varDelta E$-E SSD detectors were used for the charged particle decay measurements and thirty liquid scintillation counters were employed to detect decay neutrons. For the ^{16}O target, we used thin $\mathrm{SiO_2}$ and Si targets in the measurements of charged particle decay, where the results were obtained after subtraction processes, and an $\mathrm{H_2O}$ ice target was employed in the neutron decay measurements.

The most of the low lying states excited by the present $(p, 2p)$ reactions were found to be regarded as one-hole states produced by the direct knockout of a proton in the parent nuclei. The contribution of non-quasifree background processes around the 1*s*-hole state in ^{15}N was estimated from the DWIA analysis for the recoil momentum dependence of cross sections and the value of 15 % was derived. (For the ^{11}B(*s*-hole) state, the value of 10 % determined previously by Noro *et al.* [59] was used.) The spectroscopic strengths for the *s*-hole states extracted from the DWIA calculations exhausted to large extent the values of the independent particle shell model in both nuclei.

The measured excitation energy spectrum of ^{11}B shows that the *s*-hole state split into three sub-structures. This splitting agrees qualitatively with the result of recent shell-model calculations [96]. For the *s*-hole state in ^{11}B, the triton decay probability was found to be larger compared to any other decay, although the *Q*-value of the α-decay channel is larger. This provides useful information on the studies of the $S{=}{-2}$ hypernuclear production via the Ξ^- captures into ^{12}C at rest, because the *Q*-value of the elementary process ($\Xi^- p \rightarrow \Lambda\Lambda + 28$ MeV) is almost the same as the separation energy of an s-state proton and only the triton-based fragments were observed until now. The present results for the decay branching ratios of the ^{11}B(s-hole) state can not be reproduced by statistical model calculations. Microscopic cluster model calculations with SU(3)($\lambda\mu$) wave functions [33] explains the experimental decay character qualitatively, while the SU(3)($\lambda\mu$)=[443](04) feature in the microscopic cluster model calculations becomes unclear in the shell-model calculations. A quantitative comparison between the experimental results and theoretical calculations is not sufficient to deduce the ratio of the escape width $\Gamma^{\uparrow}$ to the spreading width $\Gamma^{\downarrow}$ of the s-hole state in ^{11}B. Further calculations including the direct 3-body decay like $2\alpha+t$ will be needed to explain the experimental results for the ^{11}B(s-hole) state.

In the case of the s-hole state in ^{15}N, the measured excitation energy spectrum also shows some sub-structures. By means of a peak-fitting procedure, at least four peaks were found above the excitation energy of 16 MeV and the peak with the central energy of 27 MeV was dominant. This gross structure is well reproduced by the results of the shell-model calculations [96], if the calculated excitation energy would be shifted downward by about 5 MeV. In the binary decay process, the suppression of α-decay is clearly recognized, which supports the selection rule due to the spatial SU(3) symmetry. The shell-model calculations explain the experimental '2-body decay' patterns better than the microscopic cluster model calculations. From a comparison between the experimental results and both the statistical model and shell-model calculations, the ratio of the escape width $\Gamma^{\uparrow}$ to the spreading width $\Gamma^{\downarrow}$ of the s-hole state in ^{15}N was deduced. The obtained ratio, which is dependent on the unknown decay character of the non-quasifree backgrounds, is 0.7 to 1.0. Thus, nearly a half of the total fragmentation of the ^{15}N(s-hole) state is concluded to be the direct decay of the doorway s-hole state.

Decay probabilities of the deexcitation γ-rays from the s-hole state in ^{15}N was estimated from the particle yields decaying to the excited states in residual nuclei. The obtained branching ratio of the γ-ray emission from the s-hole state is at least 30 %, which will be compared to the succeeding results of the analysis of the γ-decay measurements using NaI(Tl) detector arrays. The present data for decay properties of the s-hole states produced from the targets of ^{12}C and ^{16}O provide useful information on the studies of neutrinos and proton decay with use of the organic scintillation detectors and the water Čerenkov detectors.

Acknowledgments

I would like to thank Hidenori Toyokawa, who was first planning the experimental study on the present subject and willingly allowed me to use this work for my doctor thesis. He is one of my best friends since I got acquainted with him at Tokyo Institute of Technology (T.I.T) and we have often enjoyed not only physics research but also drinking, recreation, and other things together.

I am grateful to Taiichi Yamada for his theoretical calculations and valuable discussions. His theoretical works have provided impetus to us to promote this experiment.

I appreciate the continuous advice of Mamoru Fujiwara. I collaborated on many works with him during the last decade and was much influenced by him.

I would like to express my gratitude to Harutaka Sakaguchi, Masanobu Nakamura, and Tetsuo Noro. I have learned a lot of things about physics and experimental techniques from them since I was a graduate student.

Hiroyasu Ejiri aroused the interest of us from a particle physics point of view for the present subject. I am grateful to him.

I have had the good fortune of working closely with talented yang colleagues, particularly Atsushi Tamii, Takahiro Kawabata, Takatsugu Ishikawa, and Naohiko Tsukahara. They were also responsible for a great deal of the work on the experiment.

I would like to thank all other members of the RCNP-E110/E148 experiments; Hidetoshi Akimune, Izuru Daito, Hisako Fujimura, Masatoshi Itoh, Emi Obayashi, Hiroyuki Takeda, Tomoko Taki, Makoto Uchida, and Hidetomo P. Yoshida, and, later joining us, Keigo Hara, Kaoru Yamasaki-Hara, Yasuhiro Sakemi, Yusuke Yasuda, Remco G.T. Zegers, Kazuyoshi Kobayashi, Yoshitaka Itow, and Masato Shiozawa. The success of the experiments is due to the contributions and collaborations of all members.

I am grateful to the scientific and technical staff at RCNP, especially Kichiji Hatanaka, Shiro Ninomiya, and Tomotsugu Wakasa for their efforts to prepare stable clean beams and to provide good control system for the experimental equipments.

I thank Takahide Baba, Toru Inomata, Katsuhiko Ishibashi, Toru Kinashi, Hideki Kohri, Masayoshi Tanaka, and the late Masanori Kawabata for helpful cooperation in the early stage of the experiment (RCNP-E81). Tanaka is a next-door neighbor at RCNP and I enjoyed plenty of chat with him.

I wish to thank G.P.A. Berg for his critical reading of the letter paper, and Kiyomi Ikeda for his encouraging comments in a workshop.

Many figures in the present work for the experimental equipments are based on those illustrated by H. Akimune, T. Inomata, A. Tamii, T. Kawabata, N. Tsukahara, and K. Hara. I thank them again for their beautiful illustrations.

I am very much indebted to Shinsaku Kobayashi, who was my supervisor when I was one of his graduate students, and Hidetsugu Ikegami and Hajime Ohnuma, who were my bosses in my early career at RCNP and at T.I.T., respectively. They generously allowed me to do my work as I wanted.

I thank Ken'ichi Imai, who is the leader of the experimental nuclear hadron physics (NH) group at Kyoto University, for his encouragement and occasional reproof. I am grateful to all members of NH group for a lot of helps and discussions, in particular to Tetsuya Murakami, Haruhiko Funahashi, and Naohito Saito, who were doing many miscellaneous duties sometimes in place of me.

I spent much time at RCNP and some time at SPring-8. I thank all my colleagues and friends at RCNP and at Spring-8/LEPS.

This research was supported in part by the Grant-in-Aid for Scientific Research No. 09440105 from the Japan Ministry of Education, Sports, Culture, Science, and Technology.

Finally I thank my wife Miho and my children Shuu and Kaname for their patience and encouragement during all these years, and my mother and father for their lifelong support.

Appendix A

Efficiency calibration for neutron detectors

In § 3.4.1, the efficiency of neutron detectors is calculated using a Monte-Carlo code Scinful [81], where the NE213 liquid scintillator is substituted for the BC-501A. For the efficiency calibration, two of the neutron detectors were checked by means of the low energy $d+d \longrightarrow {}^{3}\mathrm{He}+n$ reactions.

The experiment was performed at the Kyoto University tandem accelerator laboratory [116]. In the $d+d \longrightarrow {}^{3}\mathrm{He}+n$ reaction, if the neutron detector is placed at the position of the kinematical coincidence with the ^{3}He detector, the neutrons entering the detector in coincidence with ^{3}He particles are tagged by detecting ^{3}He. Thus, the ratio of measured coincidence events to the tagged ^{3}He events is regarded as the efficiency of the neutron detector. 7.1 MeV and 12.6 MeV deuteron beams were used and a CD_2 target with a thickness of 2 mg/cm^2 was employed. A ΔE-E-E_{veto} SSD telescope was used to measure ^{3}He particles with particle identification. Thicknesses of SSD's were 20 μm, 100 μm, and 2mm, respectively. Neutrons emerging from the target went out of the scattering chamber through aluminum windows with a thickness of 1 mm and entered the neutron detector. The neutron absorptions by the aluminum windows were negligible. The kinematical conditions of the measured points are listed in Table A.1 and a schematic view of the experimental setup is shown in Fig. A.1.

A sample spectrum for the particle identification of ^{3}He is shown in Fig A.2. ^{3}He events were unambiguously determined in all the measured angles. In Fig. A.3, energy spectra of two BC-501A liquid scintillators are shown for γ-rays from a ^{137}Cs source. The difference of the energy resolution between two neutron detectors were rather large. The relation of the ADC channels with the electron equivalent energies were obtained with use of the Compton edges of γ-rays of ^{22}Na, ^{137}Cs, ^{40}K, and ^{208}Tl. All Compton edge channels were determined in the same manner as described in § 3.4.1.

Table A.1: Measured kinematical conditions for the $d+d \longrightarrow {}^3$He+n reactions. (τ denotes ^{3}He.)

E_n (MeV)	θ_n (deg)	E_τ (MeV)	θ_τ (deg)	$E_d^\dagger$
2.3	-130	7.9	13.9	7.0
2.9	-130	13.0	12.0	12.5
4.2	-90	6.1	28.7	7.0
5.5	-90	10.2	25.2	12.5
10.9	-50	4.9	41.3	12.5

† The values are mean deuteron energies taking into account the energy losses in the target.

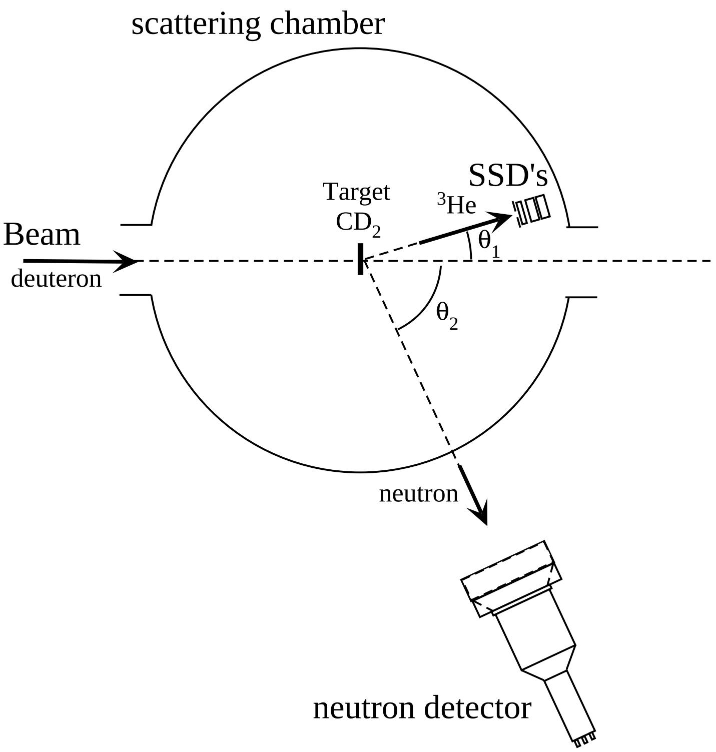

Figure A.1: Schematic view of the setup of the experiment for the efficiency calibration at the Kyoto University tandem accelerator laboratory.

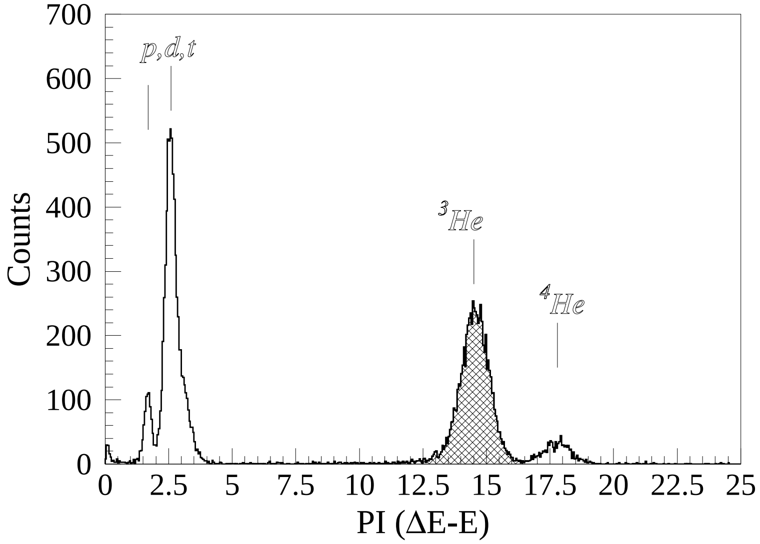

Figure A.2: Particle identification (PI) with a *ΔE*-*E* SSD telescope.

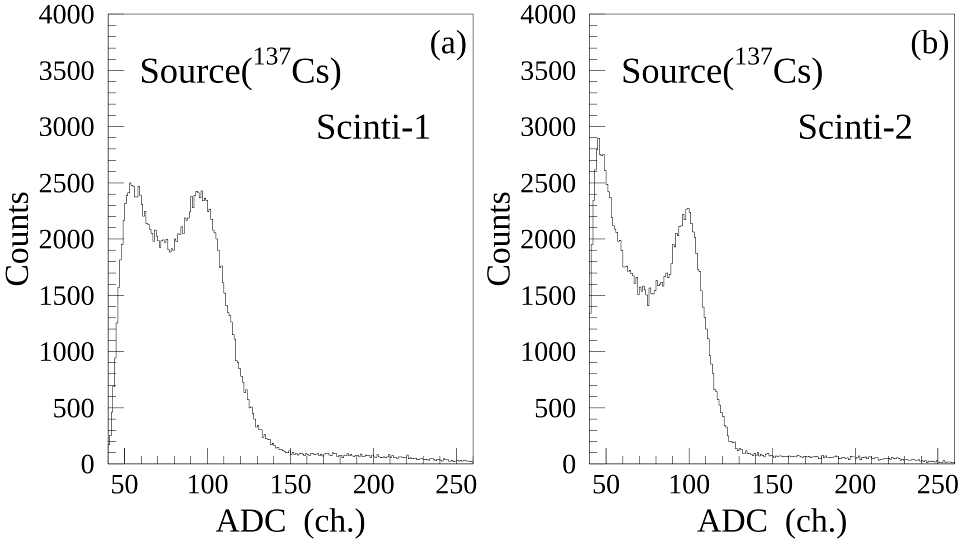

Figure A.3: ADC spectra of γ-rays from a ^{137}Cs source for two liquid-scintillators, ((a) scintillator-1 and (b) scintillator-2). The energy resolutions of two neutron detectors are rather different.

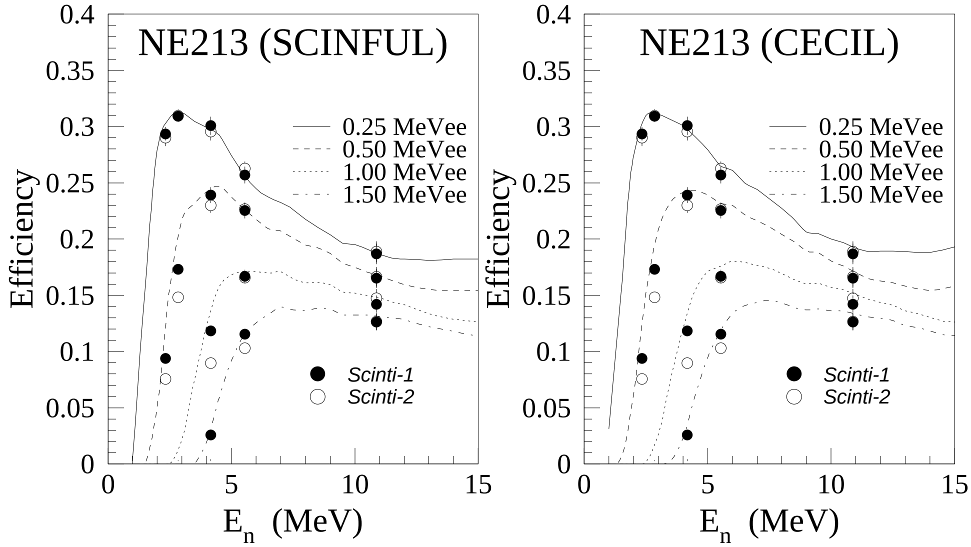

Figure A.4: Comparison of the measured neutron efficiencies with Monte-Carlo calculations using the code (a) Scinful and (b) Cecil for the threshold energies of 0.25, 0.50, 1.0, 1.5 MeVee.

Almost the same relation as Fig. 3.17(d) was obtained.

Measured neutron events were counted with several cuts for the detection threshold energies and efficiencies of both neutron detectors were calculated for each detection threshold energies. The results are plotted in Fig. A.4. The efficiencies of two detectors are slightly different in the slopes of low-energy sides, while, for the higher energies above the maximum efficiency point, the results of both detectors agree well with each other. Calculated efficiency curves with the code Scinful and with another Monte-Carlo code Cecil [117] are also shown in Fig. A.4 for the same threshold energies as experimental data. (In the Scinful calculations, we used the scaling parameter (C) of 0.82, where C is defined with the light output (L) and electron energies (E_e) as L=C(E_e-E_0)≈ CE_e.) The agreement between the experimental values for the detector with a low energy resolution and the results of the Scinful calculation is very fine. The calculated curves with the code Cecil are slightly large at high energies compared to the experimental data points. The Scinful code is better for estimating the efficiency of neutron detector than the Cecil code. It should be noted, however, that, in the lower energies below the maximum point of efficiency, the measured efficiencies seem to be dependent on the energy resolution of the detector. More careful treatments will be needed for low energy neutrons less than 2 MeV.

Appendix B

Uncertainties in statistical-decay calculations

In § 4.3.2, we calculated the statistical decay of the *s*-hole states by using the code Cascade [103], where the transmission coefficients and level densities are important input parameters. For light nuclei such as ^{11}B and ^{15}N, level densities of residual nuclei necessary for the calculations are less ambiguous because the most levels in the excitation energy up to above 10 MeV are known and they can be explicitly used in the calculations. On the other hand, the transmission coefficients are calculated with global optical potential parameters, where the most parameters usually used are those for the medium-heavy and heavy nuclei as the default options in the code Tlcal [108]. Therefore, we made the calculations using the optical potential parameters as well suited for light nuclei as possible in the present work.

Hence, we compare the results of calculations with two different sets of optical potential parameters. In Table B.1, the references for the optical potential parameters employed in the calculations are shown. Potential-1 is the set of parameters used in § 4.3.2 and Potential-2 is that usually used for the medium-heavy and heavy nuclei. Transmission coefficients are obtained by these two different sets of optical potential parameters and then the statistical decay of the *s*-hole states in ^{11}B and ^{15}N are calculated for both sets. Comparisons of the branching ratios between two calculations are shown in Fig. B.1(a) and (b) for the *s*-hole states in ^{11}B and ^{15}N, respectively. Differences between the results of two calculations are very small and at most 10 % for the branching ratios of all decay particles, although the energy dependence of the transmission coefficients, for example, obtained by Watson potentials is rather different from that obtained by Becchetti-Greenlees potentials. It may be concluded that uncertainties in the Cascade calculations due to the choice of the optical potentials are not so large.

Table B.1: Optical potentials used for the calculations of transmission coefficients.

particle	Potential–1		Potential–2	
n	Wilmore and Hodgson	[109]	Rapaport *et al.*	[118]
p	Watson *et al.*	[110]	Becchetti and Greenlees	[119]
d	Ermer *et al.*	[111]	Daehnick *et al.*	[120]
t	England *et al.*	[112]	Perey and Perey	[121]
α	Michel *et al.*	[113]	Satchler	[122]

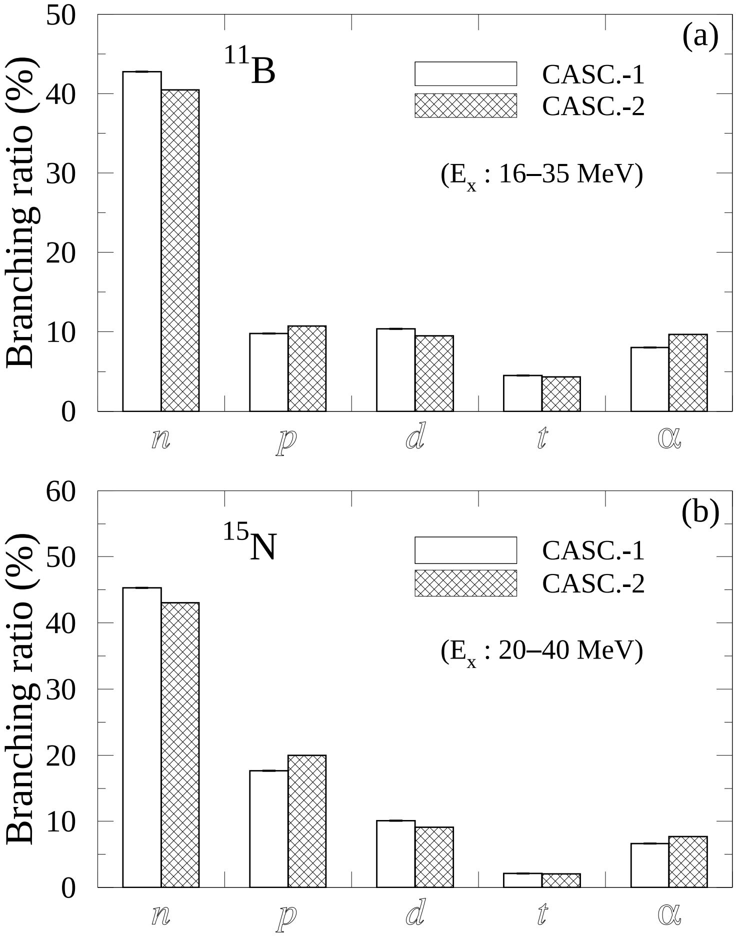

Figure B.1: Comparison of the branching ratios for the s-hole states in (a) ^{11}B and (b) ^{15}N obtained from the CASCADE calculations with two different sets of transmission coefficients (see text).

Appendix C

SU(3) model for s-hole states in light nuclei

Yamada *et al.* calculated spectroscopic factors and partial decay widths for 2-body decay processes from the doorway s-hole states in ^{11}B and ^{15}N by means of the microscopic cluster model with SU(3)$[f](\lambda\mu)$ wave functions [33]. Here, we briefly summarize the calculation method and results of Ref. [33], because the derived selection rule for fragmentations of s-hole states in light nuclei is one of the important subjects in the present work.

The ground-state wave functions of light nuclei are known to be well described by the SU(3)$(\lambda\mu)$ wave functions [123]. Since protons in a 1s-state have zero quanta, the doorway s-hole state produced by the quasifree knockout should have the same spatial symmetry as the ground state of the target nucleus. For example, ^{12}C ground state has dominantly the SU3$(\lambda\mu)$=(04) symmetry with the total quanta N_Q=8 and ^{16}O ground state has dominantly the SU3$(\lambda\mu)$=(00) symmetry with the total quanta N_Q=12. There are two SU(3) states of SU(3)$[f](\lambda\mu)$=[443](04) and [4421](04) for ^{11}B(s-hole) ([4443](00) and [44421](00) for the ^{15}N(s-hole)) with the lowest quanta, which are degenerated in energy.

The partition symmetry $[f]$ has a close connection with the microscopic cluster model [124]. For example, the microscopic α+α+3N and ^{12}C+3N models describe the SU(3)[443]$(\lambda\mu)$ and SU(3)[4443]$(\lambda\mu)$ states of ^{11}B and ^{15}N, respectively, where 3N denotes a three nucleon cluster. The microscopic α+α+2N+N and ^{12}C+2N+N models can describe the SU(3)[4421]$(\lambda\mu)$ and SU(3)[44421]$(\lambda\mu)$ states of ^{11}B and ^{15}N, respectively, as well as the SU(3)[443]$(\lambda\mu)$ and SU(3)[4443]$(\lambda\mu)$ states.

^{11}B(s-hole) state

The wave function of an SU(3)$(\lambda\mu)$=(04) state of ^{11}B(s-hole) is calculated within the framework of the microscopic α+α+2N+N model (see Fig. C.1), where total orbital

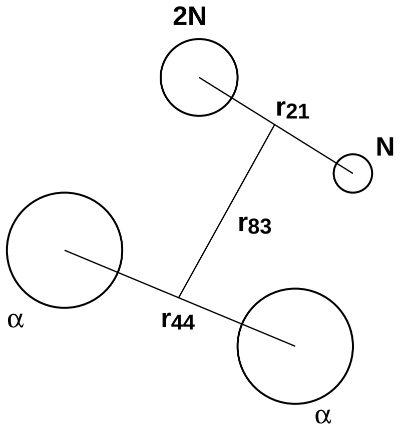

Figure C.1: Coordinate system of the microscopic α+α+$2N$+N cluster model.

angular momentum L^{π}=0^{+}, total spin S=$\frac{1}{2}$, total isospin T=$\frac{1}{2}$, and total quanta N_Q=8. The wave function of an SU(3)$[f](\lambda\mu)$=(04) state of ^{11}B is given by

$$\Phi_L(^{11}\mathrm{B}[f](\lambda\mu)) = \frac{1}{\sqrt{\nu([f](\lambda\mu))}} \sum_c a_c^{[f](\lambda\mu)L} \Phi_L(c), \tag{C.1}$$

$$\Phi_L(c) = \sqrt{\frac{4!4!2!}{11!}} \mathcal{A}' \{\phi_\alpha \phi_\alpha [\phi_{2N}\phi_N]^{ST} \cdot [[u_{n_{44}l_{44}}(\boldsymbol{r}_{44}) u_{n_{21}l_{21}}(\boldsymbol{r}_{21})]_I u_{n_{83}l_{83}}(\boldsymbol{r}_{83})]_L\}, \tag{C.2}$$

$$c = (n_{44}l_{44}, n_{21}l_{21}, I, n_{83}l_{83}), \tag{C.3}$$

with $\boldsymbol{L} = \boldsymbol{I}+\boldsymbol{l}_{83}, \boldsymbol{I} = \boldsymbol{l}_{44}+\boldsymbol{l}_{21}$, and $N_Q = (2n_{44}+l_{44})+(2n_{21}+l_{21})+(2n_{83}+l_{83})$. The internal wave functions, ϕ_α and ϕ_{2N} are given by the lowest shell model wave functions with $(s)^4$ and $(s)^2$ configurations, respectively, and ϕ_N denotes the spin-isospin function of N. The operator $\mathcal{A}'$ antisymmetrizes nucleons belonging to different clusters. The relative wave function referring to the relative coordinate $\boldsymbol{r}_{44}$ between the two α clusters is expanded in terms of the harmonic oscillator wave function $u_{n_{44}l_{44}}$ with the relative orbital angular momentum l_{44} and node number n_{44}. The relative wave functions between $2N$ and N, and between $(\alpha+\alpha)$ and $(2N$+$N)$ are expanded in the same manner. $a_c^{[f](\lambda\mu)L}$ and $\nu([f](\lambda\mu))$ are the expansion coefficient and the eigenvalue, respectively, which are obtained by the diagonalization of the norm kernel matrix.

In order to calculate the spectroscopic factors and partial decay widths of 2-body decay channels, the reduced width amplitudes for the ^{7}Li+α, ^{8}Be+t, and ^{9}Be+d channels are defined as follows:

$$\mathcal{Y}_l^{^7\mathrm{Li}\text{-}\alpha}(r_{74}) = r_{74} \left\langle \sqrt{\frac{11!}{7!4!}} [\Phi_l(^7\mathrm{Li})\phi_\alpha Y_l(\hat{\boldsymbol{r}}_{74})]_{0^+} \middle| \Phi_{0^+}(^{11}\mathrm{B}) \right\rangle_{r_{74}}, \tag{C.4}$$

$$\mathcal{Y}_l^{^8\text{Be-}t}(r_{83}) = r_{83}\left\langle \sqrt{\frac{11!}{8!3!}}[\Phi_l(^8\text{Be})\phi_t Y_l(\hat{\boldsymbol{r}}_{83})]_{0^+}\middle|\Phi_{0^+}(^{11}\text{B})\right\rangle_{r_{83}}, \tag{C.5}$$

$$\mathcal{Y}_l^{^9\text{Be-}d}(r_{92}) = r_{92}\left\langle \sqrt{\frac{11!}{9!2!}}[\Phi_l(^9\text{Be})\phi_d Y_l(\hat{\boldsymbol{r}}_{92})]_{0^+}\middle|\Phi_{0^+}(^{11}\text{B})\right\rangle_{r_{92}}, \tag{C.6}$$

where the internal wave functions, ϕ_d and ϕ_t are given by the lowest shell model wave functions with $(s)^2$ and $(s)^3$ configurations, respectively, For other channels, the reduced width amplitudes are similarly given. The wave functions for ^{10}B, ^{10}Be, ^{9}Be, ^{8}Be, ^{7}Li, ^{6}Li, and ^{5}He are calculated by the microscopic cluster-model technique with use of the SU(3)$(\lambda\mu)$ =(22),(22),(31),(40),(30),(20), and (10) respectively. For example, the ^{7}Li(30), ^{8}Be(40), and ^{9}Be(31) wave functions are given, respectively , within the frame of the microscopic α+t, α+α, and α+α+n cluster models,

$$\Phi_l(^7\text{Li}) = \frac{1}{\sqrt{\nu(30)}}\sqrt{\frac{4!3!}{7!}}\mathcal{A}'\{\phi_\alpha\phi_t u_{nl}(\boldsymbol{r}_{43})\}_{2n+l=3}, \tag{C.7}$$

$$\Phi_l(^8\text{Be}) = \frac{1}{\sqrt{\nu(40)}}\sqrt{\frac{4!4!}{8!}}\mathcal{A}'\{\phi_\alpha\phi_\alpha u_{nl}(\boldsymbol{r}_{44})\}_{2n+l=4}, \tag{C.8}$$

$$\Phi_l(^9\text{Be}) = \frac{1}{\sqrt{\nu(31)}}\sum_{n_{44}l_{44},n_{81}l_{81}} a^l_{n_{44}l_{44},n_{81}l_{81}}\Phi_l(n_{44}l_{44},n_{81}l_{81}),$$

$$\Phi_l(n_{44}l_{44},n_{81}l_{81}) = \sqrt{\frac{4!4!}{9!}}\mathcal{A}'\{\phi_\alpha\phi_\alpha\phi_n[u_{n_{44}l_{44}}(\boldsymbol{r}_{44})u_{n_{81}l_{81}}(\boldsymbol{r}_{81})]_l\}, \tag{C.9}$$

where $\boldsymbol{l} = \boldsymbol{l}_{44} + \boldsymbol{l}_{81}$ and $(2n_{44} + l_{44})$+$(2n_{81} + l_{81})$=5. Then the spectroscopic factors, for example, for the ^{7}Li+α, ^{8}Be+t, and ^{9}Be+d channels are calculated as

$$S^2[^7\text{Li}(l) + \alpha] = \int_0^\infty dr_{74}[\mathcal{Y}_l^{^7\text{Li-}\alpha}(r_{74})]^2 \tag{C.10}$$

$$S^2[^8\text{Be}(l) + t] = \int_0^\infty dr_{83}[\mathcal{Y}_l^{^8\text{Be-}t}(r_{83})]^2 \tag{C.11}$$

$$S^2[^9\text{Be}(l) + d] = \int_0^\infty dr_{92}[\mathcal{Y}_l^{^9\text{Be-}d}(r_{92})]^2 \tag{C.12}$$

The partial decay widths of the doorway ^{11}B(s-hole) state for the ^{10}B+n, ^{10}Be+p, ^{9}Be+d, ^{8}+t, ^{7}Li+α, and ^{6}Li+^{5}He channels are calculated by the separation energy method, Eq. (4.4), that is also used in the sell-model calculations. The reduced amplitude $\mathcal{Y}_l$ is related with the θ_l in Eq. (4.4) as $\theta_l^2(a) = \frac{a^3}{3}\mathcal{Y}_l^2(a)$, where a denotes the channel radius. The total sum of the partial decay widths corresponds to the escape width ($\Gamma^\uparrow$).

^{15}N(s-hole) state

The wave function of an SU(3)$(\lambda\mu)$=(00) state of ^{15}N(s-hole) is calculated within the framework of the microscopic ^{12}C+2N+N model, where total orbital angular momentum L^π=0$^+$, total spin S=$\frac{1}{2}$, total isospin T=$\frac{1}{2}$, and total quanta N_Q=12. The wave function of an SU(3)$[f](\lambda\mu)$=(04) state of ^{15}N is given by

$$\Phi_L(^{15}\mathrm{N}[f](\lambda\mu)) = \frac{1}{\sqrt{\nu([f](\lambda\mu))}}\sum_c a_c^{[f](\lambda\mu)L}\Phi_L(c) \tag{C.13}$$

$$\Phi_L(c) = \sqrt{\frac{12!2!}{15!}}\mathcal{A}'\{[\phi_{2N}\phi_N]^{ST}\cdot[\phi_l(^{12}\mathrm{C})[u_{n_rl_r}(\boldsymbol{r})u_{n_\rho l_\rho}(\boldsymbol{\rho})]_I]_L\}, \tag{C.14}$$

$$c = (l, n_rl_r, n_\rho l_\rho, I), \tag{C.15}$$

with $\boldsymbol{L} = \boldsymbol{l} + \boldsymbol{I}$, $\boldsymbol{I} = \boldsymbol{l}_r + \boldsymbol{l}_\rho$, $N_Q = (2n_r + l_r) + (2n_\rho + l_\rho) + 8$. The internal wave function $\phi_l(^{12}\mathrm{C})$ is given by the SU(3)$[f](\lambda\mu)$=[444](04) wave function. The relative wave functions referring to the relative coordinate $\boldsymbol{r}$ between ^{12}C and (2N+N) and $\boldsymbol{\rho}$ between 2N and N are expanded in terms of the harmonic oscillator wave function $u_{n_rl_r}$ and $u_{n_\rho l_\rho}$, respectively. (l_r and l_ρ are the relative orbital angular momenta and n_r and n_ρ are node numbers.)

The spectroscopic factors and partial decay widths for the 2-body fragmentations of the ^{15}N(s-hole) state, *i.e.*, ^{14}N+n, ^{14}C+p, ^{13}C+d, ^{12}C+t, ^{11}B+α, ^{10}B+^{5}He, $\cdots$, are evaluated in the same manner as in the case of ^{11}B(s-hole) state.

Results

In the calculations of Ref. [33], the excitation energies of the ^{11}B(s-hole) and ^{15}N(s-hole) states are fixed to E_x=20 MeV and 30 MeV, respectively. The calculated spectroscopic factors and partial decay widths for the ^{11}B(s-hole) state are shown in Table C.1 with Q-values of decay to the ground state of each residual nucleus. In Ref. [33], the values are obtained individually for six states of ^{10}B, three states of ^{10}Be, two states of ^{9}Be, three states of ^{8}Be, two states of ^{7}Li, and two states of ^{6}Li, respectively. In Table C.1, only the total sums for the ground state channel and excited channels in each 2-body fragmentation are listed. As seen, the spectroscopic factors for the fragmentations of the two $(\lambda\mu)L^\pi$=(04)0$^+$ eigenstates into the ^{7}Li+α and ^{6}Li+^{5}He channels are exactly zero. This is striking because the Q-value for the α-decay channel is the largest among other channels. Thus, the authors called this a selection rule for fragmentations of doorway s-hole states in light nuclei. It is noted that the spectroscopic factor of the SU(3)$[f](\lambda\mu)$=[4421](04) state for t-decay channel is exactly zero. Since the [4421] spatial symmetry state has more freedom for

Table C.1: Calculated spectroscopic factors (S^2) and partial decay widths ($\mathit{\Gamma}$) of ^{11}B($\lambda\mu$)L^π=(04)0^+ states. Decay Q-values are also shown.

		[443](04)		[4421](04)	
	Q (MeV)	S^2	$\mathit{\Gamma}$ (MeV)	S^2	$\mathit{\Gamma}$ (MeV)
^{10}B+n	8.2	0.147	0.40	0.807	2.20
^{10}Be+p	8.5	0.071	0.19	0.403	1.08
^{9}Be+d	3.9	0.332	0.58	0.456	0.80
^{8}Be+t	8.5	0.481	1.57	0.000	0.00
^{7}Li+α	11.0	0.000	0.00	0.000	0.00
^{6}Li+^{5}He	3.0	0.000	0.00	0.000	0.00
total sum			2.75		4.08

Table C.2: Calculated spectroscopic factors (S^2) and partial decay widths ($\mathit{\Gamma}$) of ^{15}N($\lambda\mu$)L^π=(00)0^+ states. Decay Q-values are also shown.

		[4443](00)		[44421](00)	
	Q (MeV)	S^2	$\mathit{\Gamma}$ (MeV)	S^2	$\mathit{\Gamma}$ (MeV)
^{14}N+n	19.2	0.153	1.29	0.765	6.43
^{14}C+p	19.8	0.077	0.62	0.383	1.50
^{13}C+d	13.8	0.384	1.62	0.480	2.04
^{12}C+t	15.2	0.543	1.29	0.000	0.00
^{11}B+α	19.1	0.000	0.00	0.000	0.00
^{10}B+^{5}He	4.4	0.000	0.00	0.000	0.00
^{9}Be+^{6}Li	2.4	0.000	0.00	0.000	0.00
^{8}Be+^{7}Li	7.6	0.000	0.00	0.000	0.00
total sum			4.83		9.96

the nucleon part outside the α+α core compared to the [443] state, the spectroscopic factors for the ^{10}B+n and ^{10}Be+p channels in the case of [4421](04) are larger than those in the case of [443] but the spectroscopic factor for the ^{8}B+t channel is much small in the [4421](04) state.

The calculated spectroscopic factors and partial decay widths for the ^{15}N(s-hole) state are shown in Table C.2 with Q-values of decay to the ground state of each residual nucleus. In Ref. [33], the values are obtained individually for four states of ^{14}N, two states of ^{14}C, two states of ^{13}C, three states of ^{12}C, two states of ^{11}B, three states of ^{10}B, a state of ^{9}Be, and three states of ^{8}Be, respectively. In Table C.2, only the total sums for the ground state channel and excited channels in each 2-body fragmentation are listed. As seen similarly to the case of the ^{11}B(s-hole) state, the spectroscopic factors for the fragmentation of the $(\lambda\mu)L^{\pi}$=(00)0^{+} eigenstates into the ^{11}B+α, ^{10}B+^{5}He, ^{9}Be+^{6}Li, and ^{8}Be+^{7}Li channels are exactly zero. The spectroscopic factor of the SU(3)$[f](\lambda\mu)$=[44421](00) state for t-decay channel is also exactly zero like the [4421](04) state in the ^{11}B(s-hole). It is worth while to mention that in the case of the ^{15}N the calculated spectroscopic factors decaying to the excited channels of each 2-body fragmentation are larger than those decaying to the ground state channel, which qualitatively agrees with the results of the present measurements.

Bibliography

[1] O. Chamberlain and E. Segrè, Phys. Rev. **87**, 81 (1952).

[2] J.B. Cladis, W.N. Hess, and B.J. Moyer, Phys. Rev. **87**, 425 (1952).

[3] J.M. Wilcox and B.J. Moyer, Phys. Rev. **99**, 875 (1955)

[4] M. Riou, Rev. Mod. Phys. **37**, 375 (1965).

[5] T. Berggren and H. Tyren, Annu. Rev. Nucl. Sci. **16**, 153 (1966).

[6] G. Jacob and Th.A.J. Maris, Rev. Mod. Phys. **38**, 121 (1966).

[7] H. Tyrén, S. Kullander, O. Sundberg, R. Ramachandran, and P. Isacsson, Nucl. Phys. **79**, 321 (1966).

[8] A.N. James, P.T. Andrews, P. Kirkby, and B.G. Lowe, Nucl. Phys. **138**, 145 (1969).

[9] G. Landaud, J. Yonnet, S. Kullander, F. Lemeilleuur, P.U. Renberg, B. Fagerström, A. Yohansson, and G. Tibell, Nucl. Phys. **173**, 337 (1971).

[10] G. Jacob and Th.A.J. Maris, Rev. Mod. Phys. **45**, 6 (1973), and references therein.

[11] H.A. Bethe, Annu. Rev. Nucl. Sci. **21**, 93 (1971).

[12] U. Amaldi, Jr, G.C. Venuti, G. Cortellesssa, C. Fronterotta, A. Reale, P. Salvadori, and P. Hillman, Phys. Rev. Lett. **13**, 341 (1964).

[13] S. Fullani and J. Mougey, in *Advances in Nuclear Physics*, edited by J.W. Negele and E. Vogt (Plenum Press, New York, 1984), Vol. 14, p. 1, and references therein.

[14] S.L. Belostotskii, S.S. Volkov, A.A. Vorob'ev, Yu.V. Dotsenko, L.G. Kudin, N.P. Kuropatkin, O.V. Miklukho, V.N. Nikulin, and O.E. Prokof'ev, Sov. J. Nucl. Phys. **41**, 903 (1985).

[15] S.S. Volkov, A.A. Vorob'ev, O.A. Domchenkov, Yu.V. Dotsenko, N.P. Kuropatkin, A.A. Lobodenko, O.V. Miklukho, V.N. Nikulin, V.E. Starodubskii, A.Yu. Tsaregorodtsev, Zh.A. Chakhalyan, and Yu.A. Shcheglov, Sov. J. Nucl. Phys. **52**, 848 (1990).

[16] P. Kitching, W.J. McDonald, Th.A.J. Maris, and C.A.Z. Vasconcellos, in *Advances in Nuclear Physics*, edited by J.W. Negele and E. Vogt (Plenum Press, New York, 1985), Vol. 15, p. 43.

[17] K. Hatanaka, M. Kawabata, N. Matsuoka, Y. Mizuno, S. Morinobu, M. Nakamura, T. Noro, A. Okihana, K. Sagara, K. Takahisa, H. Takeda, K. Tamura, M. Tanaka, S. Toyama, H. Yamazaki, and Y. Yuasa, Phys. Rev. Lett. **78**, 1014 (1997).

[18] C.A. Miller, K.H. Hicks, R. Abegg, M. Ahmad, N.S. Chant, D. Frekers, P.W. Green, L.G. Greeniaus, D.H. Hutcheon, P. Kitching, D.J. Mack, W.J. McDonald, W.C. Olsen, R. Schubank, P.G. Roos, and Y. Ye, Phys. Rev. C **57**, 1756 (1998).

[19] R. Neveling, A.A. Cowley, G.F. Steyn, S.V. Förtsch, G.C. Hillhouse, J. Mano, and S.M. Wyngaardt, Phys. Rev. C **66**, 034602 (2002).

[20] G. van der Steenhoven, H.P. Blok, E. Jans, M. de Jong, L. Lapikás, E.N.M. Quint, and P.K.A. de Witt Huberts, Nucl. Phys. **A480**, 547 (1988).

[21] M. Leuschner, J.R. Calarco, F.W. Hersman, E. jans, G.J. Kramer, L. Lapikás, G. van der Steenhoven, P.K.A. de Witt Huberts, H.P. Blok, N. Kalantar-Nayestanaki, and J. Friedrich, Phys. Rev. C **49**, 955 (1994).

[22] S.C. Pieper, R.B. Wiringa, and V.R. Pandharipande, Phys. Rev. C **46**, 1741 (1992).

[23] J.H. Heisenberg and B. Mihaila, Phys. Rev. C **59**, 1440 (1999).

[24] C. Barbieri and W.H. Dickhoff, Phys. Rev. C **65**, 064313 (2002).

[25] H. Feshbach, *Theoretical Nuclear Physics: Nuclear Reactions*, (John Willy & Sons, New York, 1992), Chap. V.

[26] J.P. Jeukenne, A. Lejeune, and C. Mahaux, Phys. Rep. C **25**, 83 (1976).

[27] H.S. Köhler, Nucl. Phys. **88**, 529 (1966).

[28] W. Hornyak, *Nuclear Structure* (Academic, New York, 1975), Chap. IV.

[29] H. de Vries, C.W. de Jager, and C. de Vries, Atomic Data and Nuclear Data Tables. **36**, 495 (1987).

[30] W. Fritsch, R. Lipperheide, and U. Wille, Nucl. Phys. **A241**, 79 (1975).

[31] H. Orland and R. Schaeffer, Nucl. Phys. **A299**, 442 (1978).

[32] R. Sartor and C. Mahaux, Phys. Rev. C **21**, 2613 (1980).

[33] T. Yamada, M. Takahashi and K. Ikeda, Phys. Rev. C **53**, 752(1996).

[34] H. Bando, T. Yamada, and J. Zofka, Phys. Rev. C **36**, 1640 (1996).

[35] T. Yamada and K. Ikeda, Prog. Theor. Phys. Suppl. No. **117**, 445 (1994).

[36] R. Bertini *et al.*, Nucl. Phys. **A368**, 365, (1981).

[37] S. Aoki *et al.*, Prog. Theor. Phys. **85**, 1287 (1991).

[38] S. Aoki *et al.*, Prog. Theor. Phys. **89**, 493 (1993).

[39] S. Aoki *et al.*, Phys. Lett. B **355**, 45 (1995).

[40] A. Ichikawa *et al.*, Phys. Lett. B **500**, 37 (2001);
A. Ichikawa, PhD thesis, Kyoto University, 2001 (unpublished).

[41] H. Takahashi *et al.*, Phys. Rev. Lett. **87**, 212502 (2001).

[42] D. Zhu, C.B. Dover, A. Gal, and M. May, Phys. Rev. Lett. **67**, 2268 (1991).

[43] M. Sano, M. Wakai, and Y. Yamamoto, Prog. Theor. Phys. **87**, 957 (1992);
Y. Yamamoto, M. Sano, and M. Wakai, Prog. Theor. Phys. Suppl. No. **117**, 265 (1994).

[44] Y. Hirata, Y. Nara, A. Ohnishi, T. Harada, and J. Randrup, Prog. Theor. Phys. **102**, 89 (1999).

[45] T. Yamada and K. Ikeda, Phys. Rev. C **56**, 3216 (1997).

[46] Y. Suzuki *et al.*, Phys. Lett. B **311**, 357 (1993).

[47] Y. Hayato *et al.* (The Super-Kamiokande Collaboration), Phys. Rev. Lett. **83**, 1529 (2000).

[48] K. Kobayashi, PhD thesis, University of Tokyo, 2002 (unpublished).

[49] H. Ejiri, Phys. Rev. C **48**, 1442 (1993).

[50] J. Hisano, J. Maruyama, and T. Yanagida, Nucl. Phys. **B402**, 46 (1993).

[51] F.L .Lang, C.W. Werntz, C.J. Crannell, J.I. Trombka, and C.C. Chang, Phys. Rev. C **35**, 1214 (1987).

[52] H. Toyokawa, H. Akimune, T. Baba, I. Daito, H. Ejiri, M. fujiwara, T. Inomata, M. Kawabata, T. Kinashi, T.Noro, A. Tamii, M. Tanaka, T. Yamada, and M. Yosoi, in *Proceedings of the XIV RCNP OSAKA International Symposium on Nuclear Reaction Dynamics of Nucleon-Hadron Many Body System, RCNP, Osaka University, Osaka, 1995*, edited by H. Ejiri, T. Noro, K. Takahisa, and H. Toki (World Scientific, Singapore, 1996), p. 339;
H. Toyokawa, H. Akimune, T. Baba, I. Daito, H. Ejiri, H. Fujimura, M. Fujiwara, T. Inomata, M. Kawabata, T. Kinashi, H. Kohri, T.Noro, A. Tamii, M. Tanaka, T. Yamada, and M. Yosoi, in *Proceedings of the 8th International Conference on Nuclear Reaction Mechanisms, Varenna, Italy, 1997*, (Universita Degli Studi Di Milano, 1997), p. 606.

[53] N. Tsukahara, M.Sc. thesis, Kyoto University, 2000 (unpublished).

[54] M. Fujiwara, H. Akimune, I. Daito, H. Fujimura, Y. Fujita, K. Hatanaka, H. Ikegami, I. Katayama, K. Nagayama, N. Matsuoka, S. Morinobu, T. Noro, M. Yoshimura, H. Sakaguchi, Y. Sakemi, A. Tamii, and M. Yosoi, Nucl. Instrum. Methods Phys. Res. A **422**, 484 (1999).

[55] N. Matsuoka, T. Noro, K. Sagara, S. Morinobu, A. Okihana, and K. Hatanaka, RCNP annual report, 1991, p. 186; 1990, p. 235.

[56] K. Hatanaka, K. Takahisa, H. Tamura, M. Sato, and I. Miura, Nucl. Instrum. Methods Phys. Res. A **384**, 575 (1997).

[57] I. Miura, T. Yamazaki, A. Shimizu, K. Hosono, T. Itahashi, T. Saito, A. Ando, K. Tamura, K. Hatanaka, M. Kibayashi, M. Uraki, H .Ogata, M. Kondo, and H. Ikegami, in *Proceedings of the 13th International Conference on Cyclotrons and their Applications, Vancouver, 1992*, edited by G. Dutte and M. K. Craddock (World Scientific, Singapore, 1993), p. 3

[58] T. Wakasa, K. Hatanaka, Y. Fujita, G. P. A. Berg, H. Fujimura, H. Fujita, M. Itoh, J. Kamiya, T. Kawabata, K. Nagayama, T. Noro, H. Sakaguchi, Y. Shimbara, H. Takeda, K. Tamura, H. Ueno, M. Uchida, M. Uraki, Y. Yasuda, and M. Yosoi, Nucl. Instrum. Methods Phys. Res. A **482**, 79 (2002).

[59] T. Noro, T. Baba, K. Hatanaka, M. Ito, M. Kawabata, N. Matsuoka, Y. Mizuno, S. Morinobu, M. Nakamura, A. Okihana, K. Sagara, H. Sakaguchi, K. Takahisa, H. Takeda, A. Tamii, K. Tamura, M. Tanaka, S. Toyama, H. Yamazaki, Y. Yuasa, H. Yoshida, and M. Yosoi, Nucl. Phys. **A629**, 324c (1998).

[60] D. Koltun, Phys. Rev. Lett. **28**, 182 (1972).

[61] M. Fujiwara, A. Nakanishi, Y. Fujita, N. Matsuoka, T. Noro, S. Morinobu, and H. Ikegami, RCNP annual report, 1989, p. 201.

[62] T. Noro, M. Fujiwara, O. Kamigaito, S. Hirata, Y. Fujita, A. Yamagoshi, T. Takahashi, H. Akimune, Y. Sakemi, M. Yosoi, H. Sakaguchi, and J. Tanaka, RCNP annual report, 1991, p. 177.

[63] H.P. Yoshida, T. Baba, T. Noro, M. Kawabata, H. Akimune, H. Sakaguchi, A. Tamii, H. Takeda, and T. Kawabata, RCNP annual report, 1996, p. 164.

[64] H. Akimune, I. Daito, Y. Fujita, M. Fujiwara, M. B. Greenfield, M. N. Harakeh, T. Inomata, J. Jänecke, K. Katori, S. Nakayama, H. Sakai, Y. Sakemi, M. Tanaka, and M. Yosoi, Phys. Lett. B **323**, 107 (1994); Phys. Rev. C **52**, 604 (1995).

[65] T. Inomata, H. Akimune, I. Daito, H. Ejiri, H. Fujimura, Y. Fujita, M. Fujiwara, M. N. Harakeh, K. Ishibashi, H. Kohri, N. Matsuoka, S. Nakayama, A. Tamii, M. Tanaka, H. Toyokawa, M. Yoshimura, and M. Yosoi, Phys. Rev. C **57**, 3153 (1998);
T. Inomata, PhD thesis, Osaka University, 1998 (unpublished).

[66] A. Tamii, H. Sakaguchi, H. Takeda, M. Yosoi, H. Akimune, M. Fujiwara, H. Ogata, M. Tanaka, and H. Togawa, IEEE Trans. Nucl. Sci. **43**, 2488 (1996).

[67] A. Tamii, M. Itoh, T. Kawabata, H. Sakaguchi, H. Takeda, T. Taki, H. Torii, M. Yosoi, H. Akimune, T. Baba, M. Fujiwara, M. Kawabata, T. Noro, and H. Yoshida, in *Proceedings of the 2nd International Data Acquisition Workshop on Networked Data Acquisition System, Osaka, Japan, 1996*, edited by M. Nomachi and S. Ajimura (World Scientific, Singapore 1997), p. 238.

[68] T. Kawabata, H. Sakaguchi, A. Tamii, H. Takeda, T. Taki, and H. Yoshida, RCNP annual report, 1996, p. 161.

[69] H. Laurent, H. Lefort, D. Beaumel, Y. Blumenfeld, S. Fortier, S. Galès, J. Gillot, J.C. Roynette, P. Volkov, and S. Brandenburg, Nucl. Instrum. Methods Phys. Res. A **326**, 517 (1993).

[70] C.A. Goulding, A.A. Robba, and E.R. Shunk, LANL Program Technical note, LA-N2TN-87-201, 1987.

[71] T. Kawabata, H. Akimune, H. Fujimura, H. Fujita, Y. Fujita, M. Fujiwara, K. Hara, K. Hatanaka, K. Hosono, T. Ishikawa, M. Itoh, J. Kamiya, M. Nakamura, T. Noro, E. Obayashi, H. Sakaguchi, Y. Shimbara, H. Takeda, T. Taki, A. Tamii, H. Toyokawa, N. Tsukahara, M. Uchida, H. Ueno, T. Wakasa, K. Yamasaki, Y. Yasuda, H.P. Yoshida, and M. Yosoi, Nucl. Instrum. Methods Phys. Res. A **459**, 171 (2001).

[72] T. Kawabata, T. Ishikawa, M. Itoh, M. Nakamura, H. Sakaguchi, H. Takeda, T. Taki, M. Uchida, Y. Yasuda, M. Yosoi, H. Akimune, K. Yamasaki, G. P. A. Berg, H. Fujimura, K. Hara, K. Hatanaka, J. Kamiya, T. Noro, E. Obayashi, T. Wakasa, H. P. Yoshida, B. A. Brown, H. Fujita, Y. Fujita, Y. Shimbara, H. Ueno, M. Fujiwara, K. Hosono, A. Tamii, and H. Toyokawa, Phys. Rev. C **65**, 064316 (2002);
T. Kawabata, PhD thesis, Kyoto University, 2002 (unpublished).

[73] HBOOK, CERN Program Library entry Y250.

[74] PAW, CERN Program Library entry Q121.

[75] W.R. Leo, *Techniques for Nuclear and Particle Physics Experiments (2nd Edition)*, (Springer-Verlag, Berlin Heidelberg, 1994), p. 168.

[76] J. Mougey, M. Bernheim, A. Bussière, A. Gillebert, Phuan Xuan Ho, M. Priou, D. Royer, I. Sick, and G.J. Wagner, Nucl. Phys. **A262**, 461 (1976).

[77] A. Okihana, N. Matsuoka, T. Noro, H. Akiyoshi, H. Utsunomiya, and M. Yoshimura, RCNP annual report, 1993, p. 171;
A. Okihana, N. Matsuoka, T. Noro, and M. Yoshimura, *ibid.*, 1994, p. 150.

[78] E. Obayashi, M.Sc. thesis, Osaka University, 1999 (unpublished).

[79] G, Dietze and H. Klein, Nucl. Instrum. Methods Phys. **193**, 549 (1982).

[80] N, Olsson, P.-O. Söderman,L. Nilsson, and H. Laurent, Nucl. Instrum. Methods Phys. Res. A **349**, 231 (1994).

[81] J.K. Dickens, program code SCINFUL, ORNL-6462;ORNL-6463 (1988).

[82] J.F. Briesmeister (Editor), program code MCNP-4B, LA-12625-M (1997).

[83] N.S. Chant and P.G. Roos, Phys. Rev. C **27**, 1060 (1983);
program code THREEDEE.

[84] R.A. Arndt, C.H. Oh, I.I. Strakovsky, R.L. Workman, and F. Dohrmann, Phys. Rev. C **56**, 3005 (1997); solution of SAID program (http://gwdac.phys.gwu.edu).

[85] L.R. B. Elton and A. Swift, Nucl. Phys. **A94**, 52 (1967).

[86] E.D. Cooper, S. Hama, B.C. Clark, and R.L. Mercer, Phys. Rev. C **47**, 297 (1993).

[87] F. Ajzenberg-Selove, Nucl. Phys. **A506**, 1 (1990).

[88] G. van der Steenhoven, H.P. Blok, J.W.A. den Herder, E. Jans, P.H.M. Keizer, L. Lapikás, E.N.M. Quint, P.K.A. de Witt Huberts, G.W.R. Dean, P.J. Brussaard, P.W.M. Glaudemans, and D. Zwarts, Phys. Lett. **156B**, 151 (1985).

[89] G. Mairle and G.J. Wagner, Nucl. Phys. **A253**, 253 (1975).

[90] F. Ajzenberg-Selove, Nucl. Phys. **A523**, 1 (1991).

[91] J.C. Hiebert and E. Newman, and R.H. Bassel, Phys. Rev. **154**, 154 (1967).

[92] G. Mairle and G.J. Wagner, Z. Phys. **A258**, 321 (1973).

[93] W.J. McDonald, R.N. McDonald, W.C. Olsen, R. Dymarz, F. Khanna, L. Antonuk, J.M. Cameron, P. Kitching, G.C. Neilson, D.M. Sheppard, D.H. Hutcheon, C.A. Miller, and J. Kallne, Nucl. Phys. **A456**, 577 (1986).

[94] T. Noro *et al.*, RCNP Annual Report, 1996, p. 48.

[95] C.J. Horowitz, D.P. Murdock, and B.D. Sero, in *Computational Nuclear Physics*, edited by K. Langanke, J.A. Marhun, and S.E. Koonin (Springer-Verlag, Berlin Heidelberg, 1991) Vol. 1, p. 129.

[96] T. Yamada, Nucl. Phys. **A687**, 297c (2001), and *private communication.*

[97] M. Benjamintz, W.R. Falk, J.R. Campbell, A. Green, P.G. Roos, P.L. Walden, S. Yen, A.G. Ling, E.G. Auld, E. Korkmaz, and M.A. Punyasena, Phys. Rev. C **58**, 964 (1998).

[98] M. Yosoi, H. Toyokawa, N. Tsukahara, H. Akimune, I. Daito, H. Ejiri, H. Fujimura, M. Fujiwara, T. Ishikawa, M. Itoh, T. Kawabata, M. Nakamura, T. Noro,

E. Obayashi, H. Sakaguchi, H. Takeda, T. Taki, A. Tamii, M. Uchida, T. Yamada and H. P. Yoshida, in *Proceedings of the workshop on Frontiers in Nuclear Physics, Suwon, Feb. 18 -19, 2000*, Edited by H. Bhang, M. Fujiwara and B.T. Kim (Sungkyunkwan University Press, Seoul, 2000), p. 95.

[99] S. Cohen and D. Kurath, Nucl. Phys. **73**, 1 (1965).

[100] D.J. Millener and D. Kurath, Nucl. Phys. **A255**, 315 (1975).

[101] H. Horiuchi, K. Ikeda, and Y. Suzuki, Prog. Theor. Phys. Suppl. No. **52**, 89 (1972).

[102] A. Bohr and B.R. Mottelson, *Nuclear Structure*, Vol. I, (Benjamin, New York, 1969), p. 437.

[103] F. Pühlhofer, Nucl. Phys. **A280**, 267 (1977);
M. N. Harakeh, extended version of program code CASCADE (1983) (unpublished).

[104] W. Hauser and H. Feshbach, Phys. Rev. **87**, 366 (1952).

[105] T.D. Thomas, Nucl. Phys. **53**, 558 (1964).

[106] E. Gadioli and R. Zetta, Phys. Rev. **167**, 1016 (1968).

[107] H. Vonach and M. Hille, Nucl. Phys. **A127**, 289 (1969).

[108] F.Pühlhofer, program code TLCALC (unpublished).

[109] D. Wilmore and P.E. Hodgson, Nucl. Phys. **55**, 673 (1964).

[110] B.A. Watson, P.P Singh, and R.E. Segel, Phys. Rev. **182**, 977 (1969).

[111] M. Ermer, H. Clement, G. Holetzke, W. Kabitzke, G. Graw, R. Hertenberger, H. Kader, F. Merz, and P. Schiemenz, Nucl Phys. **A533**, 71, (1991).

[112] J.B.A. England *et al.*, Nucl. Phys. **A475**, 422 (1987).

[113] F. Michel, J. Albinski, P. Belerly, Th. Delbar, Gh. Grégoire, B. Tasiaux, and G. Reidemeister, Phys. Rev. C **28**, 1904 (1983).

[114] W. Dilg, W. Schantl, H. Vonach, and M. Uhl, Nucl. Phys. **A217**, 269 (1973).

[115] R.B. Firestone and V.S. Shirley (Editors), *Table of Isotopes*, Vol. I (John Wiley & Sons, New York, 1996).

[116] M. Nakamura, S. Shimoura, K. Takimoto, H. Sakaguchi, and S. Kobayashi, Nucl. Instrum. Methods Phys. Res. A **268**, 313 (1988).

[117] R.R. Cecil, B.D. Anderson, and R. Madey, Nucl. Instrum. Methods Phys. **161**, 439 (1979); program code CECIL.

[118] J. Rapaport, V. Kulkarni, and R.W. Finlay, Nucl. Phys. **A330**, 155 (1979).

[119] F.D. Becchetti, Jr. and G.W. Greenlees, Phys. Rev. **182**, 1190 (1969).

[120] W.W. Daehnick, J.D. Childs, and Z. Vrcelj, Phys. Rev. C **21**, 2253 (1980).

[121] C.M. Perey and F.G. Perey, Atomic Data and Nuclear Data Tables. **17**, 1 (1976); The potential of F.D. Becchetti, Jr. and G.W. Greenlees.

[122] G.R. Satchler, Nucl. Phys. **70**, 177 (1965).

[123] J.P. Elliot, Proc. R. Soc. London **245**, 128 (1958); **245**, 562 (1958); J.P. Elliot and M. Harvey, *ibid.* **272**, 557 (1963).

[124] B.F. Bayman and A. Bohr, Nucl. Phys. **9**, 596 (1958/59).

[125] H. Furutani, H. Kanada, T. Kaneko, S. Nagata, H. Nishioka, S. Okabe, S. Saito, T. Sakuda, and M. Seya, Prog. Theor. Phys. Suppl. No. **68**, 193 (1980).

List of Figures

List of Tables